APPROVAL SHEET

Title of Thesis: Analysis of chalcogenide-glass photonic crystal fibers
Name of Candidate: Zhihang (Jonathan) Hu
Doctor of Philosophy, 2008

Dissertation and Abstract Approved: ____________________________
Curtis R. Menyuk
Professor
Computer Science and Electrical Engineering

Date Approved: ______________________________

Curriculum Vitae

Zhihang (Jonathan) Hu
5200 Westland Blvd. 205A
Baltimore, MD 21227
Phone: (410)455-6507, Fax: (410)455-6500
E-mail: `hu1@umbc.edu`

Education:

Ph.D.	**Electrical Engineering: Photonics** **University of Maryland Baltimore County**, September 2008 Dissertation: Analysis of chalcogenide-glass photonic crystal fibers Advisor: Dr. Curtis R. Menyuk
M.Sc.	**Electrical Engineering** **University of Tulsa**, Tulsa, OK August 2001
B.Sc.	**Electrical Engineering** **Zhejiang University**, Hangzhou, China June 1997

Awards and honors:

– Chinese government award for outstanding self-financed students abroad (2006)

– First price award in IEEE Baltimore and Washington-Northern Virginia LEOS chapter graduate student poster competition (2008)

Services:

Session chair for Frontier in Optics/Laser Science Conference (2008)
Referee for *Optics Express*,
Photonics Technology Letters,
Journal of Lightwave Technology,
Journal of Quantum Electronics,
Optics Communications,
Fiber and Integrated Optics, and
Journal of Modern Optics

Archival journal publications:

1. **J. Hu**, C. R. Menyuk, L. B. Shaw, J. S. Sanghera, and I. D. Aggarwal, “Raman response function and supercontinuum generation in an As_2Se_3-based chalcogenide fibers,” Opt. Express (under review).

2. **J. Hu** and C. R. Menyuk, “Understanding leaky modes: Slab waveguide revisited,” Adv. Opt. Photon. **1**, 58–106 (2009), http://www.opticsinfobase.org/aop/abstract.cfm?URI=aop-1-1-58.

3. **J. Hu** and C. R. Menyuk, “Optimization of the operational bandwidth in air-core photonic bandgap fibers for IR transmission,” Opt. Commun. **282**, 18–21 (2009)

4. **J. Hu** and C. R. Menyuk, “Leakage loss and bandgap analysis in air-core photonic bandgap fiber for nonsilica glasses,” Opt. Express **15**, 339–349 (2007), http://www.opticsinfobase.org/abstract.cfm?URI=oe-15-2-339.

5. P. Griggio, **J. Hu**, J. Wen, G. E. Tudury, J. Zweck, B. S. Marks, L. Yan, G. M. Carter, and C. R. Menyuk, “Characterizing pattern dependence in transmitters and receivers for modeling optical communication systems,” Opt. Commun. **272**, 107–110 (2007).

6. **J. Hu**, B. S. Marks, C. R. Menyuk, J. Kim, T. F. Carruthers, B. M. Wright, T. F. Taunay, and E. J. Friebele, “Pulse compression using a tapered microstructure optical fiber,” Opt. Express **14**, 4026–4036 (2006), http://www.opticsinfobase.org/abstract.cfm?URI=oe-14-9-4026.

7. J. Kim, U-C. Paek, B. H. Lee, **J. Hu**, B. Marks, and C. R. Menyuk, “Impact of interstitial air holes on a wide bandwidth rejection filter made from a photonic crystal fiber,” Opt. Lett. **31**, 1196–1198 (2006).

8. G. E. Tudury, **J. Hu**, B. S. Marks, A. S. Lenihan, C. R. Menyuk, and G. M. Carter, “Gain characteristics of a 210-km hybrid Raman/EDFA amplified fiber loop,” Opt. Commun. **261**, 152–157, (2006).

9. **J. Hu**, B. S. Marks, Q. Zhang, and C. R. Menyuk, “Modeling backward-pumped Raman amplifiers,” J. Opt. Soc. Am. B **22**, 2083–2090, (2005).

10. **J. Hu**, B. S. Marks, and C. R. Menyuk, “Flat-gain fiber Raman amplifiers using equally spaced pumps,” J. Lightwave Technol. **22**, 1519–1522, (2004).

Refereed conference proceedings:

1. **J. Hu**, C. R. Menyuk, L. B. Shaw, J. S. Sanghera, and I. D. Aggarwal, "Supercontinuum generation in an As_2Se_3-based chalcogenide PCF using four-wave mixing and soliton self-frequency shift," in Proc. Conference on Optical Fiber Communications (OFC), San Diego, CA, paper OWU6, (2009).

2. W. Torruellas, M. Dennis, J. Warren, **J. Hu**, and C. Menyuk, "Parametric generation in optical fibers in the 900-950nm spectral band," Proceedings of SPIE, Volume 6952 (2008).

3. **J. Hu**, C. R. Menyuk, L. B. Shaw, J. S. Sanghera, and I. D. Aggarwal, "Raman response function and supercontinuum generation in chalcogenide fiber," in Proc. Conference on Lasers and Electro-Optics (CLEO), San Jose, CA, paper CMDD2, (2008).

4. **J. Hu** and C. R. Menyuk, "Optimize operational bandwidth through core design in air-core photonic bandgap fibers for IR transmission," in Proc. Conference on Optical Fiber Communications (OFC), San Diego, CA, paper JWA9, (2008).

5. V. Veerasubramanian, **J. Hu**, J. Zweck, and C. R. Menyuk, "Propagation analysis of an 80-Gb/s wavelength-converted signal utilizing XPM," in Proc. Conference on Optical Fiber Communications (OFC), San Diego, CA, paper JWA69, (2008).

6. J. J. Butler, S. R. Sueoka, S. R. Montgomery, S. R. Flom, R. G.S. Pong, J. S. Shirk, T. E. Taunay, B. M. Wright, **J. Hu**, and C. R. Menyuk, "Optical limiting in solid-core photonic crystal fibers," in Proc. Conference on Lasers and Electro-Optics (CLEO), Baltimore, MD, paper CMS6, (2007).

7. **J. Hu** and C. R. Menyuk, "Use of fingers in the core to reduce leakage loss in air-core photonic bandgap fibers," in Proc. Conference on Optical Fiber Communications (OFC), Anaheim, CA, paper OML6, (2007).

8. **J. Hu** and C. R. Menyuk, "Loss and bandgap analysis in air-core photonic bandgap fiber for nonsilica glasses," in Proc. Conference on Quantum Electronics and Laser Science Conference (QELS), Long Beach, CA, paper JWB55, (2006).

9. **J. Hu** and C. R. Menyuk, "Loss and bandgap analysis in air-core photonic bandgap fiber for IR transmission," in Proc. Conference on Optical Fiber Communications (OFC), Anaheim, CA, paper OFC5, (2006).

10. **J. Hu**, B. S. Marks, J. Kim, and C. R. Menyuk, “Mode compression and loss in tapered microstructure optical fiber,” in Proc. Conference on Quantum Electronics and Laser Science Conference (QELS), Baltimore, MD, paper JWB56, (2005).

11. J. Wen, P. Griggio, **J. Hu**, L. Yan, and G. M. Carter, “Quantitative study of the performance statistics of WDM systems under different channel spacings,” in Proc. Conference on Lasers and Electro-Optics (CLEO), Baltimore, MD, paper CWG1, (2005).

12. **J. Hu**, Y. Sun, B. S. Marks, L. Yan, G. M. Carter, and C. R. Menyuk, “Optimizing the input scrambling rate in a recirculating loop with EDFAs,” in Proc. Conference on Lasers and Electro-Optics (CLEO), San Francisco, CA, paper CFN7, (2004).

13. **J. Hu**, B. S. Marks, and C. R. Menyuk, “Design of flat-gain fiber Raman amplifiers using equally spaced pumps with fixed and optimized central wavelength,” in Proc. Conference on Lasers and Electro-Optics (CLEO), Baltimore, MD, paper CThD5, (2003).

14. G. E. Tudury, **J. Hu**, B. S. Marks, G. M. Carter, and C. R. Menyuk, “Spectral gain characteristics of an amplified hybrid Raman/EDFA 210-km link,” in Proc. Conference on Lasers and Electro-Optics (CLEO), Baltimore, MD, paper CThM52, (2003).

15. **J. Hu**, B. S. Marks, Q. Zhang, and C. R. Menyuk, “A shooting algorithm to model backward-pumped Raman amplifiers,” Lasers and Electro-Optics Society (LEOS) Annual Meeting, Tucson, AZ, paper TuI3, (2003).

Other presentations:

1. S. R. Sueoka, J. Butler, S. Montgomery, J. Shirk, S. Flom, R. Pong, B. Wright, T. Tauney, A. Rosenberg, C. Menyuk, and **J. Hu**, “Optical limiting in solid-core holey fibers,” 2007 AAS/AAPT Joint Meeting, American Astronomical Society Meeting, Seattle, Washington, paper 209.02, 2007

2. **J. Hu** “Leakage loss and bandgap analysis in air-core photonic bandgap fiber for nonsilica glasses,” UMBC CSEE graduate seminar, Oct. 10, 2006

3. J. Kim, **J. Hu**, B. Marks, C. Menyuk, U-C. Paek, and B. H. Lee, “Improved multipole method for analysis of photonic crystal fibers,” Photonics’05 T2D2, Chungmu, Korea, 2005

4. J. Kim, **J. Hu**, B. Marks, C. Menyuk, U-C. Paek, and B. H. Lee, “Cladding mode analysis of the photonic crystal fiber with two layers of holes,” Proceedings of Physics Society of Korea Fall Meeting, LP2-036, Chonju, Korea, 2005
5. J. Kim, J. E. Im, **J. Hu**, B. Marks, C. Menyuk, U-C. Paek, and B. H. Lee, “Cladding mode analysis for photonic crystal fiber by using multipole method,” COOC’05, FP-20, Daegu, Korea, 2005

Abstract

Title of Dissertation: Analysis of chalcogenide-glass photonic crystal fibers

Zhihang (Jonathan) Hu, Doctor of Philosophy, 2008

Dissertation directed by: Curtis R. Menyuk
Professor
Computer Science and Electrical Engineering

In this dissertation, we describe a theoretical study of chalcogenide-glass photonic crystal fiber designs. Light can propagate in these glasses in the wavelength region $\lambda =$ 2–11 μm, in contrast to standard silica fiber in which light does not propagate beyond $\lambda \simeq 2$ μm. Consequently, they have important defense and biomedical applications. While silica-glass photonic crystal fibers have been extensively studied, that is not true for other glasses such as chalcogenide glasses. We have carried out this study in collaboration with researchers at the Naval Research Laboratory, who have provided the data that we use as input parameters to our simulations, as well as experimental results to compare to the simulations. In this dissertation, we first analyze leaky modes using traditional, one-dimensional slab waveguides. The reason for analyzing one-dimensional waveguides is that this analysis yields theoretical results that are of

use in understanding the physics in the more complex geometry of two-dimensional waveguides. Next, we describe an investigation of the leakage loss from a finite number of air-hole rings in a photonic bandgap fiber as a function of the pitch and the refractive index. The leakage loss is due to incomplete mode confinement. It is shown that for a refractive index equal to 2.4, corresponding to chalcogenide glass at $\lambda = 4$ μm, the loss is minimal when the air-hole-diameter-to-pitch ratio equals 0.8. This result contrasts strongly with analogous results for silica fibers in which the leakage loss is minimized by making the air-hole-diameter-to-pitch ratio approach as close to 1.0 as possible. In addition to minimizing the leakage loss, the core geometry is optimized for air-core photonic bandgap fibers to decrease the effect of coupling losses to surface modes. Finally, the nonlinearity is characterized and used in simulations to study supercontinuum generation in chalcogenide fibers. The nonlinearities that must be included are the Kerr and Raman effects. After verifying that the simulation code reproduces the spectrum that was observed in experimental studies of infrared supercontinuum generation from 2.1 to 3.2 μm, we then used the code to predict that a bandwidth of more than 4 μm can be generated using an As_2Se_3-based chalcogenide photonic crystal fiber with an air-hole-diameter-to-pitch ratio of 0.4 and a pitch of 3 μm.

Analysis of chalcogenide-glass photonic crystal fibers

by

Zhihang (Jonathan) Hu

Dissertation submitted to the Faculty of the Graduate School
of the University of Maryland in partial fulfillment
of the requirements for the degree of
Doctor of Philosophy
2008

© Copyright by Zhihang (Jonathan) Hu, 2008

Dedication

To my parents Xiru and Jiexun Hu, and my sister Yiyi Hu

Acknowledgements

I am grateful to Dr. Curtis Menyuk, my dissertation advisor, for his support and guidance throughout my PhD education at UMBC. I appreciate the chance that he gave me to work within his research group. Not only did he enable my graduate studies, but he also taught me useful skills such as presentation skills, how to work in teams, and how to communicate with my colleagues. I am also grateful to Dr. Gary Carter for giving me the opportunity to collaborate with his experimental group at the Laboratory for Physical Sciences during the early stages of my PhD study.

I would also like to thank Prof. Brian Marks for his contributions to my graduate education at UMBC, and especially for spending time with me every week in the first few years of my Ph.D. studies. I would like to thank Jinchae Kim, who visited us from Gwangju Institute of Science and Technology in Korea. The discussions with him were always very helpful.

It has been a great pleasure to work with experimental groups at the Naval Research Laboratory. The research with them eventually became my dissertation topic. I would like to express my special gratitude to Brandon Shaw, Jas Sanghera, Ishwar Aggarwal, and Brian Justus.

The most interesting experience was being a part of an internationally and culturally diverse group. Many thanks to all my colleagues for the privilege of working with you: Ivan Lima, Aurenice Oliveira, Lyn Randers, Ronald Holzlöhner, Oleg Sinkin, Anisuzzaman Talukder, Anshul Kalra, Vlad Seghete, Venkat Veerasubramanian, Hai Xu, Yu Sun, Hua Jiao, Jiping Wen, Olukayode Okusaga, William Astar, Anthony Lenihan, Gaston Tudury, and to our group's professors, Vladimir Grigoryan, Li Yan, and John Zweck.

I would like to thank my friend Jack Shih, who encouraged me throughout the years during my PhD study.

I would like to express my immense gratitude to my parents Xiru and Jiexun Hu and my sister Yiyi Hu for supporting me throughout of my education.

Contents

List of Figures **viii**

1 Introduction **1**

2 Understanding leaky modes **6**

2.1 The wave equation and its solutions in slab waveguides 14

2.2 Non-leaky structures 24

2.2.1 Uniform medium 24

2.2.2 Three-layer waveguide 28

2.3 W-type slab waveguide 36

2.3.1 Leaky mode analysis 36

2.3.2 Perturbation analysis 38

2.3.3 Physical explanation of the exponential decay 40

2.3.4 Radiation mode decomposition 41

2.3.5 Comparison and analysis 45

2.4 Bandgap slab waveguide 50

2.4.1 Eigenvalue equation 50

2.4.2 Alternative solution procedures 53

2.5 Waveguide with absorbing layers 60

2.5.1 Optimization of the absorbing layer 62

2.5.2 Mode decomposition and the leaky mode 66

2.6 Answers to the introductory questions 72

3 Leakage loss and bandgap analysis for nonsilica glasses 78

3.1 Bandgap and mode analysis 79

3.2 Mode leakage loss analysis 85

4 Optimization of the operational bandwidth in air-core photonic bandgap fibers 95

4.1 Fiber geometry 96

4.2 Result and analysis 97

5 Raman response function and supercontinuum generation in chalcogenide fiber 105

5.1 Raman response function for chalcogenide fiber 106

5.2 Comparison between theory and experiment 108

5.3 Single mode analysis 112

5.4 Supercontinuum generation using four-wave mixing 114

6 Conclusion 121

Bibliography **124**

List of Figures

2.1 The refractive index profile for (a) a three-layer waveguide and (b) a W-type waveguide. 13

2.2 Comparison of (a) guided modes, (b) radiation modes, and (c) leaky modes in a one dimensional waveguide. The solid curves show the mode power outside of a center region, which depends upon the details of the waveguide index variation. 16

2.3 The normalized spectral power density $P(k_x) = |\tilde{A}(k_x)|^2 / \max[|\tilde{A}(k_x)|^2]$ and the real part of n_{eff} as a function of k_x. 26

2.4 Wave propagation in a uniform medium. Light is injected into a uniform medium at $z = 0$. The movie shows the real part of the electric field. 27

2.5 $I_{\text{norm}} = |A(z, x = 0)|^2 / |A(z = 0, x = 0)|^2$ as a function z/λ for a Gaussian beam. Blue circles represent the complete solution, while the red solid curve represents the lowest-order asymptotic approximation. 29

2.6 The normalized spectral power density $P(k_x) = |\tilde{A}(k_x)|^2 / \max[|\tilde{A}(k_x)|^2]$ and the $\text{Re}(n_{\text{eff}})$ as a function of k_x. 32

2.7 Wave propagation in a three-layer waveguide. The light is injected into the waveguide at $z = 0$. The movie shows the real part of the electric field. The black dashed lines indicate $x = \pm a$. 33

2.8 $I_{\text{norm}} = |A(z, x = 0)|^2/|A(z = 0, x = 0)|^2$ as a function of z/λ for a Gaussian beam. The blue circles represent the power calculated by solving the propagation equation, Eq. 2.4 using the complete decomposition, while the red dashed curve represents the sum of the asymptotic approximation from Eq. 2.39 and the guided mode contribution. . . . 35

2.9 Logarithm of the magnitude of the difference between the left and right hand side of Eq. 2.42. 38

2.10 Schematic illustration of the flux flow. 41

2.11 The normalized spectral power density $P(k_x) = |\tilde{A}(k_x)|^2/\max[|\tilde{A}(k_x)|^2]$ and the real part of effective index $\mathrm{Re}(n_{\text{eff}})$ as a function of k_x/k_0. . 42

2.12 Wave propagation in a W-type waveguide. Light is injected into the W-type waveguide at $z = 0$. The black dash-dotted lines and black dashed lines indicate $x = \pm a$ and $x = \pm b$, respectively. The movie shows the real part of the electric field. 45

2.13 $\mathrm{Im}(n_{\text{eff}})$ as a function of b/a. The blue solid curve, green dash-dotted curve, and red dashed curve represent the leakage loss calculated from the direct determination of the leaky mode solution, the perturbation method, and the determination from the radiation mode solution, respectively. 46

2.14 Movie of the transverse mode evolution as the mode propagates along a W-type slab waveguide. The red dashed curve and blue solid curve represent the transverse mode power from the leaky mode and the actual profile that is found by integrating Eq. 2.4. The black dashed lines indicate $x = \pm b$. 47

2.15 $I_{\text{norm}} = |A(z, x = 0)|^2/|A(z = 0, x = 0)|^2$ as a function of z/λ for a Gaussian beam with $b/a = 2.5$. The red dashed curve shows the power of the field using numerical integration. The green dash-dotted and green solid curves show respectively the steepest descent analysis for the evolution at $x = 0$ and the leaky mode evolution. The blue solid curve shows the I_{norm} that is calculated by summing the fields from the steepest descent analysis that were used to produce I and II. . . . 48

2.16 The refractive index profile for (a) an infinite periodic structure, (b) an infinite periodic structure with a center defect, and (c) a leaky bandgap waveguide. 56

2.17 Band structure as a function of normalized frequency and propagation constant. The dark area are the allowed bands. 56

2.18 Refractive index and real part of $E(x)$ as a function of x. 57

2.19 The normalized coefficient $P(K_x) = |\tilde{A}(K_x)|^2/\max[|\tilde{A}(K_x)|^2]$ with (a) linear scale and (b) logarithmic scale as a function of K_x and the real part of n_{eff}. 57

2.20 Wave propagation in a leaky bandgap waveguide. A beam is injected into the waveguide at $z = 0$. The movie shows the real part of the electric field. The black dash-dotted lines and black dashed lines indicate $x = \pm d$ and $x = \pm(d + M\Lambda)$, respectively. 58

2.21 Movie of the transverse mode evolution as it propagates along a leaky bandgap slab waveguide. The red dashed curve and blue solid curve represent the power of the leaky mode and the computational solution of Eq. 2.4. The boundary lines are not shown in this figure since they are very close to the center, as shown in Fig. 2.20. 58

2.22 $\mathrm{Im}(n_{\mathrm{eff}})$ as a function of the number of periods. The blue solid curve, green dash-dotted curve, and red dashed curve represent the leakage loss calculated from the direct determination of the leaky mode solution, the perturbation method, and the determination from the radiation mode solution, respectively. 59

2.23 Refractive index profile for a W-type waveguide with absorbing layers. 62

2.24 $\mathrm{Im}(n_{\mathrm{eff}}) = \mathrm{Im}(\beta)/k_0$ as a function of L/λ. The blue dash-dotted curve, dashed curve, and dotted curve show the results with normalized absorbing layer widths $d/\lambda = 5$, 10, and 15, respectively. The red solid curve shows the results from Eq. 2.42. 64

2.25 $\mathrm{Im}(n_{\mathrm{eff}}) = \mathrm{Im}(\beta)/k_0$ as a function of L/λ. The blue dash-dotted curve, dashed curve and dotted curve show the results with $s' = 5$, 2, and 1, respectively. The red solid curve shows the results from Eq. 2.42. . . 65

2.26 The average value of Im(n_{eff}) and the standard deviation for 100 evenly-spaced values of L/λ as we allow it to vary from 5 to 10. 65

2.27 The Re(n_{eff}) and Im(n_{eff}) for all 500 eigenmodes. 68

2.28 Movie of the transverse normalized power of the same initial Gaussian beam that we considered in Sec. 2.3.4. We also show the power of the leaky mode as a red dashed curve. We have normalized the peak of the mode power profiles to 1. The black dash-dotted lines, black dashed line, and black dotted lines indicate $x = \pm a$, $x = \pm b$, and $x = \pm L$, respectively. 69

2.29 $I_{\text{norm}} = |A(z, x = 0)|^2/|A(z = 0, x = 0)|^2$ as a function z/λ for a Gaussian beam. The red solid curve shows the result keeping all 500 modes, while the blue dashed curve shows the result keeping only the leaky mode. 70

2.30 Slide show for the input wave (blue solid curves) and its decomposition into the eigenmodes (red dashed curves). In (b), we show the central region from (a). The black dash-dotted lines, black dashed line, and black dotted lines indicate $x = \pm a$, $x = \pm b$, and $x = \pm L$, respectively. 71

3.1 Bandgap diagrams for (a) a refractive index of 1.45 with a d/Λ of 0.9 and (b) a refractive index of 2.4 with a d/Λ of 0.8, respectively. . . . 80

3.2 The contour plot for the maximum relative bandgap. The black x-marks represent the d/Λ corresponding to the maximum relative bandgap at each refractive index. Two black dashed curves connect x-marks in the two relative bandgap maxima in the contour plot. There exists a discontinuity of the maximum relative bandgap around a refractive index of 1.8. 81

3.3 Band diagram when we use a refractive index of 1.45 and a d/Λ of 0.92. Yellow indicates the largest relative bandgap. 82

3.4 Magnitude of Poynting flux, normalized to the peak, in the (a) 4th and (b) 5th band. The red regions correspond to a large Poynting flux. Most of the flux in the 4th band is located in the spots, which are the large glass regions between three holes in the triangular structure. However, most of the flux in the 5th band is located in the veins, which are the long thin connections between two spots. 83

3.5 Fill factor as a function of the d/Λ. Red dashed and blue solid curves represent the fill factor for the 4th and 5th bands, respectively. 84

3.6 Band diagram when we use a refractive index of 2.4 and an d/Λ of 0.75. Yellow indicates the largest relative bandgap. 85

3.7 (a) Red solid and dashed curves represent the lowest frequency in the 9th band and highest frequency in the 8th band as functions of the d/Λ. (b) The red dashed curve is the same as in (a). Three solid blue curves represent the normalized frequency in the Γ, M, and M-K points as a function of d/Λ. 86

3.8 The frequency dependence of the leakage loss for air-core PBGFs with 5 rings of air holes, where the d/Λ is taken as a parameter. The dashed curve represents the loss for the optimized normalized frequency with different d/Λ. We recall that normalized frequency $\omega\Lambda/2\pi c$ equals the pitch-wavelength ratio Λ/λ. Loss is calculated by using a wavelength of 4 μm and a refractive index of 2.4. 87

3.9 (a) The normalized leakage loss (loss × wavelength) as a function of refractive index. (b) The corresponding real part of the effective index. 88

3.10 Geometry and corresponding normalized mode intensity for a 5-layer air-guided PBGF corresponding to (a) the mode found by our optimization procedure without any constraints and (b) the mode found by our optimization procedure with the constraint that more than 75% of the mode power is located in the central air core. A normalized mode intensity smaller than 0.1 is not shown. 89

3.11 (a) The solid curves represent the d/Λ corresponding to minimum loss. The dashed curves with x-marks represent the d/Λ corresponding to the maximum relative bandgap. (b) Relative bandgap when the d/Λ corresponds to the dashed curve of (a). 90

3.12 The optimized normalized frequency corresponding to curves in Fig. 3.9 as a function of refractive index. 92

3.13 (a) Geometry and corresponding normalized mode intensity for a 5-layer air-guided PBGF corresponding to the minima shown in the dashed curves in Fig. 3.9. A normalized mode intensity smaller than 0.1 is not shown. 93

3.14 The loss as a function of the number of air hole rings on a logarithmic scale with the same fiber parameter. 94

4.1 Fiber geometries for PBGFs with (a) a 19-cell core and (b) a 7-cell core. 98

4.2 Contour plots of (a) power in the core and (b) $F \cdot \Lambda$ for a PBGF with a 19-cell core. 99

4.3 (a) The mode effective index as a function of normalized frequency at a normalized ring thickness of 0.05. The blue solid and dashed curves represent the fundamental air-guided mode and surface modes, respectively. The black dashed lines represent the edge of the bandgap. (b) The comparison between power in the core and normalized factor $F \cdot \Lambda$ for a PBGF with a 19-cell core. Black dash-dotted line indicates $F \cdot \Lambda = 1.6$. (c) The relative mode intensity profiles correspond to points I, II, and III in (a). 101

4.4 Relative operational bandwidth as a function of normalized ring thickness. 102

4.5 The relative operational bandwidth for different glass refractive indices with a normalized ring thickness of 0.04. 102

4.6 Contour plots of (a) power in the core and (b) $F \cdot \Lambda$ for a PBGF with a 7-cell core. 103

5.1 (a) The imaginary part of third-order susceptibility, which is proportional to the Raman gain. It has been normalized to unity at the peak gain. (b) The real part of the third-order susceptibility is shown in the same arbitrary units. 109

5.2 Raman response function. In these figures, the blue solid curve and the red dashed curve represent chalcogenide fiber and silica fiber, respectively. 110

5.3 (a) The dashed curve and solid curve represent material dispersion for chalcogenide glass and total dispersion for a chalcogenide PCF with one air-hole ring, respectively. 110

5.4 The blue solid curve and the red dashed curve show the simulation result and corresponding experimental result [26]. 111

5.5 The effective index of the fundamental space-filling mode n_{FSM} as a function of the ratio of wavelength to pitch, λ/Λ, with different ratios of hole diameter to pitch, d/Λ. 111

5.6 The curves corresponding to $V_{\text{eff}} = 2.405$ for different refractive indices of glass. The red, blue, and green solid solid curves represent refractive indices of 1.45, 2.4, and 2.8, respectively. 112

5.7 The phase-matching diagram is calculated for an As_2Se_3-based chalcogenide PCF. The blue solid, dashed, and dotted curves present the phase-matching conditions for peak powers of 1, 0.1, and 0 kW, respectively, with $d/\Lambda = 0.4$ and $\Lambda = 3$ μm. The red dash-dotted curve presents the phase-matching condition for a peak power of 0.1 kW for PCF with $d/\Lambda = 0.4$ and $\Lambda = 2.5$ μm. 115

5.8 The output spectrum using a As_2Se_3-based PCF with $d/\Lambda = 0.4$ and $\Lambda = 3$ μm. The input pulse has a FWHM of 500 fs. The input peak power is set at 1 kW. 115

5.9 Movie of a simulation of the spectrogram as the wave propagates along the PCF. The black solid curve shows the group delay with respect to the wave at 2.5 μm. 116

5.10 The dispersion curve for PCF with $d/\Lambda = 0.4$ and $\Lambda = 3$ μm. 117

5.11 The total generated bandwidth as a function of Λ. 118

5.12 The total generated bandwidth as a function of the FWHM of the input pulse. 118

5.13 Spectrograms with (a) an input FWHM of 600 ps and (b) an input FWHM of 650 ps. 119

5.14 The total generated bandwidth as a function of input peak power. . . 119

Chapter 1

Introduction

Photonic crystal fibers (PCFs) were first explored in the 1970's [1]. In the past several years, progress in fabrication technology has led to a rapid development of new types of PCFs [2]–[5]. A variety of fibers with useful characteristics not achievable using standard fibers have been proposed and many of the most interesting properties have been realized in university or industrial laboratories. PCFs offer increased flexibility in the dispersive, nonlinear, and polarization properties of fiber [6]–[8]. Index-guided PCFs, which have one hole missing in the center, guide light through total internal reflection. Air-core PCFs, or photonic bandgap fibers (PBGFs), guide light through the photonic bandgap effect, which is a completely different effect from the usual index guiding in optical fibers. Due to the air core, the nonlinearity is dramatically reduced. This reduction has already become important in the high-power delivery of laser light [9] and may become important in optical communications [10], [11]. A large amount of research has been done on silica PCFs [12]. However, silica glass cannot be used for infrared (IR) transmission because of its high material loss. This dissertation is concerned with investigating chalcogenide-glass PCF that is used for IR transmission.

For IR transmission, chalcogenide PCFs are preferred [13]. Chalcogenide glasses are based on the chalcogen elements sulfur (S), selenium (Se), and tellurium (Te), with the addition of other elements such as germanium (Ge), arsenic (As), and antimony (Sb). The refractive index of chalcogenide glass varies between 2.2 and 2.8, depends on the glass composition [14]. These glasses have been shown to be chemically and mechanically durable and have low loss at IR wavelengths [15]. Chalcogenide fibers are well suited for chemical sensing applications based on analyzing attenuated total reflection (ATR) spectra [16]. Another important application using chalcogenide glass is fiber beam delivery of mid-infrared light from a CO_2 laser for medical applications [17]. Delivery of tens of watts from a CO_2 laser which is at a wavelength of 10.6 μm has been demonstrated [9]. Recently, supercontinuum generation using a chalcogenide PCF with one ring of air holes has been demonstrated, and the Raman gain spectrum for a step index chalcogenide fiber has been measured by a group at the Naval Research Laboratory [15], [18], [19]. However, a detailed study for a PCF with an optimized structure for supercontinuum generation using nonsilica glasses, especially chalcogenide glass, has not previously been made.

In order to understand the fiber property for PCFs, it is crucial to understand the modes that are supported by PCFs. Due to the finite number of air hole rings, the modes in the PCFs are leaky modes. Computational methods for determining the complex propagation constants of leaky waveguide modes have become so powerful and so readily available that it is possible to use these methods with little understanding of what they are calculating. In this dessertation, we first give a tutorial introduction. We compare different computational methods for calculating the propagation constants of the leaky modes, focusing on the relatively simple context of a W-type slab waveguide. In a lossless medium with infinite transverse extent, we compare a direct determination of the leaky mode to a complete mode decomposition. The direct determination of leaky mode is a mode matching method that is analogous to the multipole method in two dimensions. We then compare these results to a simple finite-difference scheme in a transverse region with absorbing boundaries that is analogous to finite-difference or finite-element methods in two dimensions. While the physical meaning of the leaky modes in these different solution methods is different, they all predict a nearly identical evolution for an initial, nearly-confined mode profile over a limited spatial region and a limited distance.

Air-core photonic bandgap fibers (PBGFs), in contrast to some other types of holey fibers, guide light through the photonic bandgap effect, instead of using total internal reflection [10], [11]. PBGFs have the potential to provide very low-loss transmission, along with delivery of high power and low nonlinearity. Research on silica fiber shows that a larger air-hole-diameter-to-pitch ratio, d/Λ, in air-core PBGFs leads to wider bandgaps and hence better mode confinement [20]. Pitch, Λ, is defined as the distance between the centers of the nearby holes. Pottage, *et al.* suggest using lower d/Λ to obtain a wider bandgap for high-index glass [21]. The assumption is that a wider relative bandgap leads to lower leakage loss. However, the loss due to mode leakage in high-index glass with lower d/Λ has not been previously calculated, and this assumption remains unverified. We calculate the relative bandgap when we vary the d/Λ and the refractive index, and compare the d/Λ for the minimum loss and maximum relative bandgap. It is found that they coincide for a wide range of refractive index.

In PGCFs, the core mode has its mode power inside the central air hole. Additionally, there exists another kind of mode called a surface mode. The surface modes, which are located between the core and the cladding, have been shown to have significant impact on the loss of the fundamental mode [22]. The confinement mechanism is the bandgap effect on the large-radius (outer) side of the mode and internal reflection on the small-radius (inner) side of the mode. The surface mode interact with core modes and decrease the operational bandwidth of the core modes. Amezcua-Correa, *et al.* [23], [24] demonstrated that by carefully selecting the thickness of the inner glass ring around the core, it is possible to push the surface modes away from the center of bandgap in silica PBGFs. Hence, it is interesting to know what kind of geometry should be drawn for chalcogenide fiber to push the surface modes away from the center of bandgap.

The use of a solid core PCF for supercontinuum generation is particularly attractive since a small effective area can be realized, which increases fiber nonlinearity, and the zero group-velocity dispersion (GVD) can be tailored to maximize supercontinuum generation [25]. Conventional optical fibers are made from silica, because silica-glass fibers are easy and relatively inexpensive to manufacture. However, the output of the spectrum is limited by the material loss of the silica fiber to below 2 μm. Supercontinuum generation at IR wavelengths up to 10 μm [15] is however possible using chalcogenide-based PCFs. The Raman spectrum, which is proportional to the imaginary part of the third-order susceptibility, has been measured in a step-index chalcogenide fiber. The time-domain Raman response function is then calculated from the Raman spectrum. Using the nonlinear response function of the chalcogenide fiber, which includes both the instantaneous (Kerr) response and the delayed (Raman) response, we theoretically reproduce the measured bandwidth of the supercontinuum generation in Ref. 26. We then theoretically find that a bandwidth of more than 4 μm can be generated using an As_2Se_3-based chalcogenide photonic crystal fiber with an air-hole-diameter-to-pitch ratio of 0.4 and a pitch of 3 μm.

The remainder of this dissertation is organized as follows: In the second chapter, we describe wave propagation in a uniform medium, three-layer slab waveguide, W-type slab waveguide, bandgap slab waveguide, and W-type slab waveguide with absorbing layers. We describe the leaky modes in a W-type slab waveguide and bandgap slab waveguide.

In the third chapter, we show the minimum leakage loss and maximum relative bandgap as a function of the d/Λ in a photonic bandgap fiber for a refractive index between 1.4 and 2.8. The mode properties for maxima of the relative bandgap are analyzed as the air-hole-diameter-to-pitch ratio and the refractive index are varied.

In the fourth chapter, we present the optimal inner glass ring thickness and its dependence on the glass index in infrared PBGFs.

In the fifth chapter, we show the Raman response function and supercontinuum generation in chalcogenide fiber. Using measured Raman spectrum and dispersion, we modeled and reproduced the experimental bandwidth of IR supercontinuum generation using a chalcogenide PCF. We then optimized the PCF structure to generate supercontinuum in IR region. These results are presented in this chapter.

The sixth chapter contains the conclusions that summarize the main results of the dissertation.

Chapter 2

Understanding leaky modes

In the 1960s and 1970s, the optical modes in solid-state and waveguides were the subject of intensive study [27]–[30]. The waveguides that could be made then were fairly simple; a higher index material was typically embedded in a lower index material with a slab or rectangular waveguide in the case of semiconductor waveguides and a step or graded index waveguide in the case of optical fibers. In the past decade, it has become possible to make highly-complex optical waveguides in both semiconductors and glass, and, as a consequence, the study of optical waveguides has undergone a renaissance. A number of highly-sophisticated computational algorithms have been developed to find the modes and their propagation constants inside these waveguides, including the finite-element method [31]–[33], the finite-difference method [32], [34], the multipole method [35], [36], the Galerkin method [37], and the plane-wave method [38], [39]. In general, the modes in these modern waveguides may be evanescent or leaky even when there are no material losses. The finite-difference method, the finite-element method and the multipole method allow one to determine the mode profiles and attenuation. Commercial finite-difference and finite-element solvers have in practice become so sophisticated and at the same time so easy to use that it is possible to determine mode profiles and their complex propagation constants with little understanding of what a complex propagation constant really means.

There is in fact a serious conceptual issue with leaky modes. Strictly speaking, they are not modes of the infinite lossless transverse waveguide. In principle, given any initial transverse profile at the beginning of a waveguide, one can decompose that profile into a finite number of guided modes and a continuum of radiation modes. These modes then propagate without attenuation in a lossless medium, and any attenuation of an initial profile that occurs must be due to spreading of the radiation modes. So, what is it that the finite-element, the multipole method, or other mode solvers are finding?

Leaky modes appear when an initial profile is nearly guided. In the three-layer slab waveguide shown in Fig. 2.1(a), in which $n_1 > n_0$, at least one guided mode exists. By contrast, in the five-layer W-type slab waveguide, shown in Fig. 2.1(b), with $n_1 < n_0$, only continuum radiation modes still exist. Nonetheless, when the width of the lower-index region becomes large, an optical beam is observed that looks much like the guided mode that would exist if the outer, higher-index layer were not present. This beam attenuates exponentially with a rate that decreases rapidly as the width of the lower-index layer increases. How do we mathematically relate the radiation modes that compose this nearly-guided waveguide to the guided mode that exists in the absence of the outer higher-index layers? Why is the attenuation in the W-type waveguide exponential?

Exponential attenuation is not the only possibility. If we send light into a medium with a single index of refraction n_0, then the light diffracts and its intensity diminishes algebraically, rather than exponentially. This algebraic decay occurs because the light is not even partially confined. When the light comes from a point source, the algebraic decay is proportional to the square of the inverse distance from the source, since the light spreads in both transverse dimensions. When the light source is extended in one dimension, then the algebraic decay is proportional to the inverse of the distance, since light spreads in only one dimension. In a purely diffractive medium, the mode solvers will not find a single mode. In leaky mode waveguides, most of the energy will eventually leak out from the nearly-guided waveguide, and the light will then diffract. When does diffraction dominate and the exponential decay of the leaky modes become algebraic?

A further issue with leaky modes is that at sufficiently large transverse distances from the mode center they increase exponentially. This behavior is clearly unphysical in the limit $x \to \pm\infty$. What is its origin? Is an exponential increase away from the transverse center ever visible?

The waveguides shown in Fig. 2.1 are quite simple. Is the behavior in more complex waveguides, in particular bandgap or photonic crystal waveguides, qualitatively similar? Can bandgap waveguides be studied using the same methods as in the case of the simpler W-type waveguides?

A related issue is that one normally applies the finite-difference or the finite-element method by using a finite lossless region that is surrounded by absorbing layers or regions. The purpose of the absorbing regions is to avoid reflections and simulate outward-going boundary conditions. so that inside the lossless region, the solution approximates the solution with the same initial conditions that one would find in a lossless medium of infinite transverse extent. However, the problem that one is solving, even in the limit as the discretization grows finer, is in fact fundamentally different from the problem of a lossless medium of infinite transverse extent and a lossless medium. Are the leaky modes real modes in this system? Do they still grow exponentially in the direction transverse to the propagation, at least in the lossless regions? Is there an analog to diffraction? What is the mode decomposition in this case? Finally — and perhaps most important — is the behavior that is predicted in this case the same as in the case of a lossless medium of infinite extent?

The answers to these questions may be found scattered throughout the technical literature, but not together and not in a form that is easily accessible to newcomers to the study of optical waveguides. The discussions rely on steepest descent method for evaluating integrals and other asymptotic methods, whose physical meaning may not always be clear. In this introductory tutorial, our goal is to answer all these questions and to show the relationship among them. We will present the mathematical basis for these answers, but, at the same time, we will present pictures and animations whose goal is to illuminate what is happening both mathematically and physically.

We will focus here on simple one-dimensional slab waveguides, although two-dimensional waveguides are more important in practice. All the questions that we posed can be answered within the context of one-dimensional waveguides. No new concepts appear in two dimensions, although the mathematical complexity increases. Moreover, it is far simpler to illustrate the phenomena through pictures and animations since one less dimension must be kept. Further discussion of the mathematical methods in two dimensions may be found in the textbooks by Marcuse [40] and by Snyder and Love [41].

For historical interest, we note that leaky modes were first described in the context of microwave waveguides, and both the textbooks by Marcuse and by Snyder and

Love refer to a classic textbook by Collins [42], who refers in turn to reports by Barone [43], [44] that appeared in 1956 and 1958. These reports are part of a series of reports from the Brooklyn Polytechnic Institute in which the leaky mode concept was first described. The first archival article reference is a brief report by Marcuvitz [45], who noted the close analogy to quantum-mechanical tunneling. This paper stated that leaky modes are not members of a complete set of orthogonal basis functions. He noted that this solution to the wave equation gives field representation in a center range with a complex propagation constant, but that the field becomes infinite at the infinite transverse spatial limit. A series of papers by Tamir, Oliner, and their colleagues, begun shortly thereafter, summarize and categorize the possible behavior of a leaky mode [46]–[51]. The first measurement of a leaky mode was carried out in 1961 by Cassedy, *et al.* [52]. They confirmed the existence of a leaky wave due to a line current source above a grounded dielectric slab [52]. Hall and Yeh presented both theory and experiment for heteroepitaxial deposition of ZnS or ZnSe on GaSe, which is a three-layer waveguide [53]. In their experiment, the index of the substrate is higher than that of the center layer. Hence, only leaky modes can exist in this waveguide; no guided mode can exist. The same refractive index variation with position also occurs in waveguides with GaAlAs layers on GaAs substrates [54]. In 1975, the W-type, or depressed-cladding, slab waveguide was analyzed by Suematsu and Furuya [55]. At about the same time, the theory for W-type fiber was developed by Kawakami and Nishida [56], [57]. The original leaky wave analysis for a cylindrical waveguide was carried out in 1969 [58], [59], which is 13 years after the leaky wave theory for a slab waveguide was first presented [43]. The attenuation coefficient of leaky modes has been obtained by solving the appropriate eigenvalue equation [53], [56], [57], [59]–[61], using Poynting's vector theorem [62]–[65], and by using ray optics [65]–[68]. For the multilayer slab waveguide, the mode-matching method has been extensively used to find leaky modes [69]–[71].

We do not discuss the ray optics method, and, given its historical importance, this omission requires comment. Historically, ray optics was used in the analysis of optical waveguides to find reasonably accurate analytical approximations to Maxwell's equations in contexts where exact analytical solutions could not be obtained. This approximation requires in principle the wavelength of the light in the waveguide to be "small" compared to the waveguide's dimensions. What "small" means in this context is difficult to precisely define, and the attempt is rarely made. When the leakage is due to partial refraction, as in the case of a mode just below cutoff, ray optics can provide a reasonably accurate estimate of the leakage [41], along with a physical picture that some find compelling [41], [72]. However, when the leakage is due to tunneling, as in the slab waveguide examples presented in this tutorial, there is no refraction, and in principle no leakage in the limit of small wavelengths. So, ray optics cannot be used without additional, *ad hoc* assumptions. Moreover, ray optics, in contrast to mode-matching methods and finite-difference or finite-element methods, is ill-suited for use in computational mode solvers. That is particularly the case in the complex geometries that are becoming increasingly common. As a consequence, it has been little used in recent years for waveguide analysis.

The rest of this paper is organized as follows: In chapter 2.1, we show the wave equation and its solutions in slab waveguides. Chapter 2.2 shows wave propagation and asymptotic analysis in non-leaky waveguides for a uniform medium and a three-layer slab waveguide. Chapter 2.3 shows the analysis for a W-type slab waveguide.

Chapter 2.4 shows the analysis for a bandgap slab waveguide. Chapter 2.5 shows the analysis for a W-type slab waveguide with absorbing layers. In chapter 2.6, we provide answers to the introductory questions.

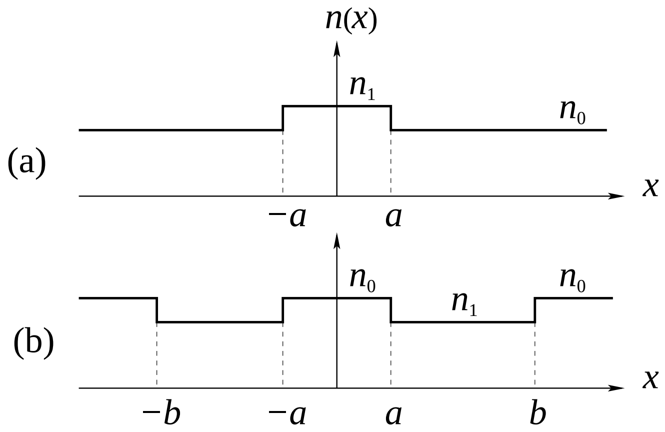
n(x)
n_1
n_0
(a)
x
−a
a
n_0
n_1
n_0
(b)
x
−b
−a
a
b

Figure 2.1: The refractive index profile for (a) a three-layer waveguide and (b) a W-type waveguide.

2.1 The wave equation and its solutions in slab waveguides

When polarization effects can be ignored, so that the electric field vector can be represented by a single component of the vector, then the field in optical waveguides can be approximately described by the scalar Helmholtz equation [32], [73]. When we restrict our study to one transverse dimension, as shown in Fig. 2.1, this equation becomes

$$\frac{\partial^2 A(z,x)}{\partial z^2} + \frac{\partial^2 A(z,x)}{\partial x^2} + k_0^2 n^2(x) A(z,x) = 0, \tag{2.1}$$

where z and x denote the dimensions along and transverse to the waveguide, $A(z,x)$ is the complex electric field, normalized so that $|A(z,x)|^2$ is the power per unit length, k_0 is the propagation constant in vacuum, which is equal to the ratio of the angular frequency to the speed of light ω/c, and $n(x)$ is the index of refraction. Here, we will assume that $n(x)$ is purely real, so that the waveguide has no material losses. Throughout this chapter, we will refer to power per unit length as simply power. We will also use the negative carrier frequency convention in which all fields vary proportional to $\exp(-i\omega t)$, where $i = \sqrt{-1}$. While this convention is common among physicists, electrical engineers typically use the positive carrier frequency convention in which all fields vary proportional to $\exp(j\omega t)$, where $j = \sqrt{-1}$. The optics literature is split, and one occasionally finds the positive carrier frequency convention along with the use of $i = \sqrt{-1}$, as in [41]. The reader of the optics literature must always check which convention is being used, since the authors are often not explicit.

While Eq. 2.1 is only approximate in general, it becomes exact when the electric field only has a y-component, as in the case of a TE mode. Moreover, the basic behavior of leaky modes remains unchanged when the full-vector Maxwell's equations are used. Likewise, the basic behavior is unchanged when instead of one transverse dimension, two transverse dimensions are considered. If we search for solutions to Eq. 2.1 of the form

$$A(z,x) = E(x)\exp(i\beta z - i\omega t), \tag{2.2}$$

we find that $E(x)$ obeys the equation

$$\frac{d^2E(x)}{dx^2} + [k_0^2 n^2(x) - \beta^2]E(x) = 0, \tag{2.3}$$

where the eigenvalue β corresponds to the propagation constant in the z-direction.

In slab waveguides with the property that $n(x)$ is equal to some constant value n_0 when $|x|$ is larger than some value x_0, there are three qualitatively different types of solutions that can appear, as shown in Fig. 2.2. Beyond $|x| = x_0$ where $n = n_0$, the field $E(x)$ must be expandable in the form $E(x) = E_0\exp(ik_x x)$, where $k_x = \pm(k_0^2n_0^2 - \beta^2)^{1/2}$. First, as shown in Fig. 2.2(a), if β is real and $k_0^2n_0^2 - \beta^2 < 0$, then $k_x = \pm i\alpha$ is purely imaginary and the field decays exponentially when $|x| > a$ as $x \to \pm\infty$. These solutions are guided mode solutions. Second, as shown in Fig. 2.2(b), if β is real and $k_0^2n_0^2 - \beta^2 > 0$, then k_x is purely real, and the field oscillates when $|x| > b$ as $x \to \pm\infty$. These solutions are radiation mode solutions. Only a finite number of β-values, which may equal zero, may be found for which $k_0^2n_0^2 - \beta^2 < 0$, and for which Eq. 2.3 has guided mode solutions. By contrast, radiation mode solutions may be found for any value for which $k_0^2n_0^2 - \beta^2 > 0$ [74].

The guided modes and the radiation modes constitute a complete set, by which we mean that any physically reasonable initial condition $A(x, z = 0)$ can be expanded as a superposition of guided modes and radiation modes [74], [75]. Leaky mode solutions

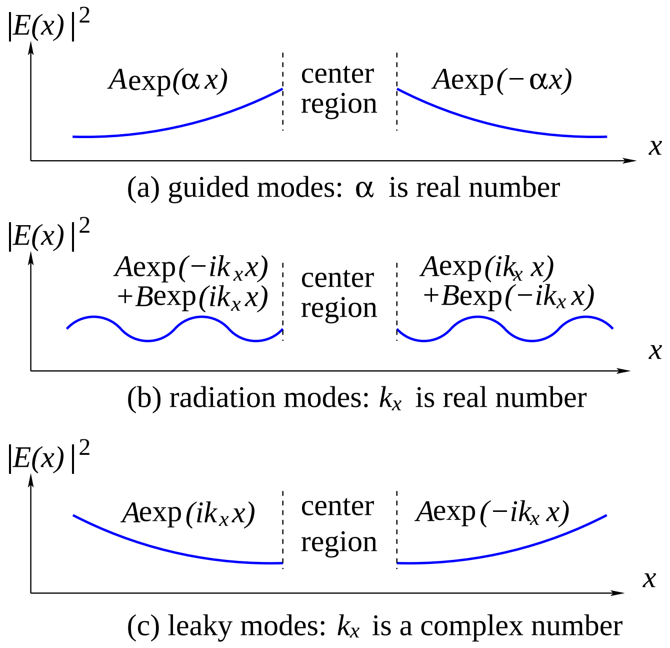
$|E(x)|^2$
Aexp(αx)
center region
Aexp(−αx)
x
(a) guided modes: α is real number
$|E(x)|^2$
Aexp(−ik_x x) +Bexp(ik_x x)
center region
Aexp(ik_x x) +Bexp(−ik_x x)
x
(b) radiation modes: k_x is real number
$|E(x)|^2$
Aexp(ik_x x)
center region
Aexp(−ik_x x)
x
(c) leaky modes: k_x is a complex number

Figure 2.2: Comparison of (a) guided modes, (b) radiation modes, and (c) leaky modes in a one dimensional waveguide. The solid curves show the mode power outside of a center region, which depends upon the details of the waveguide index variation.

of the sort shown in Fig. 2.2(c) are not part of this complete set. Equation 2.3 is self-adjoint, which implies that it is possible to choose both the guided mode solutions and the radiation mode solutions that make up the complete set so that they are all real. In all the examples that we will consider, the index of refraction $n(x)$ is symmetric, *i.e.*, $n(x) = n(-x)$. The asymmetric case is more complicated, but the basic behavior is unchanged [40], [41]. In the symmetric case, it is possible to choose the solutions to Eq. 2.3 so that they are even or odd, and we may write

$$A(z=0,x) = \sum_{l=1}^{N} \tilde{A}_l E_l(x) + \frac{1}{\pi}\int_0^\infty \tilde{A}_e(k_x) E_e(k_x,x)dk_x + \frac{1}{\pi}\int_0^\infty \tilde{A}_o(k_x) E_o(k_x,x)dk_x, \tag{2.4}$$

where N is the number of guided mode solutions, which may equal zero, the $E_l(x)$ are the guided mode solutions to Eq. 2.3, the $E_e(k_x,x)$ are the even radiation modes, and the $E_o(k_x, x)$ are the odd radiation modes. The $E_l(x)$, $E_e(k_x, x)$, and $E_o(k_x, x)$ are all mutually orthogonal. If in addition we choose them to be orthonormal and real, so that

$$\int_{-\infty}^{\infty} E_l(x) E_m(x) dx = \delta_{lm}, \tag{2.5.a}$$

$$\int_{-\infty}^{\infty} E_e(k_x, x) E_e(k'_x, x) dx = \pi\delta(k_x - k'_x), \tag{2.5.b}$$

$$\int_{-\infty}^{\infty} E_o(k_x, x) E_o(k'_x, x) dx = \pi\delta(k_x - k'_x), \tag{2.5.c}$$

then we find that

$$\tilde{A}_l = \int_{-\infty}^{\infty} A(z = 0, x) E_l(x) dx, \tag{2.6.a}$$

$$\tilde{A}_e(k_x) = \int_{-\infty}^{\infty} A(z = 0, x) E_e(k_x, x) dx, \tag{2.6.b}$$

$$\tilde{A}_o(k_x) = \int_{-\infty}^{\infty} A(z = 0, x) E_o(k_x, x) dx. \tag{2.6.c}$$

Equation 2.6.b and 2.6.c are analogous to cosine and sine transforms. It is possible and often useful to define an analog to the Fourier transform by writing $\tilde{A}(k_x) = \tilde{A}_e(k_x) - i\tilde{A}_o(k_x)$, $E(k_x, x) = E_e(k_x, x) + iE_o(k_x, x)$, $\tilde{A}(-k_x) = \tilde{A}^*(k_x)$ and $E(-k_x, x) = E^*(k_x, x)$. We now find that Eq. 2.4 becomes

$$A(z = 0, x) = \sum_{l=1}^{N} \tilde{A}_l E_l(x) + \frac{1}{2\pi} \int_{-\infty}^{\infty} \tilde{A}(k_x) E(k_x, x) dk_x, \tag{2.7}$$

and Eqs. 2.6.b and 2.6.c become

$$\tilde{A}(k_x) = \int_{-\infty}^{\infty} A(z = 0, x) E^*(k_x, x) dx. \tag{2.8}$$

We note that $E_e(k_x, x) \propto \cos[k_x x + \phi_e(k_x)]$ and $E_o(k_x, x) \propto \sin[k_x x + \phi_o(k_x)]$ when $x > |x_0|$ with $E_e(k_x, x) = E_e(k_x, -x)$ and $E_o(k_x, x) = -E_o(k_x, -x)$ when $x < |x_0|$, where in general $\phi_e(k_x) \neq \phi_o(k_x)$, and we recall that x_0 is the value of $|x|$ beyond which $n(x) = n_0$. As a consequence $E(k_x, x)$ contains components proportional to both $\exp(ik_x x)$ and $\exp(-ik_x x)$ as $x \to \pm\infty$. If the initial field consists of purely forward-going waves in the z-direction, as would be the case for a beam that is externally injected into a waveguide, then we may write the solution for all z as

$$A(z, x) = \sum_{l=1}^{N} \tilde{A}_l E_l(x) \exp(i\beta_l z) + \frac{1}{2\pi} \int_{-\infty}^{\infty} \tilde{A}(k_x) E(k_x, x) \exp[i\beta(k_x) z] dk_x, \tag{2.9}$$

where we recall that $\beta(k_x) = (k_0^2 n_0^2 - k_x^2)^{1/2}$. When $k_x^2 > k_0^2 n_0^2$, $\beta(k_x) = i(k_x^2 - k_0^2 n_0^2)^{1/2}$, and these contributions to the solution are purely decaying. The energy in these components will be reflected backwards.

While this formalism is completely general and allows one to determine in principle the evolution of a wave along a waveguide starting from any initial condition, the inclusion of radiation modes in the analysis is usually difficult since one must integrate over the continuum of modes, and an exact solution is rarely available. When the problem is discretized for a numerical solution, the number of modes that must be included in the analysis is typically quite large. Moreover, this formalism often fails to capture the essence of the physics. The contribution from the continuous spectrum of radiation modes can be replaced approximately by a summation of discrete modes, which are called leaky modes [76]. If we consider for example the three-layer waveguide shown in Fig. 2.1(a), then it will have at least one guided mode. By contrast, if we consider the W-type waveguide shown in Fig. 2.1(b), then it has no guided mode solutions, and any solution must be expressible in terms of the radiation modes. At the same time, it is intuitively clear that when $b \gg a$, the W-type waveguide must have solutions that closely resemble the guided mode solution to the waveguide in Fig. 2.1(a), and indeed such solutions can be observed to propagate with a slow exponential decay when an initial condition corresponding to the guided mode in the three-layer waveguide is launched in the W-type waveguide.

In fact, one can find solutions to Eq. 2.3 for the W-type waveguide that have nearly the same profiles in some range around $x = 0$ as the profiles that we observed computationally when an initial condition that corresponds to the guided-mode solution in the three-layer waveguide is launched in the W-type waveguide. These leaky mode solutions have complex propagation constants β, and the attenuation rate corresponds to what is observed computationally. However, the leaky mode solutions have the uncomfortable property that they grow exponentially as $x \rightarrow \pm\infty$, as shown schematically in Fig. 2.2(c), so that beyond some range of $|x|$, they no longer resemble the computationally-observed solution. We will show later that this exponential growth is required by flux conservation. While these leaky modes can be very useful in practice, and, as noted in the Introduction, they are often what is found by computational mode solvers, they are not normalizable and thus are not part of a complete set of basis functions on the infinite line in the usual sense. While mathematical work is ongoing to explore some unusual senses in which leaky modes are part of a complete set on the infinite line [72], this work is in its early stages and will not be discussed here.

In this discussion, we have assumed thus far that the index of refraction $n(x)$ becomes equal to the same value n_0 as $x \rightarrow \pm\infty$. In a slab waveguide, it is possible for these limits to be different. In that case, instead of just the three possibilities shown in Fig. 2.2, additional possibilities appear [46], [48]. As a consequence, the complete mode decomposition, shown in Eq. 2.7 becomes more complicated. However, the basic behavior is unchanged by this added complexity. Any mode that grows exponentially as $x \to +\infty$ or as $x \to -\infty$ cannot be part of a complete set of basis functions since they do not satisfy the boundary conditions.

In Secs. 3–5 of this tutorial, we will be presenting computational solutions of Eq. 2.4 or Eq. 2.9. In numerical calculations, one has a finite spatial window. A boundary condition should be enforced that ensures that the discretized equations remain self-adjoint [74] and leads to an orthogonal set of basis functions. In a uniform medium with periodic boundary conditions, this orthogonal set will be uniformly spaced in k_x and will be doubly-degenerate, allowing the use of complex exponents as a basis set [74], [77]. In effect, we are discretizing Eq. 2.9. However, in more complex waveguides, like the three-layer waveguide that we will consider in Sec. 2.2, the W-type waveguide that we will consider in Sec. 2.3, and the bandgap waveguides that we will consider in Sec. 2.4, it is no longer possible to choose the even and odd modes with self-adjoint boundary conditions so that they are degenerate. Hence, we must in effect discretize Eq. 2.4 with difference choices of the k_x-values for the even and the odd modes. In all cases except for the uniform medium, we use Neumann boundary conditions, which means that the derivatives of $E(k_x, x)$ are zero at the ends of the transverse spatial window. In all our computational examples, we pick initial conditions that are initially symmetric around $x = 0$, so that $\tilde{A}_0(k_x) = 0$, and we will only need to determine $\tilde{A}_0(k_x)$ at the allowed values of k_x for the even modes. We keep anywhere from 1,000–20,000 k_x-modes, and the boundaries of our spatial window, $x = \pm B$, are chosen so that B is hundreds to thousand of times larger than the initial beam width. We checked these values in every simulation to ensure that they are large enough, so that all our figures are unaffected by numerical errors. The number of modes and the spatial window must be large to ensure that we have good spatial resolution, while at the same time the field remains equal to zero at the spatial boundary over the entire propagation. We choose $\lambda = 1\ \mu$m in all cases except for the bandgap waveguides in Sec. 2.4. One can obtain results for different wavelengths by scaling the wavelength, the waveguide dimensions, and the mode fields, since Maxwell's equations are scale invariant [78].

When the medium becomes lossy beyond some value in $|x|$ as $x \to \pm\infty$, as is always assumed in computational mode solvers based on the finite-difference or finite-element methods, then the decomposition of an initial condition into a complete set of modes changes in important ways. First, all modes decay exponentially as $x \to \pm\infty$, and there are an infinite number of discrete modes. Hence, any initial condition may be written in the form

$$A(z=0,x) = \sum_{l=1}^{\infty} \tilde{A}_l(x) E_l(x), \tag{2.10}$$

so that

$$A(z,x) = \sum_{l=1}^{\infty} \tilde{A}_l(x) E_l(x) \exp(i\beta_l z). \tag{2.11}$$

Radiation modes and leaky modes are no longer present. However, when guided modes exist in the lossless waveguide, there are modes in discrete set of Eq. 2.10 that closely resemble the guided modes. Likewise, when leaky modes exist, there are modes in this discrete set that closely resemble the leaky modes up to the values of $|x|$ where the waveguide becomes lossy. A second major difference from the lossless case is that Eq. 2.3 is no longer self-adjoint. As a consequence, both $E_l(x)$ and β_l become complex, and $E_l^*(x)$ is not a solution of Eq. 2.3. However, Eq. 2.3 is symmetric, by which we mean that

$$\int_{-\infty}^{\infty} f(x)\left\{\frac{d^2}{dx^2}+[k_0^2 n(x)-\beta^2]\right\}g(x)dx$$
$$=\int_{-\infty}^{\infty} g(x)\left\{\frac{d^2}{dx^2}+[k_0^2 n(x)-\beta^2]\right\}f(x)dx \tag{2.12}$$

for any $f(x)$ and $g(x)$ for which the integrals exist. As a consequence, the $E_l(x)$ are self-dual and we may determine the $\tilde{A}_l$ by using the relation

$$\tilde{A}_l=\int_{-\infty}^{\infty} A(z=0,x)E_l(x)dx. \tag{2.13}$$

The appropriate normalization condition is

$$\int_{-\infty}^{\infty} E_l^2(x)dx=1, \tag{2.14}$$

which sets the overall phase as well as the amplitude of $E_l(x)$. Because $E_l(x)$ is complex, one might worry that the integral in Eq. 2.14 could equal zero, in which case $E_l(x)$ is not normalizable. However, that cannot happen at least for any finite discretization because Eq. 2.3 is symmetric and hence normal [79].

In the reminder of the chapter, we will elucidate the relationship between the leaky modes and the modes that form a complete basis set in the lossless guide, as describe in Eqs. 2.4–2.9. We will also elucidate the relationship between the leaky modes and the modes in a lossy waveguide, as described in Eqs. 2.10, 2.11, 2.13, and 2.14. While these two descriptions are quite different, we will find that the they yield nearly identical behavior for nearly-confined light over some range of $|x|$ and

$|z|$. We will also elucidate the relationship between the leaky modes and the modes that are found by computational mode solvers.

2.2 Non-leaky structures

In this section, we consider two non-leaky waveguides that we will compare to the leaky waveguides. The first is a uniform waveguide in which simple diffraction occurs, and the intensity decays algebraically rather than exponentially as $z \to \infty$. The second is the three-layer waveguide shown in Fig. 2.1(a).

2.2.1 Uniform medium

In this case, we only have radiation modes, and they are the standard Fourier modes. Referring to Eq. 2.9, we find $N = 0$ and $E(k_x, x) = \exp(ik_x x)$. It follows that at any point z along the waveguide we may write

$$A(z,x) = \frac{1}{2\pi} \int\limits_{-\infty}^{\infty} \tilde{A}(k_x) \exp[ik_x x + i\beta(k_x)z] dk_x, \tag{2.15}$$

where $\tilde{A}(k_x) = \int\limits_{-\infty}^{\infty} A(z=0,x) \exp(-ik_x x) dx$.

In most cases, it is not possible to find an analytical solution to Eq. 2.15. An important exception is when the beam is initially Gaussian-distributed so that $A(z = 0, x) = A_0 \exp(-x^2/2w^2)$, where w is the initial beam width. In this case, we find

$$\tilde{A}(k_x) = A_0 \int\limits_{-\infty}^{\infty} \exp(-x^2/2w^2) \exp(-ik_x x) dx = \sqrt{2\pi} w A_0 \exp(-k_x^2 w^2/2), \tag{2.16}$$

In the paraxial approximation, which often holds in optical waveguides, we may assume that $k_0 n_0 \gg k_x$, so that $\beta(k_x) \simeq k_0 n_0 [1 - (k_x^2/2k_0^2 n_0^2)]$, where n_0 is the index of the uniform waveguide. Equation 2.9 then becomes

$$\begin{aligned} A(z,x) &= \frac{wA_0\exp(ik_0n_0z)}{\sqrt{2\pi}}\int_{-\infty}^{\infty}\exp\left[-\frac{1}{2}\left(w^2+\frac{iz}{k_0n_0}\right)k_x^2+ik_xx\right]dk_x \\ &= \frac{wA_0\exp(ik_0n_0z)}{(w^2+iz/k_0n_0)^{1/2}}\exp\left[\frac{-x^2}{2(w^2+iz/k_0n_0)}\right]. \end{aligned} \tag{2.17}$$

We see that the field remains Gaussian-distributed, but the argument becomes complex, corresponding to the development of a curved phase front. The intensity per unit length $|A(z,x)|^2$ becomes

$$|A(z,x)|^2 = \frac{w^2A_0^2}{(w^4+z^2/k_0^2n_0^2)^{1/2}}\exp\left[\frac{-w^2x^2}{(w^4+z^2/k_0^2n_0^2)}\right]. \tag{2.18}$$

When $z \gg k_0n_0w^2 = 2\pi w^2n_0/\lambda$, where λ is the vacuum wavelength, we find that the on-axis intensity per unit length decreases as z^{-1} and the beam width spreads proportional to z.

As a special case of the Gaussian beam, we may consider the case $w = \lambda$, corresponding to a relatively narrow beam. In Fig. 2.3, we plot $P(k_x) = |\tilde{A}(k_x)|^2/\max[|\tilde{A}(k_x)|^2]$. As k_x increases $P(k_x)$ decreases, and when it falls to 0.01, we find that $\beta(k_x)/\beta(k_x = 0) = 0.94$, so that the propagation is nearly paraxial. We also show for reference the real part of the effective index $\mathrm{Re}(n_{\text{eff}})$ as a function of k_x. The effective index, $n_{\text{eff}} = \beta/k_0$, equals the ratio of the propagation constant to the wavenumber k_0. In Fig. 2.4, we show a movie of the beam as it propagates through the medium. We solve Eq. 2.9 after discretization with the Gaussian input beam profile, $A(z = 0, x) = \exp(-x^2/2w^2)$, setting $w = \lambda$. We then multiply $A(z,x)$ by $\exp(-i\omega t)$ and allow ωt to increase, where ω is the angular frequency of the input wave. We show the real part of the field in Fig. 2.4. We use a spatial transverse limit of $B = 500\lambda$,

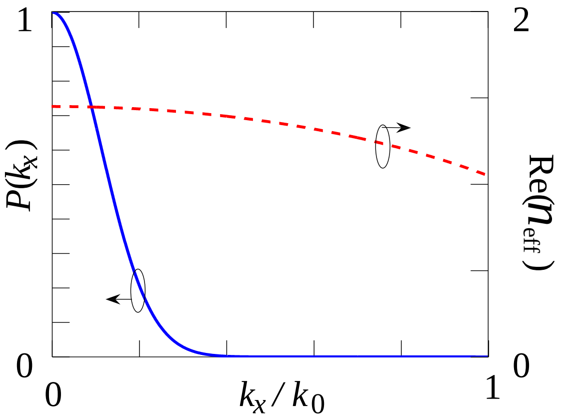

Figure 2.3: The normalized spectral power density $P(k_x) = |\tilde{A}(k_x)|^2 / \max[|\tilde{A}(k_x)|^2]$ and the real part of n_{eff} as a function of k_x.

and 1000 k_x-modes. As noted in Sec. 2.1, the k_x-modes are uniformly spaced in this cases. We set $n_0 = 1.45$, which is a typical value for silica waveguides.

The same qualitative features are present with almost any initial beam shape when z becomes large, as may be shown using the method of stationary phase [80]. We may rewrite Eq. 2.9 in the form:

$$A(z,x) = \frac{1}{2\pi} \int_{-\infty}^{\infty} \tilde{A}(k_x) \exp\left[ik_x x + i\beta(k_x)z\right] dk_x = \frac{1}{2\pi} \int_{-\infty}^{\infty} \tilde{A}(k_x) \exp(i\phi) dk_x. \quad (2.19)$$

Expanding $\phi = k_x x + \beta(k_x)z$ about the point $k_x = k_s$, we find $\phi = \phi^{(0)} + \phi^{(1)}(k_x - k_s) + (1/2)\phi^{(2)}(k_x - k_s)^2$ + higher order terms, where $\phi^{(0)} = k_s x + \beta(k_s)z$, $\phi^{(1)} = x + \beta'(k_s)z$, $\phi^{(2)} = \beta''(k_s)z$. We have written $\beta'(k_s) = d\beta/dk_x$ at $k_x = k_s$ and $\beta''(k_s) = d^2\beta/d^2k_x$ at $k_x = k_s$. From the expansion $\beta(k_x) = (k_0^2 n_0^2 - k_x^2)^{1/2}$, we find $\beta'(k_x) = -k_x/\beta(k_x)$. The stationary phase point satisfies the condition $0 = \phi^{(1)} = x - k_s z/\beta(k_s)$. It follows that $k_s = [x/(x^2 + z^2)^{1/2}]k_0 n_0$ and $\beta(k_s) = [z/(x^2 + z^2)^{1/2}]k_0 n_0$. Using this result, we find that $\phi^{(0)} = (1 + x^2/z^2)^{1/2} k_0 n_0 z$ and $\phi^{(2)} = -(1 + x^2/z^2)^{3/2}(z/k_0 n_0)$. Equation 2.19

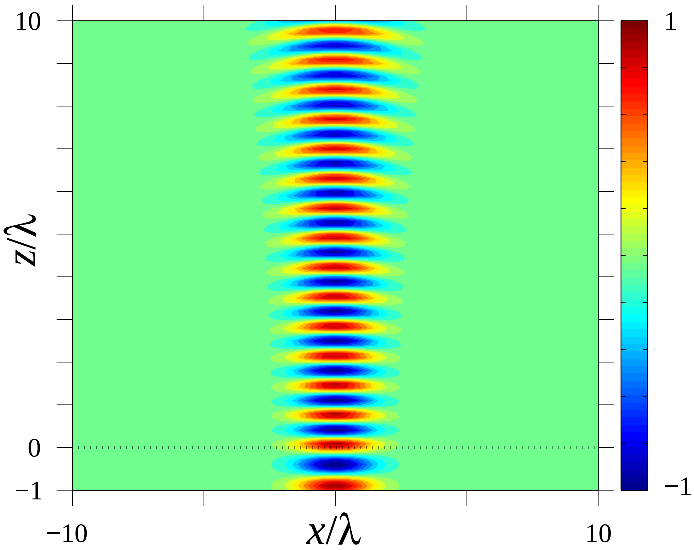

Figure 2.4: Wave propagation in a uniform medium. Light is injected into a uniform medium at $z = 0$. The movie shows the real part of the electric field.

now becomes

$$A(z,x) = \frac{1}{2\pi} \exp\left[i\left(1+\frac{x^2}{z^2}\right)^{1/2} k_0 n_0 z\right] \int_{-\infty}^{\infty} \tilde{A}(k_x) \exp\left[-\frac{i}{2}\left(1+\frac{x^2}{z^2}\right)^{3/2} \frac{z}{k_0 n_0}(k_x-k_s)^2\right] dk_x. \tag{2.20}$$

As z becomes larger, the oscillations about the stationary phase point $k_x = k_s$ become increasingly more rapid, so, to lowest order in an expansion in increasing powers of z, we may replace $\tilde{A}(k_x)$ with $\tilde{A}(k_s)$, and Eq. 2.20 becomes

$$\begin{aligned} A(z,x) &= \frac{1}{2\pi} \exp\left[i\left(1+\frac{x^2}{z^2}\right)^{1/2} k_0 n_0 z\right] \tilde{A}\left[\frac{x}{(x^2+z^2)^{1/2}} k_0 n_0\right] \\ &\quad \int_{-\infty}^{\infty} \exp\left[-\frac{i}{2}\left(1+\frac{x^2}{z^2}\right)^{3/2} \frac{z}{k_0 n_0}(k_x-k_s)^2\right] dk_x \\ &= \frac{1-i}{2\sqrt{\pi}}\left(1+\frac{x^2}{z^2}\right)^{-3/4}\left(\frac{k_0 n_0}{z}\right)^{1/2} \exp\left[i\left(1+\frac{x^2}{z^2}\right)^{1/2} k_0 n_0 z\right] \\ &\quad \tilde{A}\left[\frac{x}{(x^2+z^2)^{1/2}} k_0 n_0\right]. \end{aligned} \tag{2.21}$$

In the paraxial limit, which is of greatest practical interest, Eq. 2.21 reduces to

$$A(z,x) = \frac{1-i}{2\sqrt{\pi}} \left(\frac{k_0 n_0}{z} \right)^{1/2} \exp(ik_0 n_0 z) \tilde{A} \left(\frac{x}{z} k_0 n_0 \right), \tag{2.22}$$

and the intensity per unit length becomes

$$|A(z,x)|^2 = \frac{1}{2\pi} \frac{k_0 n_0}{z} \left| \tilde{A} \left(\frac{x}{z} k_0 n_0 \right) \right|^2 . \tag{2.23}$$

Hence, any initial condition ultimately resembles its initial Fourier transform, diminishes proportional to z^{-1} for any fixed ratio x/z and has a width that is proportional to z.

Equation 2.20 is the first term in an asymptotic expansion of $A(z,x)$ in powers of $z^{-1/2}$. Corrections will be small as long as $z \gg k_0 n_0 w^2$, where w is the initial beam width. This limit, referred to as the Fresnel limit, is rapidly reached in most applications. In the case of the Gaussian beam, this limit can be obtained directly from the complex solution that is shown in Eqs. 2.17 and 2.18. In Fig. 2.5, we show $I_{\text{norm}} = |A(z, x=0)|^2 / |A(z=0, x=0)|^2$, the on-axis normalized intensity per unit length, for both the complete and first-order asymptotic solutions in the case of the Gaussian beam. At the point $z/\lambda = 20$, the two solutions are nearly indistinguishable.

2.2.2 Three-layer waveguide

A simple waveguide that has guided modes as well as radiation modes is the three-layer symmetric waveguide, shown in Fig. 2.1(a). As long as $n_1 > n_0$, this waveguide has at least one guided mode [73]. We note that since the waveguide is symmetric, all modes must be even or odd, or must be the superposition of two degenerate mode in the case of radiation modes, where there is one even and one odd mode for each allowed value of β.

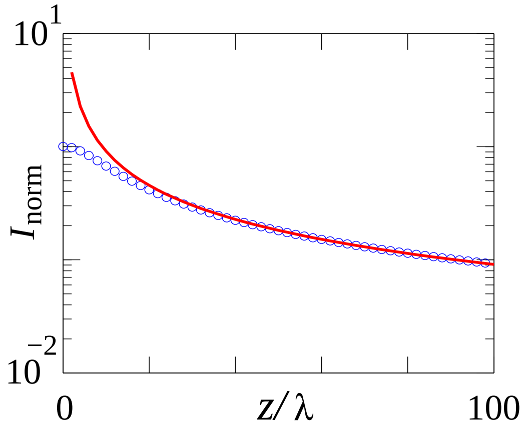

Figure 2.5: $I_{\text{norm}} = |A(z, x = 0)|^2/|A(z = 0, x = 0)|^2$ as a function z/λ for a Gaussian beam. Blue circles represent the complete solution, while the red solid curve represents the lowest-order asymptotic approximation.

From the wave equation, Eq. 2.3, we find that the even guided modes are expressible as

$$E(x) = \begin{cases} C_1 \cos(k_c x) & |x| \le a \\ C_0 \exp(-\alpha|x|) & a \le |x| \end{cases}, \tag{2.24}$$

where $\alpha = [\beta^2(\alpha) - k_0^2 n_0^2]^{1/2}$ and $k_c = (k_0^2 n_1^2 - \beta^2)^{1/2} = [k_0^2(n_1^2 - n_0^2) - \alpha^2]^{1/2}$. Consequently, the guided modes must satisfy the condition $k_c^2 < k_0^2(n_1^2 - n_0^2)$. Any mode that satisfies Eq. 3 and its derivative must be continuous at the slab interfaces, from which we infer

$$C_1 \cos(k_c a) = C_0 \exp(-\alpha a), \tag{2.25.a}$$

$$k_c C_1 \sin(k_c a) = \alpha C_0 \exp(-\alpha a), \tag{2.25.b}$$

which yields the dispersion relation

$$k_c \tan(k_c a) = \alpha = [(k_0^2(n_1^2 - n_0^2) - k_c^2]^{1/2}. \tag{2.26}$$

This transcendental relation always has at least one solution and will have at least two if $k_0a(n_1^2 - n_0^2)^{1/2} > \pi$. The orthonormality condition Eq. 2.5 becomes [73]

$$1 = \int_{-\infty}^{\infty} E^2(x)dx = C_1^2 \left[a + \frac{\sin(2k_ca)}{2k_c} + \frac{\cos^2(k_ca)}{\alpha} \right]. \tag{2.27}$$

The discussion for the odd guided modes is similar. When $x > 0$, we find

$$E(x) = \begin{cases} C_1 \sin(k_cx) & 0 \leq x \leq a \\ C_0 \exp(-\alpha x) & a \leq x \end{cases}, \tag{2.28}$$

and $E(x) = -E(-x)$, when $x < 0$. The dispersion relation becomes

$$-k_c \cot(k_ca) = \alpha = [k_0^2(n_1^2 - n_0^2) - k_c^2]^{1/2}, \tag{2.29}$$

which will have at least one solution as long as $k_0a(n_1^2 - n_0^2)^{1/2} > \pi/2$. Conversely, there is only one even guided mode when $k_0a(n_1^2 - n_0^2)^{1/2} < \pi/2$. Quite generally, it follows from Sturm-Liouville theory that the propagation numbers for the even and odd modes are interleaved and are non-degenerate [77].

When $x > 0$, the even radiation mode may be written

$$E_e(k_x, x) = \begin{cases} C_{1e} \cos(k_cx) & 0 \leq x \leq a \\ C_{0e} \cos(k_xx + \phi_e) & a \leq x \end{cases}, \tag{2.30}$$

and odd radiation mode solutions may be written

$$E_o(k_x, x) = \begin{cases} C_{1o} \sin(k_cx) & 0 \leq x \leq a \\ C_{0o} \sin(k_xx + \phi_o) & a \leq x \end{cases}, \tag{2.31}$$

with $E_e(k_x, x) = E_e(k_x, -x)$ and $E_o(k_x, x) = -E_o(k_x, -x)$ when $x < 0$. Any value of k_x is allowed, and we find $\beta(k_x) = (k_0^2n_0^2 - k_x^2)^{1/2}$ and $k_c(k_x) = [k_0^2(n_1^2 - n_0^2) + k_x^2]^{1/2}$. Taking the combination $E(k_x, x) = E_e(k_x, x) + iE_o(k_x, x)$ at each value of k_x, we may write

$$E(k_x, x) = \begin{cases} C_1 \exp(ik_cx) & 0 \leq x \leq a \\ C_0 \exp(ik_xx) + D_0 \exp(-ik_xx) & a \leq x \end{cases}, \tag{2.32}$$

where $C_1 = C_{1e} = C_{1o}$, $C_0 = [C_{0e}\exp(i\phi_e) + C_{0o}\exp(i\phi_o)]/2$, and $D_0 = [D_{0e}\exp(-i\phi_e) - C_{0o}\exp(-i\phi_o)]/2$ when $x > 0$ and $E(k_x, x) = E^*(k_x, -x)$ when $x < 0$. From the continuity of $E(k_x, x)$ and its derivative at $x = a$, we find

$$C_1 \exp(ik_c a) = C_0 \exp(ik_x a) + D_0 \exp(-ik_x a), \tag{2.33.a}$$

$$ik_c C_1 \exp(ik_c a) = ik_x C_0 \exp(ik_x a) - ik_x D_0 \exp(-ik_x a), \tag{2.33.b}$$

which determines the ratios D_0/C_1 and C_0/C_1. From the orthogonality condition, Eq. 2.5, we find $|C_0|^2 + |D_0|^2 = 1$. The solution given in Eq. 2.32 is like the solutions $E(k_x, x) = \exp(ik_x x)$ that we found in the case of the uniform medium. However, there is one important difference. when $k_x > 0$, the solution in the uniform medium propagates rightward, which means that it is purely outgoing as $x \to +\infty$ and is purely incoming as $x \to -\infty$. The opposite holds, when $k_x < 0$. By contrast, the solution in Eq. 2.32 has both incoming and outgoing components as $x \to \pm\infty$.

We now consider as an example a medium in which $n_1 = 1.45$ and $n_0 = 0.96 n_1 = 1.39$. The width in the center region is chosen so that $k_0 a (h_1^2 - n_0^2)^{1/2} = 1$, which implies $a = 0.39\lambda$. There is only one guided mode [73], and we consider a Gaussian input beam $A(z = 0, x) = A_0 \exp(-x^2/2a^2)$, where a is half the width of the central layer, as shown in Fig. 2.1. In this example, 70% of the initial power is in the guided mode, and the rest is in the radiation modes. We discretize the radiation contribution to Eq. 2.4 using Neumann boundary conditions, as discussed in Sec. 2.1. For even modes, we insert the ratios D_0/C_1 and C_0/C_1 that we obtained from Eq. 2.33 into Eq. 2.32. We set $dE/dx = 0$ at $x = \pm B$, and we then obtain

$$\tan[k_x(B - a)] + \frac{k_c}{k_x}\tan(k_c a) = 0. \tag{2.34}$$

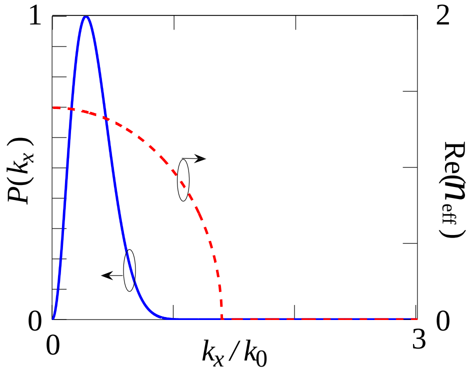

Figure 2.6: The normalized spectral power density $P(k_x) = |\tilde{A}(k_x)|^2/\max[|\tilde{A}(k_x)|^2]$ and the $\mathrm{Re}(n_{\mathrm{eff}})$ as a function of k_x.

We note for completeness that the corresponding dispersion relation for the odd modes is

$$\tan[k_x(B-a)] - \frac{k_c}{k_x}\cot(k_c a) = 0, \tag{2.35}$$

although we will not need the odd modes in this example since the initial condition is symmetric. We keep 2,000 k_x-modes, and we set $B = 500a$. The function $\tilde{A}(k_x) = \tilde{A}_e(k_x)$ is purely real in this case, and we show $|\tilde{A}(k_x)|^2$ normalized to its maximum for $k_x > 0$ in Fig. 2.6. We also show for reference the real part of the effective index $\mathrm{Re}(n_{\mathrm{eff}})$ as a function of k_x. Note that n_{eff} is a purely real number when $k_x < n_0 k_0$, and n_{eff} becomes a purely imaginary number when $k_x > n_0 k_0$. As in the case of the uniform guide, the radiation components for which $k_x > n_0 k_0$ do not propagate. They are exponentionally damped, and their energy will be reflected back.

In Fig. 2.7, we show a movie of the wave propagation in the z-direction. The waveguide parameters are the same as in Fig. 2.6. We keep 2,000 k_x-modes, and we set $B = 1,000a$. As expected, the Gaussian input profile separates into a guided-wave component that propagates without diminishing and a diffractive component that diminishes algebraically, not exponentially. The behavior of the diffractive component

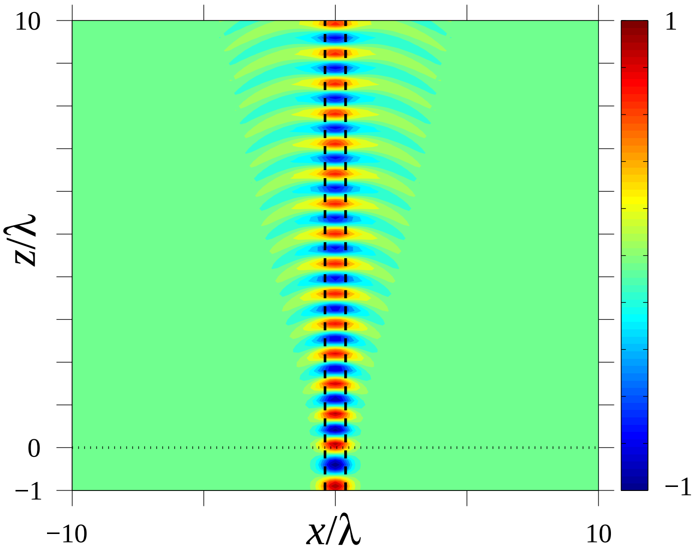

Figure 2.7: Wave propagation in a three-layer waveguide. The light is injected into the waveguide at $z = 0$. The movie shows the real part of the electric field. The black dashed lines indicate $x = \pm a$.

in the three-layer waveguide is qualitatively similar to the behavior of a beam in the uniform medium.

We find, as in the case of the uniform medium that the solution spreads proportional to z and that the intensity per unit length diminishes proportional to z^{-1}. We may now once again use the method of stationary phase to obtain the contribution of the radiation modes in the Fresnel limit when $z \gg k_0 n_0 w^2$ for the three-layer waveguide. Focusing on the radiation field contribution A_{rad} to the total field, we rewrite this field at z in the form

$$A_{\text{rad}}(z,x) = \frac{1}{2\pi}\int_{-\infty}^{\infty} \tilde{A}(k_x)E(k_x,x)\exp\left[i\beta(k_x)z\right]dk_x = \frac{1}{2\pi}\int_{-\infty}^{\infty} \tilde{A}(k_x)E(k_x,x)\exp(i\phi)dk_x. \tag{2.36}$$

There is no analytical solution of this equation. Hence, for $x = 0$, we proceed by writing

$$A_{\text{rad}}(z, x = 0) = \frac{1}{2\pi} \int\limits_{-\infty}^{\infty} \tilde{A}(k_x) E(k_x, 0) \exp(i\phi) dk_x. \tag{2.37}$$

Expanding $\phi = \beta(k_x)z$ about the point $k_x = k_s$, we find $\phi = \phi^{(0)} + \phi^{(1)}(k_x - k_s) + (1/2)\phi^{(2)}(k_x - k_s)^2$ + higher order terms, where $\phi^{(0)} = \beta(k_s)z$, $\phi^{(1)} = \beta'(k_s)z$, $\phi^{(2)} = \beta''(k_s)z$, the stationary phase point satisfies the condition $0 = \phi^{(1)} = -k_s z/\beta(k_s)$. It follows that $k_s = 0$ and $\beta(k_s) = k_0 n_0$. Using this result, we find that $\phi^{(0)} = k_0 n_0 z$ and $\phi^{(2)} = -(z/k_0 n_0)$. We also write $\tilde{A}(k_x)$ and $E(k_x, 0)$ as a Taylor series, from which we obtain $\tilde{A}(k_x) = \tilde{A}(k_s) + \tilde{A}'(k_x)(k_x - k_s)$ + higher order terms and $E(k_x, 0) = E(k_s, 0) + E'(k_s, 0)(k_x - k_s)$ + higher order terms. Both $\tilde{A}(k_x)$ and $E(k_x, 0)$ are zero at $k_x = 0$. Equation 2.37 now becomes

$$\begin{aligned} A_{\text{rad}}(z, x = 0) &= \frac{1}{2\pi} \exp\left[ik_0 n_0 z\right] \int\limits_{-\infty}^{\infty} \tilde{A}'(0) E'(0, 0) k_x^2 \exp\left[-\frac{i}{2} \frac{z}{k_0 n_0} k_x^2\right] dk_x \\ &= \frac{1 + i}{2\sqrt{\pi}} \exp(ik_0 n_0 z) \tilde{A}'(0) E'(0, 0) \left(\frac{k_0 n_0}{z}\right)^{3/2}. \end{aligned} \tag{2.38}$$

The power then becomes

$$|A_{\text{rad}}(z, x = 0)|^2 = \frac{1}{2\pi} \left(\frac{k_0 n_0}{z}\right)^3 \left|\tilde{A}'(0) E'(0, 0)\right|^2. \tag{2.39}$$

Hence, the power at $x = 0$ diminishes proportional to z^{-3}. At other values of x/z, the power at $\tilde{A}(k_s) \neq 0$, and the power will diminish proportional to z^{-1} at large z, just as is the case in the uniform medium.

In Fig. 2.8, we show $I_{\text{norm}} = |A(z, x = 0)|^2 / |A(z = 0, x = 0)|^2$ as a function of z/λ. The blue circles represent the power calculated by solving the propagation equation, Eq. 2.4 using the complete decomposition. The red dashed curve represents the sum

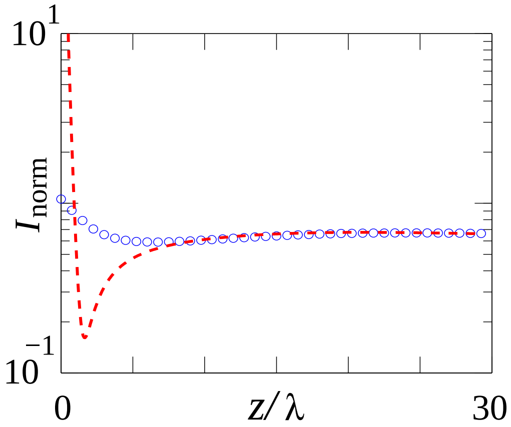

Figure 2.8: $I_{\mathrm{norm}} = |A(z, x = 0)|^2/|A(z = 0, x = 0)|^2$ as a function of z/λ for a Gaussian beam. The blue circles represent the power calculated by solving the propagation equation, Eq. 2.4 using the complete decomposition, while the red dashed curve represents the sum of the asymptotic approximation from Eq. 2.39 and the guided mode contribution.

of the fundamental mode propagation and the steepest descent estimated according to Eq. 2.39. The numerical integration and asymptotic analysis agree at $z > 10\lambda$.

The steepest descent approach that we have used to evaluate the radiation integrals is a powerful mathematical technique that will allow us in the following sections to separate the leaky mode contributions to the radiation integrals from the diffractive contributions.

2.3 W-type slab waveguide

We now turn to consideration of what is perhaps the simplest waveguide that has leaky modes — the W-type waveguide whose profile is shown in Fig. 2.1(b). A solution to Eq. 2.3 is purely outgoing when $x > b$ as $x \rightarrow +\infty$ if $E(x) \propto \exp(ik_x^+ x)$ where $\mathrm{Re}(k_x^+) > 0$ and is purely incoming if $\mathrm{Re}(k_x^+) < 0$. A solution to Eq. 2.3 is purely outgoing when $x < -b$ as $x \rightarrow -\infty$ if $E(x) \propto \exp(ik_x^- x)$ where $\mathrm{Re}(k_x^-) < 0$. A leaky mode is defined as a solution to Eq. 2.3 that has no incoming components as $x \rightarrow \pm\infty$ and has an outgoing component either as $x \rightarrow +\infty$ or $x \rightarrow -\infty$ or both. In an asymmetric guide, it is possible for a leaky mode to be guided on one side and outgoing on the other, but in a symmetric guide, like that shown in Fig. 2.1(b), it must be purely outgoing as $x \rightarrow \pm\infty$. Just as a waveguide may not have guided mode solutions, it may not have leaky mode solutions. For example, the uniform waveguide that we considered in Sec. 2.2.1 only has solutions that are incoming as $x \rightarrow -\infty$ if they are outgoing as $x \rightarrow +\infty$ and vice versa since $E(k_x, x) = \exp(ik_x x)$. When leaky mode solutions exist, their growth rate as $x \rightarrow \pm\infty$ must be small in order for them to be of practical interest.

2.3.1 Leaky mode analysis

We focus on the index profiles, shown in Fig. 2.1(b) for which $n(x) = n_0$ for $|x| \leq a$, $n(x) = n_1$ $a \leq |x| \leq b$, and $n(x) = n_0$ for $b < |x|$. We will search for a solution that when $x > 0$ that may be written

$$E(x) = \begin{cases} C\cos k_x x & 0 \le x \le a \\ \dfrac{C\cos(k_x a)}{\cosh(\alpha a + \phi)}\cosh(\alpha x + \phi) & a \le x \le b \\ \dfrac{C\cos(k_x a)\cosh(\alpha b + \phi)}{\cosh(\alpha a + \phi)}\exp[ik_x(x - b)] & b \le x \end{cases}, \tag{2.40}$$

where $k_x = (k_0^2 n_0^2 - \beta^2)^{1/2}$ and $\alpha = (\beta^2 - k_0^2 n_1^2)^{1/2}$. When $x < 0$, we set $E(-x) = E(x)$, so that the solution is even. We also demand $\mathrm{Re}(k_x) > 0$, so that the solution is outgoing as $x \rightarrow \pm\infty$. By matching the x-derivatives of the fields at $x = a$ and b, we obtain

$$k_x \tan(k_x a) = -\alpha \tanh(\alpha a + \phi), \tag{2.41.a}$$

$$\alpha \tanh(\alpha b + \phi) = ik_x. \tag{2.41.b}$$

Eliminating the constant ϕ, we obtain the dispersion relation for the W-type waveguide [81],

$$\tan(k_x a) = \frac{\alpha}{k_x}\tanh\left[\tanh^{-1}\left(-i\frac{k_x}{\alpha}\right) + \alpha(b - a)\right]. \tag{2.42}$$

We now consider a specific numerical example that is closely related to the three-layer waveguide that we considered in Sec. 2.2.1. In this example, we set $n_0 = 1.45$ and $n_1 = 0.96n_0 = 1.39$, which is the same ratio as in the three-layer waveguide, except that the roles of n_0 and n_1 are interchanged, because it is now the higher-index material that is present when $x \rightarrow \infty$. The width in the center region is chosen so that $k_0 a(n_0^2 - n_1^2)^{1/2} = 1$ and $b/a = 5$, so that $a = 0.39\lambda$ and $b = 1.96\lambda$. With these choices, the waveguide is the same up to $|x| \le b$ as in the case of the three-layer waveguide. In Fig. 2.9, we show a logarithmic plot of the absolute value of e, the difference between the left and right sides of Eq. 2.42, as a function of real and imaginary part of n_{eff}.

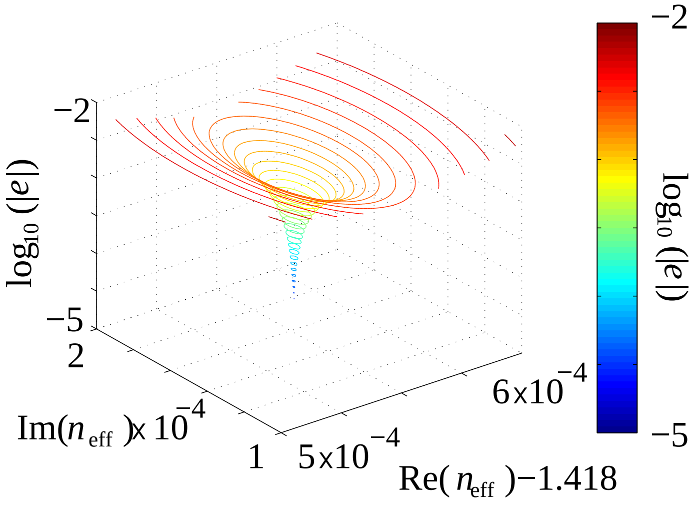

Figure 2.9: Logarithm of the magnitude of the difference between the left and right hand side of Eq. 2.42.

There is evidently a pole in the plot, corresponding to a resonance of Eq. 2.42. To find its location accurately, we first find the derivative along the real axis and then determine its derivative in the imaginary direction using the Cauchy-Riemann relation for e [82]. We then use the Newton-Raphson method to find the point where $e \longrightarrow 0$. In the case considered here, we obtain $n_{\text{eff}} = \beta/k_0 = 1.4185997 + 1.577 \times 10^{-4} i$. We have written the answer to eight significant figures, because the imaginary part is four orders of magnitude smaller than the real part. It is typical in practical problems for the imaginary part of β to be much smaller than the real part. However, obtaining this level of accuracy is not a problem in a modern-day 32-bit computer that has approximately 15 digits of accuracy for a double precision number.

2.3.2 Perturbation analysis

We now analyze this same problem using perturbation theory. From a practical standpoint, it becomes increasingly difficult to obtain the imaginary part of β accurately as b/a increases, since the imaginary part of β rapidly decreases, and when close to 15 digits of accuracy are needed, one will typically have large computational round-off errors. At the same time, this limit is precisely the one in which perturbation theory is expected to work well and can substantially decrease the computational time required to find $\mathrm{Im}(\beta)$ [57]. From a conceptual standpoint, the leaky modes in a W-type waveguide, shown in Fig. 2.1(b), are expected to be a slight modification of the corresponding guided modes in the corresponding three-layer waveguide, shown in Fig. 2.1(a). Perturbation theory allows us to make this connection directly. We begin by writing $\beta \simeq \beta_0 + \Delta\beta$, where β_0 is the propagation constant for the three-layer waveguide. We then have

$$k_x = [(k_0 n_1)^2 - (\beta_0 + \Delta\beta)^2]^{1/2} \approx k_{x0} - \beta_0 \Delta\beta / k_{x0}, \tag{2.43.a}$$

$$\alpha = [(\beta_0 + \Delta\beta)^2 - (k_0 n_0)^2]^{1/2} \approx \alpha_0 + \beta_0 \Delta\beta / \alpha_0, \tag{2.43.b}$$

where k_{x0} and α_0 are the solution for the corresponding three-layer waveguide. We may now substitute these expressions into the dispersion relation, Eq. 2.42, and carry out a Taylor expansion in powers of $\Delta\beta$, keeping only the zero-order and first-order term. Solving for $\Delta\beta$, we obtain

$$\Delta\beta = \frac{2\exp[-2\alpha_0(b-a)][ik_{x0}^2 \tan(k_{x0}a) + \alpha_0^2]}{\beta_0 M_W}, \tag{2.44}$$

where

$$\begin{aligned} M_W \;=\; & 2 + (\alpha_0/k_{x0} - k_{x0}/\alpha_0)[i + \tan(k_{x0}a)] + a(\alpha_0 - ik_{x0})[1 + \tan^2(k_{x0}a)] - 2i\tan(k_{x0}a) \\ & + \{4\alpha_0(b-a) - 4 + 2iak_{x0}[1 + \tan^2(k_{x0}a)] + 4i\tan(k_{x0}a) \\ & + 4i\tan(k_{x0}a)(b-a)k_{x0}/\alpha_0\}\exp[-2\alpha_0(b-a)]. \end{aligned} \tag{2.45}$$

We now find that $n_{\text{eff}} = \beta/k_0 = 1.4185997 + 1.567 \times 10^{-4}i$, and we see that the direct computation of $\text{Im}(\beta)$ and the result from perturbation theory agree to three decimal place.

2.3.3 Physical explanation of the exponential decay

The exponential decay in z implies that there is an exponential growth in $|x|$. Mathematically, Eqs. 2.43 and 2.44 implies that a positive imaginary component change in β, corresponding to decay in z, implies a negative imaginary change in k_x and growth in $|x|$. From a physical standpoint, we may understand this growth as a consequence of flux conservation.

The Helmholtz equation, Eq. 2.1, has a conserved time-averaged flux that may be written

$$\mathbf{F}(z,x) = (1/2i\omega)[A^*(z,x) \bigtriangledown A(z,x) - A(z,x) \bigtriangledown A^*(z,x)], \tag{2.46}$$

where $\bigtriangledown(\cdot) = \hat{z}\partial/\partial z + \hat{x}\partial/\partial x$ is the transverse gradient operator. Using Eq. 2.1, we find that $\bigtriangledown \cdot \mathbf{F} = 0$. When $A(z,x)$ corresponds to a TE wave, then $\mathbf{F}$ is proportional to the Poynting flux. If $A(z,x) = E(x)\exp(i\beta z)$ is a waveguide mode, then F_z, the z-component of $\mathbf{F}$, becomes $F_z = [\text{Re}(\beta)/\omega]|A(x)|^2$, which is positive definite. Referring to Fig. 2.10, flux conservation implies that the inward flux must equal the outward when integrated over the sides of the rectangles defined by the z-values z_1 and z_2 and by any two values of x, for example $x = \pm A$ or $x = \pm B$. When $x = \pm A$, the difference between the flux entering at $z = z_1$ and leaving at $z = z_2$ is proportional to $[1 - \exp(-2\text{Im}(\beta)|z_1 - z_2|)] \int_{-A}^{A} |E(x)|^2 dx$, and when $x = \pm B$, the difference is proportional to $[1 - \exp(-2\text{Im}(\beta)|z_1 - z_2|)] \int_{-B}^{B} |E(x)|^2 dx$. Since the second integral is larger than the first, the flux that exits from the sides at $|x| = \pm B$ must be larger

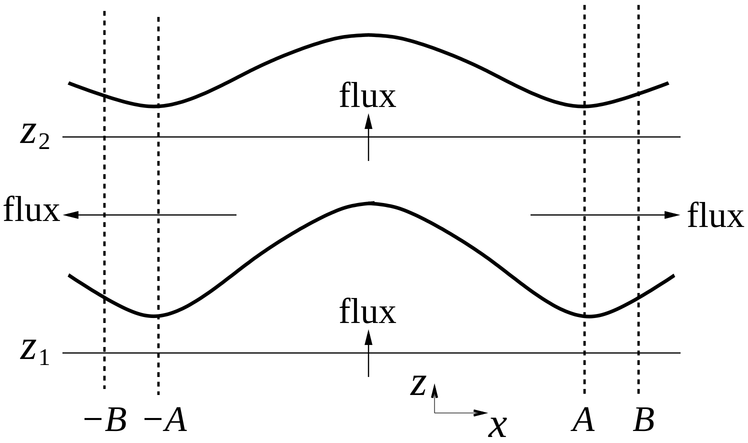

Figure 2.10: Schematic illustration of the flux flow.

than the flux that exits from the sides at $|x| = \pm A$, as long as the waves that exit from the sides are purely outgoing, as is the case for the leaky mode at sufficiently large $|x|$. This increase is only possible if $|E(x)|$ increases as well.

2.3.4 Radiation mode decomposition

There are no guided modes in the W-type waveguide. As a consequence, it must be possible to express any square-integrable initial condition as a superposition of radiation modes, just as in the case of the uniform waveguide. At the same time when $b \gg a$, we expect the behavior to resemble the behavior in the three-layer waveguide and in particular when the initial profile is close to the guided mode, as was the case with the Gaussian profile that we showed in Sec. 2.2.2, we expect the evolution to closely resemble that of the leaky mode in the central waveguide region. In this chapter, we will show how a superposition of the radiation modes leads to leaky behavior in a W-type waveguide.

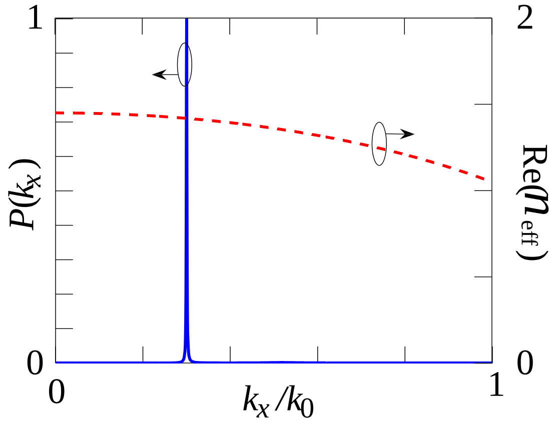

Figure 2.11: The normalized spectral power density $P(k_x) = |\tilde{A}(k_x)|^2/\max[|\tilde{A}(k_x)|^2]$ and the real part of effective index $\mathrm{Re}(n_{\mathrm{eff}})$ as a function of k_x/k_0.

When $x > 0$, the radiation modes may be written as [83]

$$E(x) = \begin{cases} C_2 \exp(ik_x x) & 0 \le x \le a \\ C_1 \exp(-\alpha x) + D_1 \exp(\alpha x) & a \le x \le b \\ C_0 \exp(-ik_x x) + D_0 \exp(ik_x x) & b \le x \end{cases}, \tag{2.47}$$

where $\beta(k_x) = (k_0^2 n_0^2 - k_x^2)^{1/2}$ and $\alpha(k_x) = [k_0^2(n_0^2 - n_1^2) - k_x^2]^{1/2}$. When $x < 0$, we find $E(k_x, x) = E^*(k_x, -x)$, and k_x can have any real value. Note that in contrast to the leaky mode *ansatz* in Eq. 2.40, the radiation modes include both incoming and outgoing waves. Equation 2.47 has both incoming and outgoing components at $|x| > b$, in contrast to Eq. 2.47, which only has outgoing component at $|x| > b$. We may find the dispersion relation by matching $E(k_x, x)$ and its derivatives at $x = a$ and $x = b$, and the orthonormality condition becomes $|C_0|^2 + |D_0|^2 = 1$. The dispersion relation in this case is complicated, and we do not show it here.

In Fig. 2.11, we show the normalized coefficient $P(k_x) = |\tilde{A}(k_x)|^2/\max(|\tilde{A}(k_x)|^2)$ and $\mathrm{Re}(n_{\mathrm{eff}})$ for the same Gaussian input beam that we considered in Sec. 2.2.2 in which $A(z = 0, x) = \exp(-x^2/2a^2)$, where a is half of the center layer width, as shown in Fig. 2.1. We calculated $\tilde{A}(k_x)$ computationally, starting from the expression

$$\tilde{A}(k_x) = \int_{-\infty}^{\infty} A(z=0,x)E^*(k_x,x)dx. \tag{2.48}$$

using the decomposition procedure described in Sec. 2.1 with 2,000 k_x-modes and with $B = 2,000a$. We find that $P(k_x)$ is sharply peaked around a value of k_x that we denote k_r. This resonant behavior of $\tilde{A}(k_x)$ differs sharply from that of the uniform waveguide or the analogous three-layer waveguide, in which $\tilde{A}(k_x)$ varied smoothly. There is a smoothly-varying portion of $\tilde{A}(k_x)$, in which $k_x^2 > k_0^2(n_0^2 - n_1^2)$, that corresponds to a diffractive contribution, analogous to the diffractive contribution in the three-layer waveguide. However, we find that as a result of the resonant behavior of $\tilde{A}(k_x)$, the integral will become dominated at an early stage of evolution by the behavior near $k_x = k_r$, rather than the stationary phase points of $\beta(k_x)$. There will also be a Lorentzian peak when $k_x = -k_r$, in addition to the Lorentzian peak at $k_x = k_r$. A close examination of $\tilde{A}(k_x)E(k_x, x = 0)$ shows that the Lorentzian peaks that dominate its behavior have a Lorentzian (single-pole) shape, so that we may write to good approximation

$$\tilde{A}(k_x)E(k_x,x=0) = -\frac{ik_i\tilde{A}(k_r)E(k_r,x=0)}{k_x - k_r - ik_i} + \frac{ik_i\tilde{A}(-k_r)E(-k_r,x=0)}{k_x + k_r + ik_i}. \tag{2.49}$$

Lorentzian peaks like the ones in Eq. 2.49 *always appear* when leaky modes are present! These Lorentzian peaks and the corresponding poles in the complex k_x-domain are the signature of a leaky mode. Just as $-i/(k_x - k_r - ik_i) + i/(k_x + k_r + ik_i)$ is the Fourier transform in the ordinary sense of $\exp[(ik_r - k_i)|x|]$ when $k_i > 0$, it is also the transform of this function in a generalized-function or distribution sense when $k_i < 0$ [84]. Hence, we find that k_r corresponds to the oscillation wavenumber of the leaky mode when $|x| > b$ and is nearly equal to k_c in the corresponding waveguide, while $|k_i|$ corresponds to the leaky mode's transverse exponentiation factor when $|x| > b$. From Eq. 2.49, it also follows that $|k_i|$ corresponds to the width of the Lorentzian peaks in the k_x-domain. When $b - a$ increases, we find that $|k_i|$ rapidly decreases, and the Lorentzian peaks tend toward δ-functions, while k_r becomes exactly equal to k_c. In general, it must be the case that $|k_i| \ll k_r$ in order for a leaky mode to propagate for an observable distance. That is the case in the example discussed here, and we thus find the following equation by using the residue theorem [82]

$$\begin{aligned} A(z, x = 0) &= \frac{1}{2\pi} \int_{-\infty}^{\infty} \tilde{A}(k_x) E(k_x, x = 0) \exp[i\beta(k_x)z] dk_x \\ &\simeq \frac{1}{2} k_i \tilde{A}(k_r) E(k_r, x = 0) \exp[i\beta_r z - \beta_i z] + \text{c.c.}, \end{aligned} \tag{2.50}$$

where $\beta_r = \text{Re}[\beta(k_x = k_r + ik_i)] \simeq \beta(k_r)$ and $\beta_i = \text{Im}[\beta(k_x = k_r + ik_i)] \simeq -k_r k_i / \sqrt{k_0^2 n_0^2 - k_r^2} = k_i \partial\beta/\partial k_x|_{k_x = k_r}$. We find $\text{Re}(n_{\text{eff}}) = \text{Re}(\beta_r/k_0) = 1.4185984$ and $\text{Im}(n_{\text{eff}}) = \text{Im}(\beta_i/k_0) = 1.588 \times 10^{-4}$, which are close to the values that we found from the leaky mode analysis. Equation 2.50 shows the intuitively expected result that $A(z, x = 0)$ is approximately proportional to $\tilde{A}(k_r)$, which is the overlap integral of $A(z = 0, x)$ with the mode at $k_x = k_r$ that corresponds closely to the guided mode in the three-layer waveguide. We find that $\tilde{A}(k_x)$ and $E(k_x, x = 0)$ have the same shape around $k_x = k_r$. Both are sharply peaked. Finally, $A(z, x = 0)$ has an exponential decay rate in z that is inversely proportional to the width of the resonance in $\tilde{A}(k_x)$. In Fig. 2.12, we show a movie of the evolution of a Gaussian input beam in a W-type waveguide with $A(z = 0, x) = \exp(-x^2/2a^2)$, just as in the three-layer waveguide simulation in Fig. 7. The waveguide parameters are the same that we used in Fig. 2.9, *i.e.*, $n_0 = 1.45$, $n_1 = 0.96 n_0$, $k_0 a (n_0^2 - n_1^2)^{1/2} = 1$, and $b/a = 5$. We keep

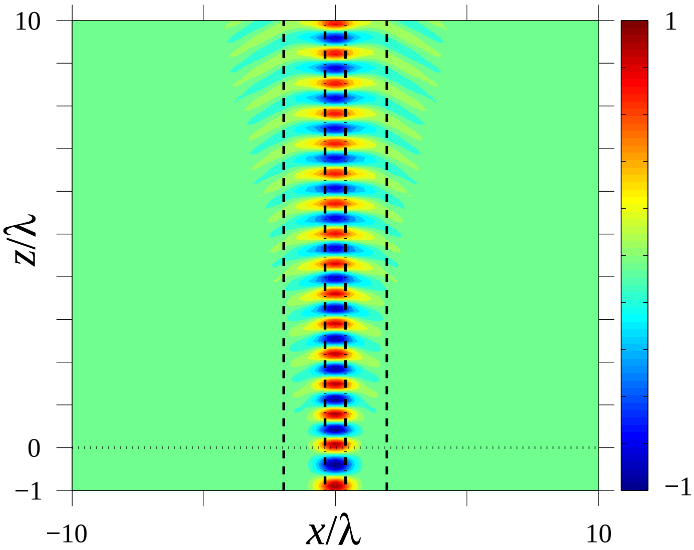

Figure 2.12: Wave propagation in a W-type waveguide. Light is injected into the W-type waveguide at $z = 0$. The black dash-dotted lines and black dashed lines indicate $x = \pm a$ and $x = \pm b$, respectively. The movie shows the real part of the electric field.

1,000 k_x-modes, and we set $B = 2,000a$. After an initial transient in which a portion of the initial beam rapidly diffracts, the beam settles down into the shape of the leaky mode in the central region of waveguide $|x| < b$, after which the gradual exponential loss is visible.

This discussion assumes that the change in $\beta(k_x)z$ is much less than one over the Lorentzian linewidth. This assumption will eventually break down as z increases, and the beam evolution will no longer be exponential. We will discuss this point shortly.

2.3.5 Comparison and analysis

Figure 2.13 shows $\text{Im}(n_{\text{eff}})$ as a function of b/a. As the ratio b/a increases, all the methods that we have used for calculating β_i — the direct determination of the leaky mode solution, the perturbation method, and the determination from the radiation mode solutions — yield nearly identical results. The linear falloff on a logarithmic

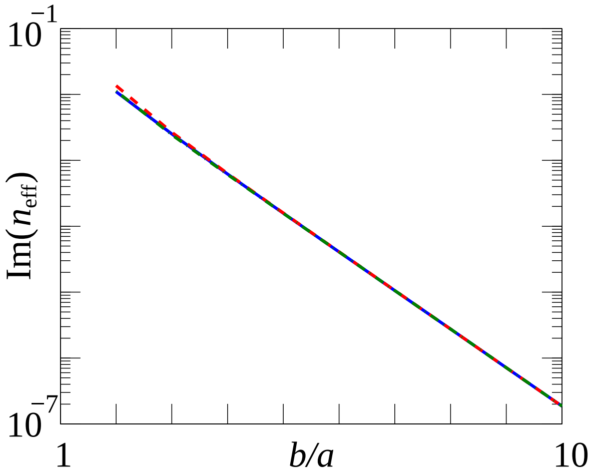

Figure 2.13: $\mathrm{Im}(n_{\mathrm{eff}})$ as a function of b/a. The blue solid curve, green dash-dotted curve, and red dashed curve represent the leakage loss calculated from the direct determination of the leaky mode solution, the perturbation method, and the determination from the radiation mode solution, respectively.

plot indicates that imaginary part of n_{eff} decreases exponentially as b/a increases. This falloff is expected since the magnitude of the nearly guided mode decreases exponentially before reaching the interfaces at $x = \pm b$.

Figure 2.14 shows a movie of the transverse mode for the Gaussian input beam that we considered in Fig. 2.7 as it propagates along the W-type waveguide. We keep 5,000 k_x-modes, and we set $B = 8,000a$. The waveguide parameters are the same as in Figs. 2.9 and 2.12. The red dashed curve indicates the leaky mode solution. The mode profiles are normalized to 1 at $x = 0$, so that the attenuation as z increases is not visible. The two solutions overlap in the center, showing that the mode preserves its shape. The exponential increase as $x \to \pm\infty$ that is expected for a leaky mode is also apparent in both solutions. However, the dynamical solution has the following characteristics: First, a portion of the the beam that is mismatched to the leaky mode in the central region of the waveguide rapidly diffracts. Second, as the beam

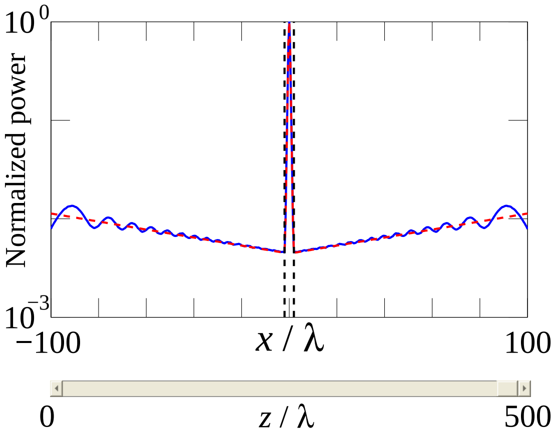

Figure 2.14: Movie of the transverse mode evolution as the mode propagates along a W-type slab waveguide. The red dashed curve and blue solid curve represent the transverse mode power from the leaky mode and the actual profile that is found by integrating Eq. 2.4. The black dashed lines indicate $x = \pm b$.

propagates along the z-direction, the beam's power gradually increases in the cladding region of the waveguide, $|x| > b$, and resembles the leaky mode profile over larger values of $|x|$. Hence, the power that is radiated from the core is actually not lost since it is simply redistributed from the core into the cladding region. Third, the dynamic solution has a front in $\pm x$ beyond which it rapidly tends to zero. The oscillations in Fig. 2.14 are due to phase interference from different points along the initial x-profile, analogous to the oscillations that are observed in Fraunhoffer diffraction from a single slit.

We noted earlier that as z becomes large, we expect the exponential decay to cease. Mathematically, this effect will occur when the change in $\beta(k_x)z$ over the bandwidth of the Lorentzian peak becomes large. The stationary phase point of $\beta(k_x)$ will once again dominate the solution, and the wave should exhibit algebraic decay that is consistent with diffraction, rather than the exponential decay that is characteristic of leakage. This long-term diffraction should not be confused with the early-term

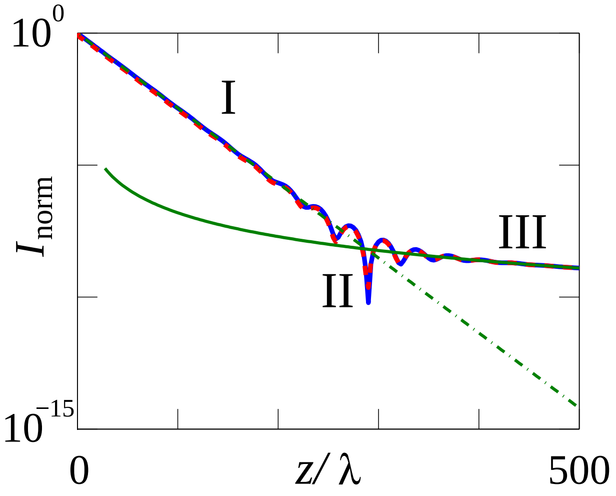

Figure 2.15: $I_{\text{norm}} = |A(z, x = 0)|^2/|A(z = 0, x = 0)|^2$ as a function of z/λ for a Gaussian beam with $b/a = 2.5$. The red dashed curve shows the power of the field using numerical integration. The green dash-dotted and green solid curves show respectively the steepest descent analysis for the evolution at $x = 0$ and the leaky mode evolution. The blue solid curve shows the I_{norm} that is calculated by summing the fields from the steepest descent analysis that were used to produce I and II.

diffraction that is observed immediately after a beam is launched into the waveguide. In contrast to the early-term diffraction that is due to the portions of the spectrum $\tilde{A}(k_x)$ in which $k_x^2 > k_0^2(n_0^2 - n_1^2)$, the long-term diffraction is due to the portion of the spectrum $\tilde{A}(k_x)$ in which $k_x^2 < k_0^2(n_0^2 - n_1^2)$. This portion of the spectrum includes $k_x = \pm k_r$, so that the components of $\tilde{A}(k_x)$ that lead to long-term diffraction also act as a background, canceling out the initial exponential growth in the $\pm x$-directions. During the period of the evolution when the leaky mode dominates, the phases of the continuum background become increasingly mismatched, increasingly revealing the leaky mode at larger values of $|x|$, as we observed in Fig. 2.14.

In Fig. 2.15, we show $I_{\text{norm}} = |A(z, x = 0)|^2/|A(z = 0, x = 0)|^2$ as a function of z/λ. The red dashed curve shows the power of the field using numerical integration. The whole curve can be separated into three regions. In region I, we find the expected exponential decay. In region III, we find the expected algebraic decay, which is proportional to z^{-3} at $x = 0$, according to Eq. 2.39. In the transition region in between, oscillations are visible as the contributions due to diffraction and leakage interfere either constructively or destructively. The green dash-dotted and green solid curves show respectively the steepest descent analysis for the evolution at $x = 0$ and the leaky mode evolution. They agree in the appropriate limits with the exact evolution. We note that we have set $b/a = 2.5$ instead of $b/a = 5$, as in our previous examples. The algebraic decay is difficult to observe, and the larger value of $b/a = 5$ implies a low leakage loss and a low power at the transition point where the decay rate changes from exponential to algebraic. The power at that point is so low that roundoff errors made it impossible for us to observe. In principle, if the input field were perfectly matched to the leaky mode there would not be a transition to algebraic decay, but since perfect matching is impossible given the infinite extent of the leaky mode, the transition will always occur.

2.4 Bandgap slab waveguide

In the slab waveguides that we have studied thus far, the index of refraction in the guiding regions is always higher than in the immediately surrounding regions. However, it is advantageous in some cases to be able to guide waves in a region of lower index of refraction. For example, by filling a region with air, one can greatly lower the nonlinearity. One can confine modes in a lower index region by using the bandgap effect [38], [85], [86]. In a periodically varying medium, like the one shown in Fig. 2.16(a), frequency bands where the light cannot propagate though the periodically varying medium are referred to as bandgaps. By creating a defect in the periodic structure, as shown in Fig. 2.16(b) and launching light at a frequency that is in the bandgap of the periodic structure, one can confine light inside the defect, even when the index of refraction is smaller then in the surrounding regions. In practice, however the periodic variations have a finite extent, as shown in Fig. 2.16(c). In this case, the waveguide is leaky. We will show in this chapter that the leaky modes in these bandgap waveguides behave much like the leaky modes in the W-type waveguides. In optical fibers, an analogous approach has been widely used to confine light to a low-index core. This guidance is referred to as photonic bandgap guidance or capillary guidance [72].

2.4.1 Eigenvalue equation

We begin by considering an infinitely periodic structure, of which Fig. 2.16(a) shows one example. Because Eq. 2.3 is a second-order ordinary differential equation, it must be possible to write any solution $E(x)$ as a superposition of two independent solutions $E_1(x)$ and $E_2(x)$. In particular, since the equation is periodic with period Λ, it must be possible to write $E_1(x+\Lambda) = AE_1(x) + BE_2(x)$ and $E_2(x+\Lambda) = CE_1(x) + DE_2(x)$, where A, B, C, and D are constants that depend on the details of the periodic structure. We may write these two relations in matrix form as

$$\begin{pmatrix} E_1(x+\Lambda) \\ E_2(x+\Lambda) \end{pmatrix} = \begin{pmatrix} A & B \\ C & D \end{pmatrix} \begin{pmatrix} E_1(x) \\ E_2(x) \end{pmatrix}, \tag{2.51}$$

where A, B, C, and D are four constants that depend on the details of the periodic variation with one important constraint. Since Eq. 2.3 has no first derivative terms, its Wronskian will be constant [77]. That implies in turn that $AD - BC = 1$. In order to determine whether propagating solutions to Eq. 3 exist at a given value of β, we first search for a particular set of solutions $E_+(x)$ and $E_-(x)$ that have the property $E_+(x) = \exp(iK_+x)u_+(x)$ and $E_-(x) = \exp(iK_-x)u_-(x)$, where $u_+(x)$ and $u_-(x)$ are strictly periodic in Λ. The existence of $u_\pm(x)$ is guaranteed by the Bloch-Floquet theorem, which holds for any periodic structure. The solutions $E_\pm(x)$ satisfy the conditions $E_\pm(x+\Lambda) = \lambda_\pm E_\pm(x)$, where $\lambda_\pm = \exp(iK_\pm\Lambda)$. We may find $\lambda_\pm$ and hence $K_\pm$ and $u_\pm(x)$ by solving the eigenvalue problem

$$\begin{vmatrix} A-\lambda & B \\ C & D-\lambda \end{vmatrix} = 0 = \lambda^2 - \lambda(A+D) + 1. \tag{2.52}$$

We now infer

$$\lambda_\pm = \frac{A+D}{2} \pm \left[\left(\frac{A+D}{2}\right)^2 - 1\right]^{1/2}. \tag{2.53}$$

From the condition $AD - BC = 1$, it follows that $\lambda_+\lambda_- = 1$, so that $K_+ = -K_-$, and both are purely real or purely imaginary. If $(A+D)^2/4 < 1$, then $K_\pm$ are real, and waves can propagate along x, which is required in order for an initial beam that is introduced at $z = 0$ to propagate in the $+z$-direction. Otherwise, there is no propagation, and an initial beam attenuates. The case shown schematically in

Fig. 2.16(a) in which there are just two different indices has been extensively analyzed in the literature [85], [87]. We consider an example from Ref. 59, in which $\lambda = 1.15$ μm, $n_1 = 2.89$, $n_2 = 3.38$, $n_c = 1$, and $a = b = 0.1$ μm, which applies to the cladding region in the waveguide for a gas laser. In Fig. 2.17, we show the band structure as a function of normalized frequency and propagation constant. The dark areas are the allowed bands, where $(A + D)^2/4 < 1$.

We now consider the case of a defect, shown in Fig. 2.16(b). The lowest-order defect mode will be even, and we write

$$E(x) = \begin{cases} C_1 \cos(k_c x) & 0 \leq x \leq d \\ C_0 u_+(x) \exp(iK_+ x) + D_0 u_-(x) \exp(-iK_- x) & d \leq x \end{cases}, \tag{2.54}$$

where $k_c = (k_0^2 n_c^2 - \beta^2)^{1/2}$, with the condition that $E(x) = E(-x)$ when $x < 0$. Since we are only interested in confined modes within the bandgap, we may assume $K_+ = i\alpha$, where α is real, and $K_- = -i\alpha$. As a consequence, the contribution $D_0 u_-(x) \exp(-iK_- x) = D_0 u_-(x) \exp(\alpha x)$ grows exponentially as $x \to +\infty$, and we must set $D_0 = 0$. Thus, Eq. 2.54 becomes

$$E(x) = \begin{cases} C_1 \cos(k_c x) & 0 \leq x \leq d \\ C_0 u_+(x) \exp(-\alpha x) & d \leq x \end{cases}. \tag{2.55}$$

Matching the function and its derivative at the boundary, we obtain

$$C_1 \cos(k_c d) = C_0 u_+(d) \exp(-\alpha d), \tag{2.56.a}$$

$$-C_1 k_c \sin(k_c d) = C_0 [u'_+(d) - \alpha u_+(d)] \exp(-\alpha d). \tag{2.56.b}$$

Eliminating constant C_1 and C_0, we find the dispersion relation

$$-k_c \tan(k_c d) = \frac{u'_+(d) - \alpha u_+(d)}{u_+(d)}, \tag{2.57}$$

from which the allowed value of β or n_{eff} may be determined. For the example that we are considering, in which $n_1 = 2.89$, $n_2 = 3.38$, $n_c = 1$, $a = b = 0.1$ μm, $d = 6a$, and $\lambda = 11.5a$, we find $n_{\text{eff}} = \beta/k_0 = 0.89295$. We show a picture of $n(x)$ and real part of $E(x)$ in Fig. 2.18.

Finally, we turn to consideration of the leaky mode in the waveguide shown in Fig. 2.16(c). In this case, Eq. 2.55 becomes

$$E(x) = \begin{cases} C_2 \cos(k_c x) & 0 < x \leq d \\ C_1 u_+(x) \exp(-\alpha x) + D_1 u_-(x) \exp(\alpha x) & d \leq x \leq d + M\Lambda \\ C_0 \exp(iK_x x) & d + M\Lambda \leq x \end{cases}, \tag{2.58}$$

where M is the number of periods in the intermediate region, and we set $E(-x) = E(x)$, where $x < 0$. We have $K_x = (k_0^2 n_2^2 - \beta^2)^{1/2}$. We may solve for the propagation constant β and n_{eff} using exactly the same mode-matching technique that we used for the W-type waveguides described in Sec. 2.3.1. In this case, we find $n_{\text{eff}} = \beta/k_0 = 0.89085 + 1.543 \times 10^{-3} i$ when the number of periods $M = 10$.

2.4.2 Alternative solution procedures

In our study of the W-type waveguide, we considered two alternate solution procedures. In the first, we perturbed around the non-leaky solution, assuming that the leakage is small. In the second, we used the complete mode decomposition, which consists of only radiation modes. We showed that both these procedures yield nearly the same answer as a direct determination of the leaky mode solution. The same is true for the bandgap leaky modes.

The perturbation analysis proceeds exactly as in the case of the W-type waveguide. We write $\beta = \beta_0 + \Delta\beta$, substitute this expression into the dispersion relation for the leaky mode, expand in powers of $\Delta\beta$ and keep the zeroth and first order contributions. We thus obtain an expression of the form $M_0(\beta_0)+M_1(\beta_0)\Delta\beta = 0$. Since we are using β_0 from the solution to the non-leaky waveguide, $M_0(\beta_0)$ is only due to the difference between the leaky and non-leaky waveguides and will be small. Using this approach on our example system, we find $n_{\mathrm{eff}} = (\beta_0 + \Delta\beta)/k_0 = 0.89097 + 1.275 \times 10^{-4}i$. The imaginary part is within 20% of what we found using a direct solution in the case with 10 periods in each cladding region.

The analysis using radiation modes again proceeds by analogy to what we found with the W-type waveguide. In Fig. 2.19 we show the $\mathrm{Re}(n_{\mathrm{eff}})$ and the normalized coefficient $P(K_x) = |\tilde{A}(K_x)|^2/\max[|\tilde{A}(K_x)|^2]$ as a function of K_x/k_0 for our example. We keep 2,000 k_x-modes, and we set $B = 1,000\Lambda$. We consider a Gaussian input beam $A(z=0,x) = A_0\exp(-x^2/2d^2)$, where d is half the width of the center region. A sharp Lorentzian peak in $|\tilde{A}(K_x)|^2$ is visible, just as in the case of the W-type waveguide. Using Eq. 2.50 once more to find n_{eff}, we obtain $n_{\mathrm{eff}} = 0.89084 + 1.540 \times 10^{-4}i$, which agrees well with the result that we obtained using the direct method. We note that there are small peaks located between $k_x/k_0 = 1$ and $k_x/k_0 = 3$. The small peaks are not visible in Fig. 2.19(a) on a linear scale, but are visible in Fig. 2.19(b) on a logarithmic scale. These are modes that are confined inside the high-index portions of the bandgap regions by the neighboring lower-index portions. Their mode effective indices are between n_1 and n_2.

Figure 2.20 shows a movie of wave propagation in the leaky bandgap waveguide. Figure 2.21 shows a movie of the transverse mode evolution as the mode propagates along the bandgap slab waveguide with 10 periods. The red dashed curve and blue solid curve show the transverse leaky mode power and the computational solution of

Eq. 2.4, respectively. The power in both curves is normalized to 1 at $x = 0$. As the mode propagates in the $+z$-direction, the mode gradually fills in the power in the outside region of the waveguide. Again, the power that is radiated from the core is not lost; it is simply redistributed from the core into the outside region. Note that the solid blue curve has an irregular shape around the center region. The irregular shape is caused by the small peaks shown in Fig. 2.19(b). If we remove these small peaks in the coefficient function $P(K_x)$, then the irregular fluctuations in the blue solid curve go away.

In Fig. 2.22 we show $\mathrm{Im}(n_{\mathrm{eff}})$ for all three mode-matching methods, for our example system, as we allow the number of periods to grow. Beyond 20 periods, disagreement among them is slight.

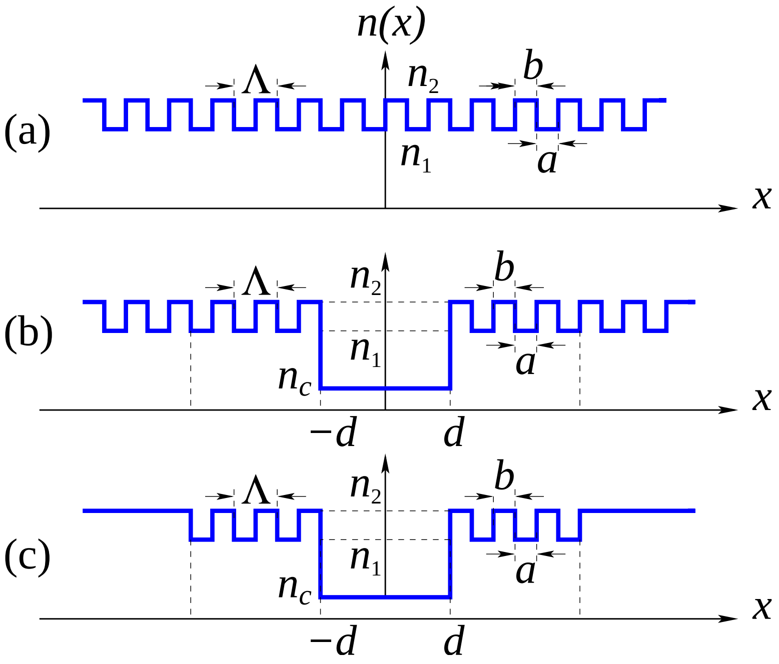

Figure 2.16: The refractive index profile for (a) an infinite periodic structure, (b) an infinite periodic structure with a center defect, and (c) a leaky bandgap waveguide.

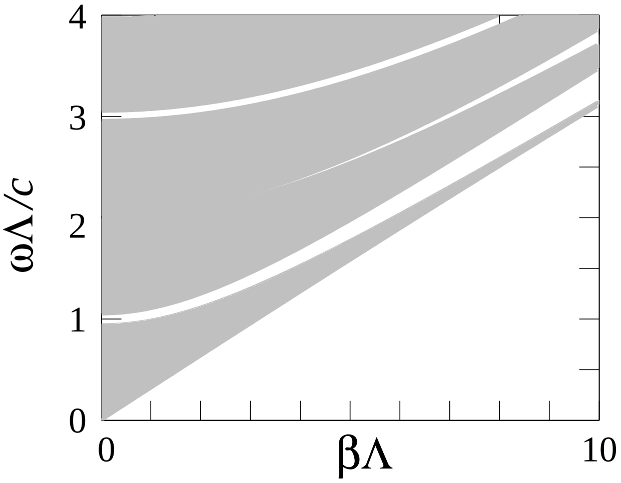

Figure 2.17: Band structure as a function of normalized frequency and propagation constant. The dark area are the allowed bands.

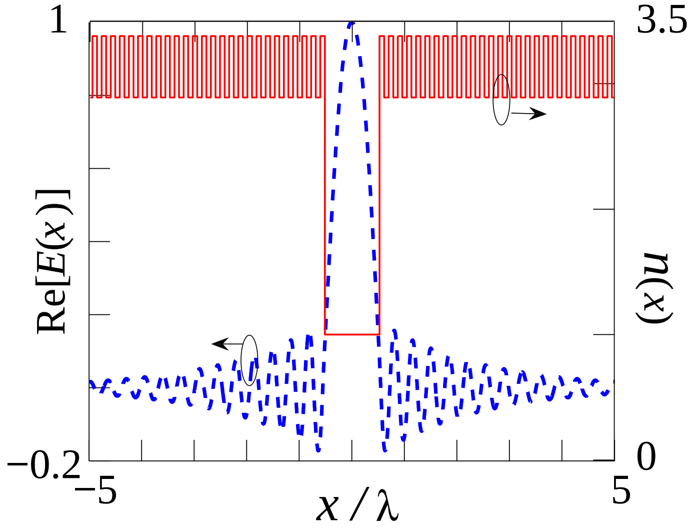

Figure 2.18: Refractive index and real part of $E(x)$ as a function of x.

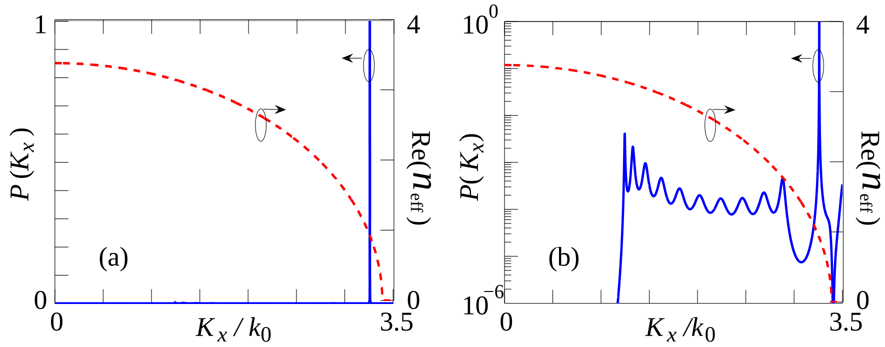

Figure 2.19: The normalized coefficient $P(K_x) = |\tilde{A}(K_x)|^2/\max[|\tilde{A}(K_x)|^2]$ with (a) linear scale and (b) logarithmic scale as a function of K_x and the real part of $n_{\rm eff}$.

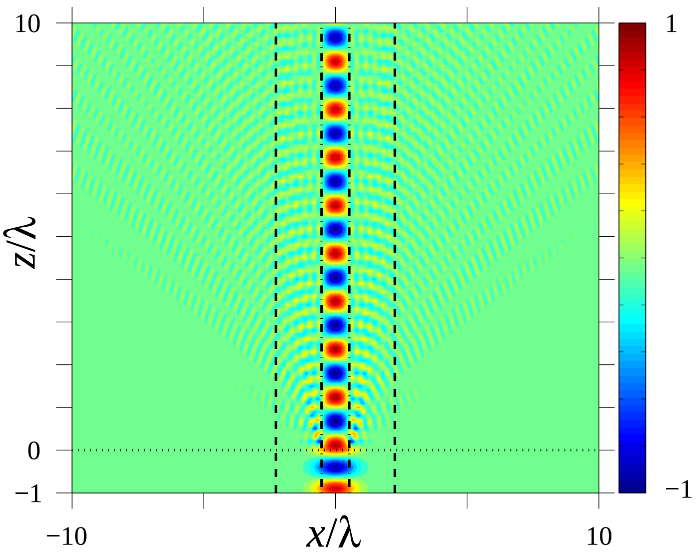

Figure 2.20: Wave propagation in a leaky bandgap waveguide. A beam is injected into the waveguide at $z = 0$. The movie shows the real part of the electric field. The black dash-dotted lines and black dashed lines indicate $x = \pm d$ and $x = \pm(d + M\Lambda)$, respectively.

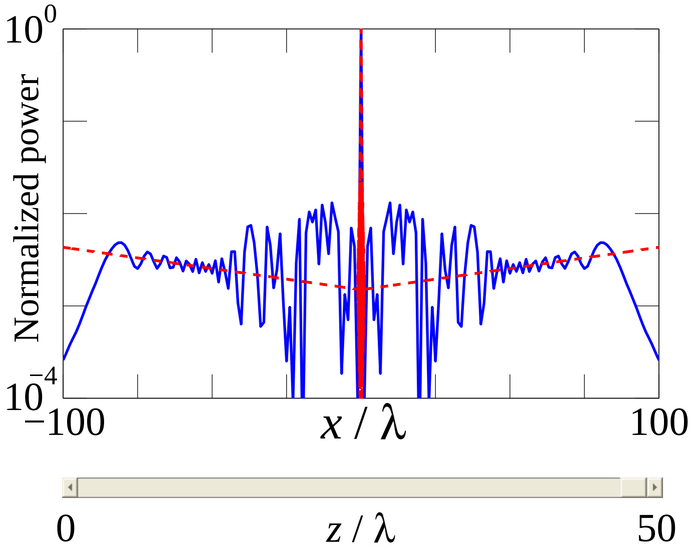

Figure 2.21: Movie of the transverse mode evolution as it propagates along a leaky bandgap slab waveguide. The red dashed curve and blue solid curve represent the power of the leaky mode and the computational solution of Eq. 2.4. The boundary lines are not shown in this figure since they are very close to the center, as shown in Fig. 2.20.

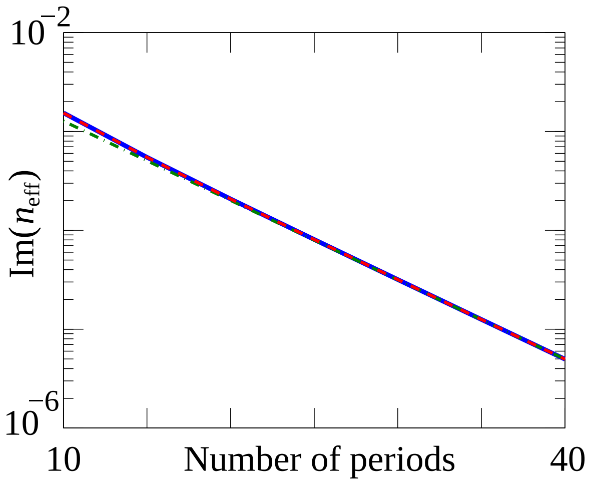

Figure 2.22: Im(n_{eff}) as a function of the number of periods. The blue solid curve, green dash-dotted curve, and red dashed curve represent the leakage loss calculated from the direct determination of the leaky mode solution, the perturbation method, and the determination from the radiation mode solution, respectively.

2.5 Waveguide with absorbing layers

Up to this point, we have solved for the modes in the waveguide by using the fact that in a region in which the index of refraction is constant, the solution can be written exactly as a sum of exponents or a sum of cosines and sines. Matching the solutions and their derivatives across the boundaries of the regions with different indices yields a matrix equation, whose solution produces the propagation constant. In two dimensions, the solution can no longer be written as a sum of exponents, but when each of the regions of constant index of refraction has a circular profile, a closely analogous method based on Bessel functions can be developed and is referred to as the multipole method [35], [36]. When all the indices are real, so that the Helmholtz equation, Eq. 2.3, is self-adjoint, there is a complete mode decomposition that consists of some finite number of guided modes and a continuum of radiation modes. Leaky modes are not part of this complete set, although they can usefully approximate the behavior of nearly guided modes, as we have discussed in detail.

While this approach is the basis for all analytical studies of optical waveguides, it is neither the most useful, nor the most widespread computational approach. Most computational approaches are based on finite-element or finite-difference discretizations of Maxwell's equation [31], [32], [88]. While the discretization in two transverse dimensions is far from trivial to implement, highly robust commercial software is available from several different vendors. The finite-difference and finite-element approaches are highly flexible since they can deal with arbitrary geometries.

In order to simulate outgoing boundary conditions, the finite-difference and finite-element approaches are usually implemented with an absorbing layer at the simulation boundary in which the index of refraction is complex [31]. The goal is to obtain a solution that reproduces as closely as possible, in a limited spatial region, the solution with a lossless medium of infinite extent. That will only be possible if the absorbing layer is far away from the initial beam. However, even given this constraint, the mathematical consequences of adding this absorbing layer are profound. First, all the modes are confined within a finite region, so that the mode decomposition always consists of a countable number of modes as the spatial discretization becomes increasingly fine, as discussed in Sec. 2.1. Second, the equations that describe the wave propagation are no longer self-adjoint, and the modes can no longer be chosen so that they are purely real. The propagation constants are in general complex. Third, we have found that when we approximate the W-type waveguide with a lossless region, surrounded by a lossy region when $|x| > L$, as shown in Fig. 2.23, there is *always* a leaky mode that is part of the complete mode decomposition. That is true even when L is very large, and the maxima of the mode's exponential tails are actually larger than the mode's central peak. As $L \to \infty$, the mode decomposition does not appear to converge to the mode decomposition for the self-adjoint problem, where there is no loss in the waveguide material that we considered in Sec. 2.3. This behavior can be considered a generalization of the result that even with self-adjoint equations, the behavior depends upon the choice of the boundary conditions [74]. Thus, it is important to understand when and why the solutions to this problem can be expected to reproduce the solutions to the problem of a lossless medium of infinite extent.

In practice, the details of the absorbing layer implementation can have a significant impact on the propagation constant of the leaky mode. In order to minimize reflections from the absorbing layers, it has become common to use perfectly matched

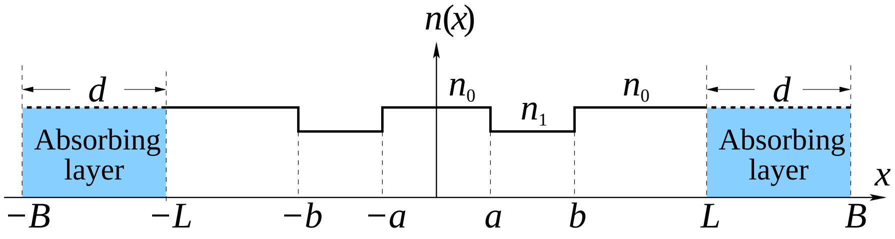

Figure 2.23: Refractive index profile for a W-type waveguide with absorbing layers.

layers — a technique that was first introduced in finite-difference time domain simulations [89], [90]. An ideal perfectly matched layer is a layer that gives no reflection at any frequency and angle. However, it is important to recognize that once spatially discretized, the perfectly matched layers are no longer "perfectly matched" and reflections from them do occur [90]. In our prior studies of two-dimensional waveguides, we have found that shifting the location of the absorbing layer slightly can make a difference in the propagation constant that far exceeds the roundoff or discretization error.

In the remainder of this chapter, we discuss the optimization of the absorbing layer and then discuss the complete mode decomposition and the role of the leaky mode for a simple finite-difference method with absorbing boundary layers.

2.5.1 Optimization of the absorbing layer

Figure 2.23 shows the structure of a symmetric W-type waveguide with absorbing layers. We have chosen not to implement perfectly matched layers in order to simplify the discussion and because they offer little or no advantage relative to a straightforward absorber for the discretization that we use. We use a simple finite-difference method, so that Eq. 2.3 becomes

$$\frac{1}{\Delta^2}[E(x_{k-1}) - 2E(x_k) + E(x_{k+1})] + [k_0^2 n^2(x_k) - \beta^2]E(x_k) = 0, \tag{2.59}$$

where $x_k = -B + (k-1)\Delta$ and $\Delta = 2B/(N-1)$ is the discretization width. The index k varies from 1 to N, where the simulation window extends from $-B$ to B. The index of refraction $n(x_k)$ is real when $|x_k| \leq L$ and is complex when $|x_k| > L$. The problem of solving Eq. 2.59 is thus a matter of finding the N eigenvalues β of the $N \times N$ matrix in Eq. 2.59, where for convenience we have applied Dirichlet boundary conditions, setting $E_0 = E_{N+1} = 0$. This choice of boundary condition does affect the mode decomposition, but has no significant effect on the leaky mode.

The permittivity of the absorbing layer is

$$\epsilon = n_0^2 \left[1 + i \left(\frac{|x| - L}{d} \right)^2 s' \right], \tag{2.60}$$

where s' is a parameter that we choose to minimize the reflections. Figure 2.24 shows $\mathrm{Im}(n_{\mathrm{eff}}) = \mathrm{Im}(\beta)/k_0$ as a function of L/λ, where β is the propagation constant of the leaky mode that we obtain from the solution of Eq. 2.59. We have chosen $b/a = 5$, $n_1 = 0.96 n_0$, $n_0 = 1.45$, and $ka(n_0^2 - n_1^2)^{1/2} = 1$, which are the same parameters as in Sec. 2.3.1. We have set $N = 10^5$. The blue dash-dotted curve, dashed curve and dotted curve show the results with normalized absorbing layer widths $d/\lambda = 5$, 10, and 15, respectively. We have set $s' = 1$ in all three cases. The red solid curve shows the results from Eq. 2.42. We see that $\mathrm{Im}(n_{\mathrm{eff}})$ varies sinusoidally, and its magnitude diminishes rapidly as d/λ increases. These oscillations are due primarily to reflections from the boundary at $x = \pm B$. The boundary produce strong reflection when the width of the absorbing layer is too small. In Fig. 2.25, we show the results when $s' = 5$, 2, and 1. The red solid curve shows the result from eigenvalue Eq. 2.42. The normalized width of absorbing layer d/λ is set to be 15 for all three cases. A large value of s' leads once again to large oscillations, primarily due to reflections

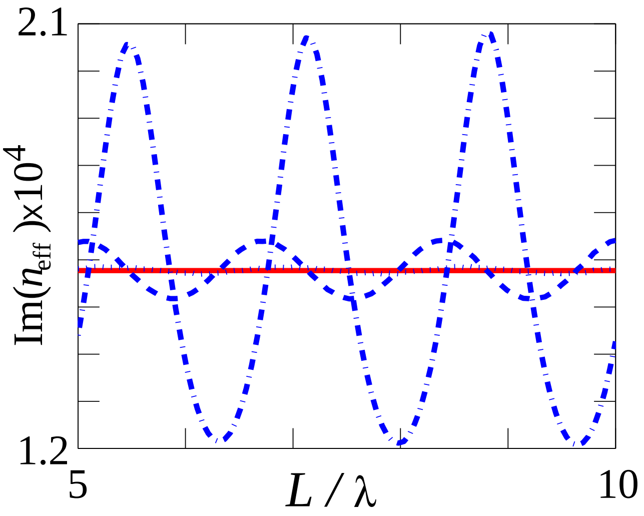

Figure 2.24: $\mathrm{Im}(n_{\mathrm{eff}}) = \mathrm{Im}(\beta)/k_0$ as a function of L/λ. The blue dash-dotted curve, dashed curve, and dotted curve show the results with normalized absorbing layer widths $d/\lambda = 5$, 10, and 15, respectively. The red solid curve shows the results from Eq. 2.42.

from within the absorbing layer, close to $|x| = L$. In Fig. 2.26, we look in more detail at the behavior of $\mathrm{Im}(n_{\mathrm{eff}})$ as s' varies from 10^{-2} to 10. At each value of s', we calculated the average value of $\mathrm{Im}(n_{\mathrm{eff}})$ and the standard deviation for 100 evenly-spaced values of L/λ as we allow it to vary from 5 to 10. When $s' < 0.04$, the reflection from the boundary at $\pm B$ causes a large error and hence a large standard deviation. When $s' > 1$, the reflection at the absorbing layer cause a large error and a large standard deviation. Any value between $s' = 0.04$ and $s' = 1.0$ yields nearly the same average, which is about 1.578×10^{-4}, but, for a single computation, it is better to use $0.04 < s' < 0.1$ so that the standard deviation is low.

In general, it is useful to use absorbing layers with different values of L and then to average the results for $\mathrm{Im}(n_{\mathrm{eff}})$.

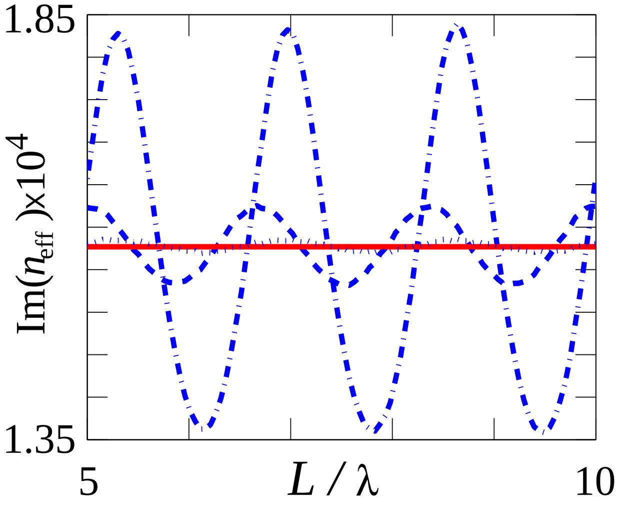

Figure 2.25: $\text{Im}(n_{\text{eff}}) = \text{Im}(\beta)/k_0$ as a function of L/λ. The blue dash-dotted curve, dashed curve and dotted curve show the results with $s' = 5$, 2, and 1, respectively. The red solid curve shows the results from Eq. 2.42.

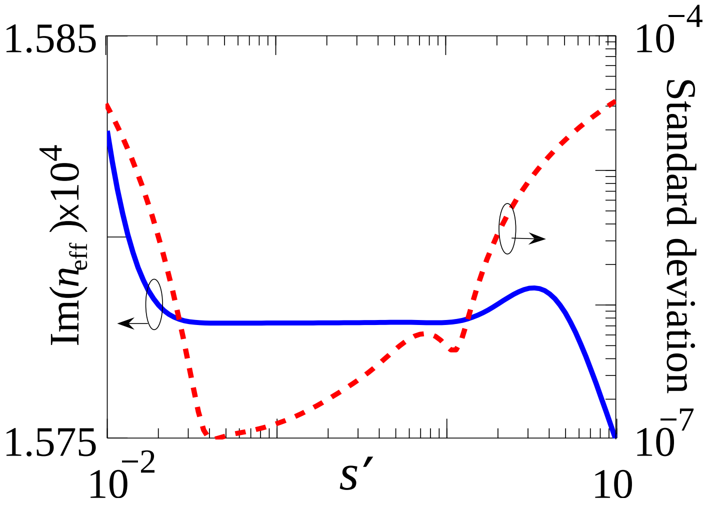

Figure 2.26: The average value of $\text{Im}(n_{\text{eff}})$ and the standard deviation for 100 evenly-spaced values of L/λ as we allow it to vary from 5 to 10.

2.5.2 Mode decomposition and the leaky mode

Equation 2.59 has the form of a matrix eigenvalue problem

$$(\mathsf{M} - \beta^2 \mathsf{I})\mathbf{E} = 0, \tag{2.61}$$

where I is the identity matrix, and, letting $\delta_{j,k}$ denote the Kronecker delta function, the matrix element

$$M_{j,k} = \frac{\delta_{j-1,k} - 2\delta_{j,k} + \delta_{j+1,k}}{\Delta^2} + k_0^2 n_k^2 \delta_{j,k} \tag{2.62}$$

is the j,k-th element of the matrix M. The vector $\mathbf{E}$ is a column vector, whose k-th element is $E(x_k)$. We note that M is a symmetric matrix, which automatically implies that it is normal, *i.e.*, $\mathsf{M}\mathsf{M}^\dagger = \mathsf{M}^\dagger\mathsf{M}$. That in turn implies that its eigenvectors form a complete set [91], so that we may write

$$A(x_k) = \sum_{l=1}^{N} \tilde{A}_l E_l(x_k), \tag{2.63}$$

where the $E_l(x_k)$ denotes the k-th element of the column vector $\mathbf{E}_l$, and the $\mathbf{E}_l$ are solutions of the right eigenvalue equation

$$(\mathsf{M} - \beta^2 \mathsf{I})\mathbf{E}_l = 0, \tag{2.64}$$

Equation 2.63 is the discretized version of Eq. 2.10 in Sec. 2.1. In principle, we may find the $\tilde{A}_l$ by defining left eigenvectors that satisfy

$$\mathbf{F}_l^T(\mathsf{M} - \beta^2 \mathsf{I}) = 0, \tag{2.65}$$

where $\mathbf{F}_l$ is a column vector and $\mathbf{F}_l^T$ is the corresponding row vector, and noting

$$\tilde{A}_l = \sum_{l=1}^{N} A(x_k) F_j(x_k). \tag{2.66}$$

Because the matrix M is symmetric, we find $F_l(x_k) = E_l(x_k)$. To determine the field at any x_l and any z, we use the expression

$$A(z, x_k) = \sum_{l=1}^{N} \tilde{A}_l E_l(x_k) \exp(i\beta_l z), \tag{2.67}$$

where we stress that the β_l are in general complex. Equation 2.67 is the analog to Eq. 2.4 for the finite-difference method and is the discretized version of Eq. 2.11.

In Fig. 2.27, we show the $\mathrm{Re}(n_{\mathrm{eff}})$ and $\mathrm{Im}(n_{\mathrm{eff}})$. We set $N = 500$ in this case. We use the same parameters as in Sec.2.3.4 with $L/\lambda = 15$, $(B - L)/\lambda = 15$, and $s' = 1$. We arrange the indices from small $\mathrm{Re}(n_{\mathrm{eff}})$ to large $\mathrm{Re}(n_{\mathrm{eff}})$, which corresponds roughly to arranging the indices from large $|k_x|$ to small $|k_x|$. In this case, mode number 476 corresponds to the leaky mode. Its imaginary part is substantially lower than its neighbors. It is the modes with small indices, corresponding to $k_x^2 > k_0^2(n_0^2 - n_1^2)$, that contribute to the early-term diffraction. All these modes are more lossy than the leaky mode. There is one mode with a lower $\mathrm{Im}(n_{\mathrm{eff}})$ than the leaky mode, which is mode no. 498. This mode is the lowest-order cavity mode that is confined in between the absorbing layer and the layer with low index of refraction n_1. In general, the loss of the cavity modes is low because their transverse derivatives are small, implying from Eq. 46 that they have little outward flux into the absorbing region. Modes no. 499 and 500 are cladding modes that are located almost entirely in the absorbing regions and have high loss.

In Fig. 2.28, we show a movie of the transverse normalized power of the same Gaussian input beam that we considered in Sec. 2.3.4, as it propagate along the waveguide with the same parameters as in Sec. 2.3.1 and with $L/\lambda = 15$, $(B-L)/\lambda = 15$, and $s' = 1$. We also show the power of the leaky mode as the red dashed curve.

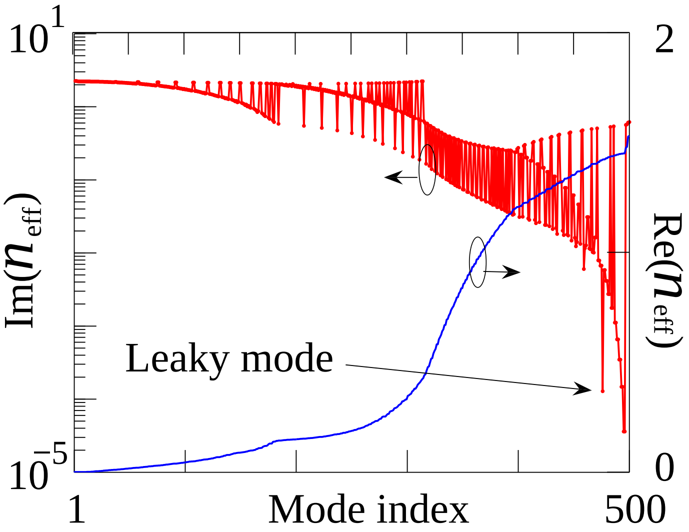

Figure 2.27: The $\mathrm{Re}(n_{\mathrm{eff}})$ and $\mathrm{Im}(n_{\mathrm{eff}})$ for all 500 eigenmodes.

We have normalized the peak of the mode power profiles to 1. There are several different propagation regions. First, the field leaks into the outer region of the W-type waveguide in which $b < |x| < L$ and almost exactly reproduces the profile of the leaky mode, although small oscillation are visible for $2 < x/\lambda < 20$, just as shown in Fig. 2.14. However, when $z/\lambda > 10,000$, the lowest-order cavity mode becomes the dominant mode. The distance at which it dominates is determined by the magnitude of its small, but finite overlap with the initial beam. Since this cavity mode is primarily located in the region $b < |x| < L$, the profile of the power changes significantly once this cavity mode becomes dominant. The lowest-order cavity mode eventually dominates because it has a lower value of $\mathrm{Im}(n_{\mathrm{eff}})$ then any other mode, including the leaky mode, and because it has a small, but non-zero overlap with the initial beam. It is possible in principle to launch an initial beam that has no overlap with this cavity mode or, in fact, is a pure leaky mode. However, one cannot do so when the initial beam is localized in the center of the simulation window, as

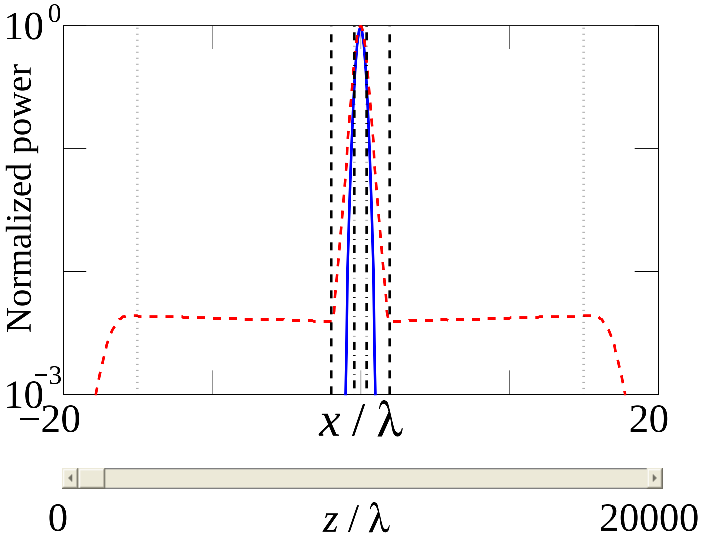

Figure 2.28: Movie of the transverse normalized power of the same initial Gaussian beam that we considered in Sec. 2.3.4. We also show the power of the leaky mode as a red dashed curve. We have normalized the peak of the mode power profiles to 1. The black dash-dotted lines, black dashed line, and black dotted lines indicate $x = \pm a$, $x = \pm b$, and $x = \pm L$, respectively.

is always required in a realistic simulation. In practice, any initial beam will be composed of many modes, of which the leaky mode is just one. Figure 2.29 shows $I_{\mathrm{norm}} = |A(z, x = 0)|^2/|A(z = 0, x = 0)|^2$ as a function z/λ for a Gaussian input beam. The beam and waveguide parameters are the same as in Fig. 2.27. Due to the large attenuation, normalization is needed to view these results. The red solid curve shows the result keeping all 500 modes, while the blue dashed curve shows the result keeping only the leaky mode. This figure is analogous to Fig. 2.15, in which long-term diffraction ultimately dominates the evolution. In this case, however, the attenuation at large z is still exponential, but the attenuation occurs at a slower rate than in the case of the leaky mode, because the energy ultimately resides in the lowest-order cavity mode, rather than a continuum of radiation modes.

In Fig. 2.30, we show a slide show for the input wave (blue solid curves) and its de-

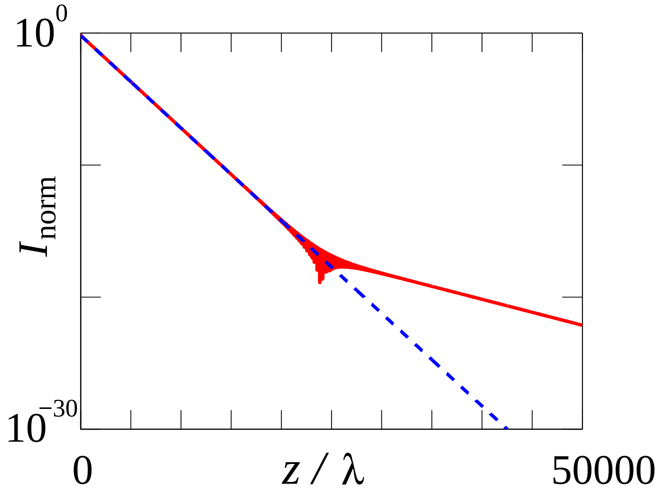

Figure 2.29: $I_{\text{norm}} = |A(z, x = 0)|^2/|A(z = 0, x = 0)|^2$ as a function z/λ for a Gaussian beam. The red solid curve shows the result keeping all 500 modes, while the blue dashed curve shows the result keeping only the leaky mode.

composition into the eigenmodes (red dashed curves). Starting with the leaky mode, which has index number 476, we add the other eigenmodes with their coefficients $\tilde{A}_l$. We see that the other modes ultimately cancel the tails of the leaky mode, so that the mode profile represents the Gaussian input beam. Since these modes attenuate more rapidly than the leaky mode, the leaky mode is ultimately revealed as the wave propagates along the waveguide. This behavior is different from the infinite guide where no modes attenuate and the leaky mode is only revealed in a finite region surrounding the center by diffraction of the continuum of radiation modes. However, the behavior in the central region is still the same in both cases up to the point where the large-z behavior begins to dominate the evolution.

In the example that we considered here, the leaky mode does not have large exponential tails. However, we have examined the behavior as L and B become large. As long as d is large enough and s' is not too big, so that reflections from the absorbing regions are avoided, the qualitative behavior is unchanged. There is always

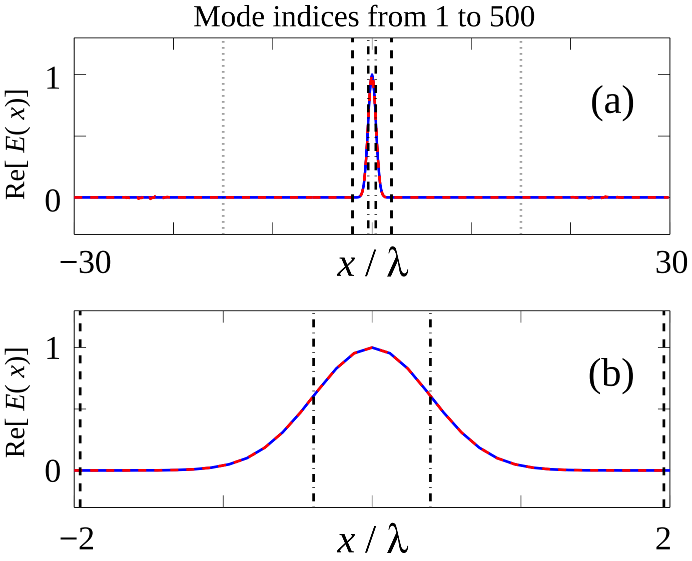

Figure 2.30: Slide show for the input wave (blue solid curves) and its decomposition into the eigenmodes (red dashed curves). In (b), we show the central region from (a). The black dash-dotted lines, black dashed line, and black dotted lines indicate $x = \pm a$, $x = \pm b$, and $x = \pm L$, respectively.

a leaky mode that dominate the evolution until z becomes large, at which point one or more cavity modes dominate the evolution. We have observed the following points: As L increases, keeping b/a fixed, so do the maxima of the exponential tails of the leaky modes. Ultimately theses tails become bigger at their maxima then the central peak of the mode. Nonetheless, the leaky mode is a real mode of this waveguide system. Additionally, as L increases the number of cavity modes with less attenuation than the leaky mode increases. However, the lowest order cavity mode always has the lowest loss and ultimately dominates the evolution.

2.6 Answers to the introductory questions

There are two basic types of computational methods that are used to find optical waveguide modes. One type is mode-matching methods, in which one uses exact analytical solutions in regions where the index of refraction is constant and matches the solutions and their derivatives at the boundaries. In the case of slab waveguides, one uses exponential functions. The other type is finite-difference and finite-element methods.

When using mode-matching methods, it is usual to specify the problem in a lossless waveguide so that the index of refraction is real at all points in the space. In this case, all the waveguide modes are lossless and have real propagation constants. If the index of refraction becomes equal to a constant value at some finite distance from the origin, then in general there is a continuum of radiation modes and a finite number of discrete guided modes. Any physically reasonable initial profile can be decomposed into a generalized sum over the waveguide modes, in which the sum includes an integral over the radiation modes. One can then determine the beam profile at any subsequent point in the waveguide by multiplying the amplitude of each mode by an appropriate exponential factor and then re-summing the modes.

This problem is equivalent mathematically to the quantum-mechanical problem of a particle that is confined in a potential well, and the set of facts just stated is often repeated in elementary textbooks on quantum mechanics and waveguide theory. The proof is, however, far from trivial [74]. It begins with a finite region in space with boundary conditions that ensure that the eigenvalue problem — given in our case by Eq. (3) — remains self-adjoint. In this case, one has a countably infinite set of modes. As one lets the boundary tend toward infinity, most of the modes coalesce into a continuum, leaving a finite set of guided modes. This continuum will always contain both outgoing and incoming waves. That occurs because self-adjoint boundary conditions on a finite region of space always lead to reflections, so that as the boundary tends toward infinity, there are always waves propagating both outward and inward. Because of its importance in quantum mechanics, as well as optical waveguides, the theory of self-adjoint eigenvalue equations has been extensively studied.

Given the complete mode decomposition into a continuum of radiation modes and a finite number of guided modes, the light evolution in the three-slab waveguide of Fig. 2.1(a) is not difficult to understand. The portion of the beam profile that couples into the guided modes remains confined, while the portion that couples into the radiation modes diffracts.

By contrast, the evolution of the light in the W-type waveguide, in which only a continuum of radiation modes is present, is not so easy to understand. The key point is that the continuum contains sharp Lorentzian peaks at values of k_x that nearly equal the transverse wavenumbers of the central portion of the guided modes of the corresponding three-slab waveguide. Immediately after a beam is injected into the waveguide, there is a transient stage in which a portion of the energy rapidly diffracts, in close analogy to the behavior in a three-slab waveguide. However, Lorentzian peaks in the continuum quickly dominate the early evolution, leading to leaky modes whose damping rates are given by the inverse widths of the Lorentzian peaks. The amplitudes corresponding to all the transverse wavenumbers in a Lorentzian peak are initially in phase, but when the propagation distance becomes long enough so that these amplitudes are out of phase, then long-term diffraction dominates. This long-term diffraction, which corresponds to the dissolution of the leaky mode and occurs outside the central region of the waveguide, should not be confused with the early-term diffraction, during which the initial beam settles down into the shape of the leaky mode in the central region of the waveguide. In effect, the continuum can be decomposed into three contributions — a smooth portion at large transverse wavenumbers that leads to the rapid initial diffraction, Lorentzian peaks that correspond to the leaky modes, and a smooth background to the Lorentzian peaks that compensates for the exponential growth at large transverse distances and leads to diffractive radiation at large propagation distances.

While leaky modes can be understood as a consequence of the Lorentzian peaks in the continuum, that does not explain the evolution of their exponential growth transverse to the direction of propagation. We have found that this exponential growth is real within a limited transverse distance surrounding the origin, and this transverse distance continues to grow as long as the leaky mode dominates over the long-term diffraction. Using conservation of flux, we have shown that any mode that decreases exponentially as it propagates must increase exponentially transverse to the direction of propagation once the transverse dimensions are large enough so that the index of refraction equals its final constant value. However, exponential growth that extends to infinity is unphysical. There have been attempts in the literature to bypass this problem by claiming that at some transverse distance the material becomes lossy or interacts with air, and the problem goes away. However, the protective coating or air is often very far from the region of interest, so that it is easier both mathematically and computationally to treat the medium as though the indices of refraction at the boundary of the region of interest extended to infinity. Invoking a protective coating or air does not help us understand how the appearance of leaky modes in the mathematical formulation of the problem as a lossless waveguide can provide useful numbers or even be consistent with physical reality.

The Lorentzian peaks in the continuum, if separated from the continuum background lead to solutions that grow exponentially in the transverse dimension. The background cancels this exponential growth. As the light propagates, the different components of the background evolve so that they are increasingly out of phase, revealing the exponential growth. This trend continues until the components of the Lorentzian peaks evolve so that they are also out of phase. Thereafter, long-term diffraction dominates the evolution.

Remarkably, the basic behavior that we have just described remains the same in far more complex systems than the three-slab and W-type waveguides that were the focus of most of our discussion. We demonstrated this point in detail for the important case of bandgap waveguides, but it remains true when the transverse structures become two-dimensional.

When using finite-difference or finite-element methods, it is usual to surround the region of interest with a lossy region, whose purpose is to absorb outgoing waves. For the class of problems that we are considering here, in which the index of refraction reaches a constant value at some finite distance from the origin, the absorbing boundary would typically be placed shortly beyond the distances at which the constant value is reached. The wave flux is strictly outwards in the lossless problem at transverse distances that are both beyond the initial beam width and beyond the points at which the index of refraction reaches its final value. Hence, one expects physically that surrounding the region of interest with an absorbing layer will produce the same behavior within the region of interest as does a lossless guide that extends to infinity. Some sort of absorber is needed because any lossless boundary conditions in a finite spatial region will produce reflections, which very visibly changes the behavior in the region of interest!

Due to their flexibility and the ease relative to other methods with which they can be numerically implemented, finite-difference and finite-element methods are the methods of choice in geometries with any significant complexity. As a consequence, considerable effort has gone into developing algorithms for absorbing layers that reflect as little as possible, while using as small a number of node points as possible [5]. The absorbing layer must be optimized for each geometry, and we showed how this optimization procedure works in the case of a simple finite-difference scheme and a simple absorber for the W-type waveguide.

As long as the absorbing layer has been optimized to produce negligible reflections and the number of points is sufficiently large on a well-chosen mesh, then the finite-difference and finite-element methods will produce results for the evolution of an initially localized beam that agrees in the region of interest with the results of the mode-matching methods for some finite propagation distance. Moreover, the damping rates for the leaky modes will agree. Not surprisingly, mode-matching methods produce different results from the finite-difference and finite-element methods when the energy that is outside the region of interest becomes large.

While the finite-difference and finite-element methods may produce the same results for the quantities of interest as do the mode-matching methods, it is important to recognize that the mathematical problem has profoundly changed and so has the mode decomposition. Since the problem formulation is no longer self-adjoint, one can no longer use the mathematical apparatus that was developed for self-adjoint problems. Indeed, there is no guarantee in general that the modes constitute a complete set, although we showed that the decomposition was complete for the simple case that we considered. Hence, the completeness must be verified on a case-by-case basis.

For the simple finite-difference algorithm that we considered, we observed the following differences from the mode-matching method: (1) The mode decomposition consists of a finite number of discrete modes. That will be the case for *any* finite-difference or finite-element method. (2) The leaky mode is a real mode of the system. (3) The transverse exponential behavior is revealed when modes that have larger loss than the leaky mode attenuate. There is no real diffraction, although the evolution reproduces the early-term diffraction. (4) There are one or more cladding modes that have less loss than the leaky mode. These cladding modes decay exponentially, but at a slower rate than the leaky mode. Algebraic decay associated with long-term diffraction is not observed.

It might seem surprising at first that the mode decomposition used with mode-matching methods and the mode decomposition used with finite-difference or finite-element methods should yield the same result for the quantities of interest when the decompositions differ so profoundly. However, it is a reflection of a deep result that can be found throughout physics. A problem can often be formulated in two different ways. As long as both formulations are correct, they must yield the same results. Often these formulations lead to different, complementary physical pictures of the phenomenon being studied. That is the case here.

Chapter 3

Leakage loss and bandgap analysis for nonsilica glasses

Air-core photonic bandgap fibers (PBGFs), in contrast to some other types of holey fiber, guide light through the photonic bandgap effect, instead of using total internal reflection [10], [11]. PBGFs have the potential to provide very low-loss transmission, along with delivery of high power and low nonlinearity. Due to the finite number of air hole rings, the modes in the air-core PBGFs are leaky modes. Research on silica fiber shows that a larger air-hole-diameter-to-pitch ratio, d/Λ, in air-core PBGFs leads to wider bandgaps and hence better mode confinement [20]. Pitch, Λ, is defined as the distance between the centers of the nearby holes. Pottage, *et al.* suggest using lower d/Λ to obtain a wider bandgap for high-index glass [21]. The assumption is that a wider relative bandgap leads to lower leakage loss. However, the loss due to mode leakage in high-index glass with lower d/Λ has not been previously calculated, and this assumption has remained unverified until now. In this chapter, we show a calculation of the relative bandgap in which we varied the d/Λ and the refractive index. We show two peaks in a relative bandgap contour plot in the range of the d/Λ and the refractive index we considered. Then, we show that with a refractive index of

2.4, which is close to the refractive index of chalcogenide fiber at $\lambda = 4$ μm [92], [93], there is an optimal d/Λ at about 0.8 that minimizes the loss. Also, we show that the d/Λ for the minimum loss and maximum relative bandgap coincide for a wide range of refractive index. Thus the simple unit-cell plane-wave analysis, although it cannot be used directly to calculate the loss due to leakage, correctly predicts the optimal operating d/Λ of air-core PBGFs in the cases that we studied, as Pottage, *et al.* suggested [21]. Although the material loss is not included in the simulation, the analysis of leakage loss indicates the minimum possible loss for the PBGF design.

3.1 Bandgap and mode analysis

In the plane-wave analysis, one assumes a periodic structure, so that this analysis cannot be used to calculate the loss due to leakage. We use the full-vectorial plane-wave method to obtain the bandgap in a two-dimensional photonic crystal cladding arranged in a triangular pattern [94]. We used a grid resolution of $\Lambda/128$ and verified that the difference between these results and the results with a grid resolution of $\Lambda/64$ differ by less than 1%. Figures 3.1(a) and (b) show the calculated bandgap diagrams for a refractive index of 1.45 with an d/Λ of 0.9 and a refractive index of 2.4 with an d/Λ of 0.8, respectively. We note that the normalized frequency $\omega\Lambda/2\pi c$ shown on the ordinate is also equal to the pitch-wavelength ratio Λ/λ. In these figures, the dashed lines represent the bandgap edges of the photonic crystal cladding. The solid lines represent the air lines. We found several bandgaps that cross the air line in our range of interest. In order to choose the best bandgap, we define a relative air-crossing bandgap or simply a relative bandgap, as the ratio of the bandgap intersection with the air line and the middle of bandgap in the air line, which

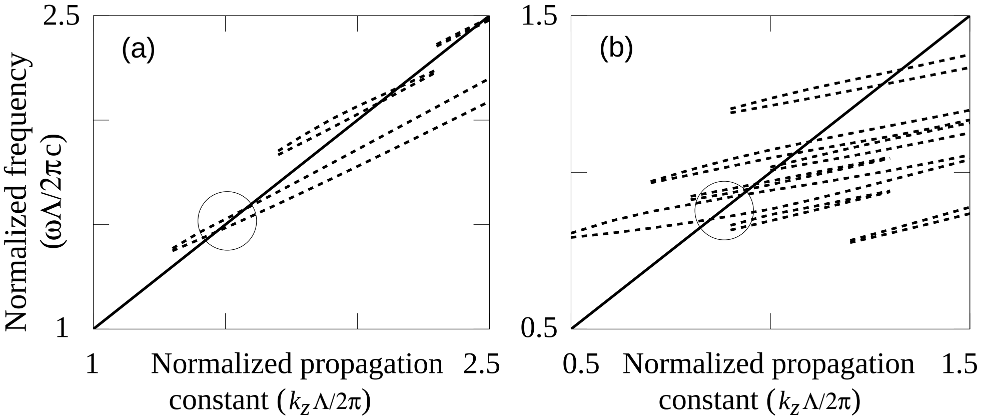

Figure 3.1: Bandgap diagrams for (a) a refractive index of 1.45 with a d/Λ of 0.9 and (b) a refractive index of 2.4 with a d/Λ of 0.8, respectively.

is the same as the normalized gap width defined in Ref. 21. This definition takes into account that bandgaps at larger frequencies must open more widely to have losses comparable to bandgaps at lower frequencies. We circle the largest relative bandgaps in Figs. 3.1(a) and (b). In Fig. 3.2, we plot the relative bandgap contour plot as a function of the d/Λ and the refractive index. We choose a maximum refractive index of 2.8 since commercial optical-fiber glasses do not have refractive indices higher than 2.8 [14], [21]. In this figure, the black x-marks represent the d/Λ corresponding to the maximum relative bandgap at each refractive index. Two black dashed curves connect x-marks in the two relative bandgap maxima in the contour plot. There exists a discontinuity of the maximum relative bandgap around a refractive index of 1.8. This discontinuity occurs because the bandgap with the maximum relative bandgap changes.

We found that for a refractive index below 1.8, the relative bandgap always increases as the d/Λ increases when the d/Λ is larger than 0.9, as shown in the peak at high d/Λ and low refractive index in Fig. 3.2. This behavior can be understood by

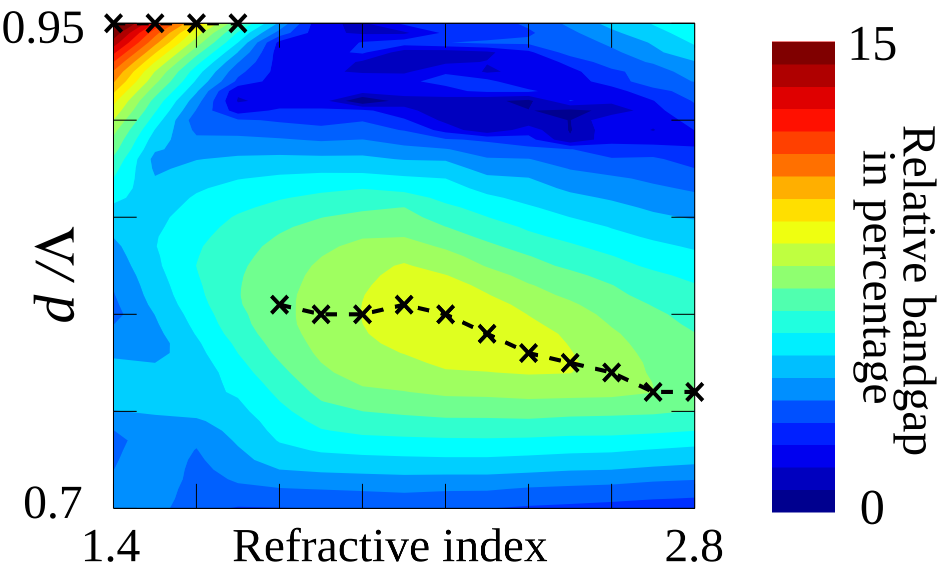

Figure 3.2: The contour plot for the maximum relative bandgap. The black x-marks represent the d/Λ corresponding to the maximum relative bandgap at each refractive index. Two black dashed curves connect x-marks in the two relative bandgap maxima in the contour plot. There exists a discontinuity of the maximum relative bandgap around a refractive index of 1.8.

examining the mode structure at the extrema of the bands that surround the largest relative bandgap. Figure 3.3 shows the band diagram when we use a refractive index of 1.45 and a d/Λ of 0.92, with a normalized propagation constant equal to $k_z\Lambda/2\pi$ = 1.6. The largest relative bandgap occurs between bands 4 and 5, and the extrema occur at the Γ point. Figures 3.4(a) and (b) show the normalized magnitude of the Poynting flux in the 4th and 5th bands. Note that most of the flux in the 4th band is located in the spots, which are the large glass regions between three holes in the triangular structure. However, most of the flux in the 5th band is located in the veins, which are the long thin connections between two spots. As the d/Λ increases and the veins become thinner, the flux in the 4th band remains almost unchanged in the spot, but the flux in the 5th band is pushed into the air. Figure 3.5 shows the fill factor for the 4th and 5th bands as a function of d/Λ. Fill factor is an appropriate

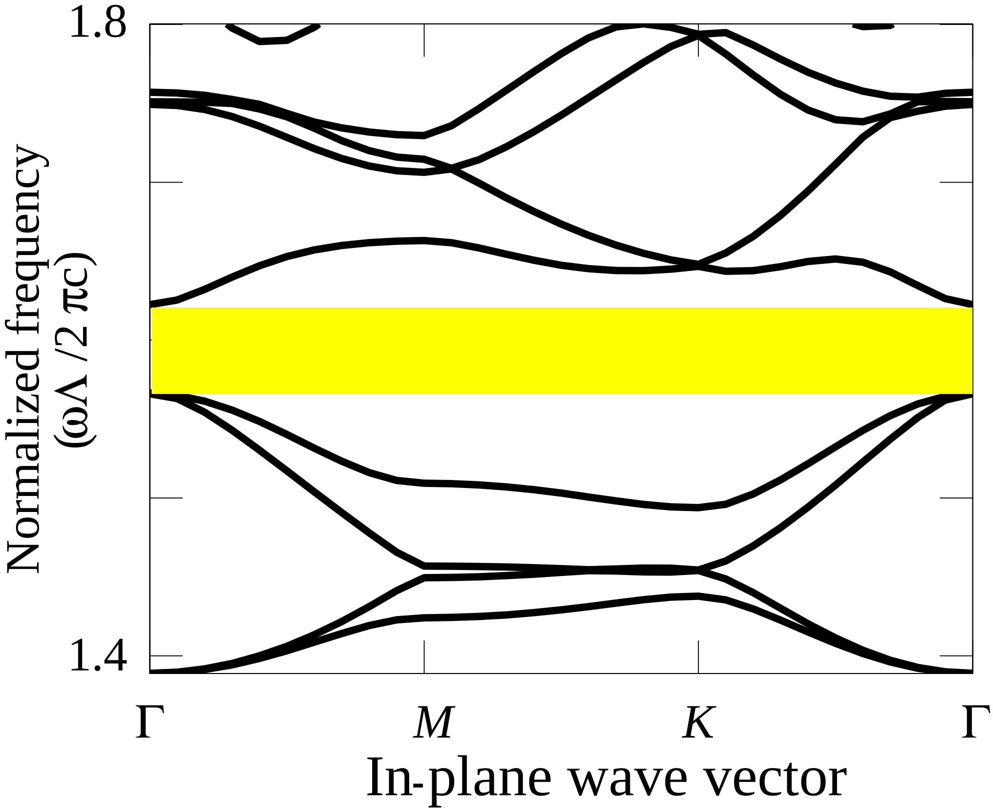

Figure 3.3: Band diagram when we use a refractive index of 1.45 and a d/Λ of 0.92. Yellow indicates the largest relative bandgap.

measure of the degree of concentration of the displacement fields in the glass regions, defined as [95]

$$f = \frac{\int_{\text{glass}} [|\mathbf{D}(x,y)|^2/\epsilon(x,y)]dxdy}{\int_{\text{all space}} [|\mathbf{D}(x,y)|^2/\epsilon(x,y)]dxdy}. \tag{3.1}$$

Red dashed and blue solid curves in Fig. 3.5 represent the fill factor for the 4th and 5th bands, respectively. The fill factor for the 5th band decreases faster than the fill factor for the 4th band as the d/Λ increases. It has been shown that the mode's frequency decreases at a fixed propagation constant k_z when the displacement field $\mathbf{D}$ is concentrated in the regions of high dielectric constant [95]. Hence, the frequency increase in the 5th band is faster than the increase in the 4th band as the d/Λ

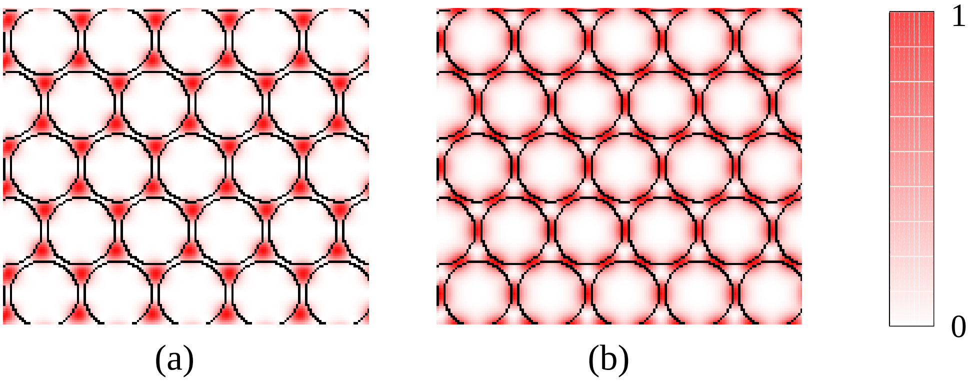

(a) (b)

Figure 3.4: Magnitude of Poynting flux, normalized to the peak, in the (a) 4th and (b) 5th band. The red regions correspond to a large Poynting flux. Most of the flux in the 4th band is located in the spots, which are the large glass regions between three holes in the triangular structure. However, most of the flux in the 5th band is located in the veins, which are the long thin connections between two spots.

increases, which implies that the bandgap opens wider. This result agrees with the loss analysis in Fig. 9 of Ref. 20, which demonstrated that a higher d/Λ always yields lower loss when the normalized frequency is optimized using a refractive index of 1.45. On the other hand, if we increase the refractive index, the mode's frequency decreases for each k_z and eventually falls below the airline, so that air-guided modes are no longer possible.

By contrast, when the refractive index is above 1.8, the relative bandgap has a maximum at an d/Λ of about 0.8. To understand this behavior, we show in Fig. 3.6 the band diagram when we use a refractive index of 2.4 and a d/Λ of 0.75, with a normalized propagation constant equal to $k_z\Lambda/2\pi = 0.8$. In this figure, we find that the bandgap between the 8th and 9th bands dominates. Point M-K is the point where the highest frequency in the 8th band is located. In Fig. 3.7(a), the red solid and dashed curves represent the lowest frequency in the 9th band and highest frequency in the 8th band as functions of the d/Λ. At each d/Λ, the propagation

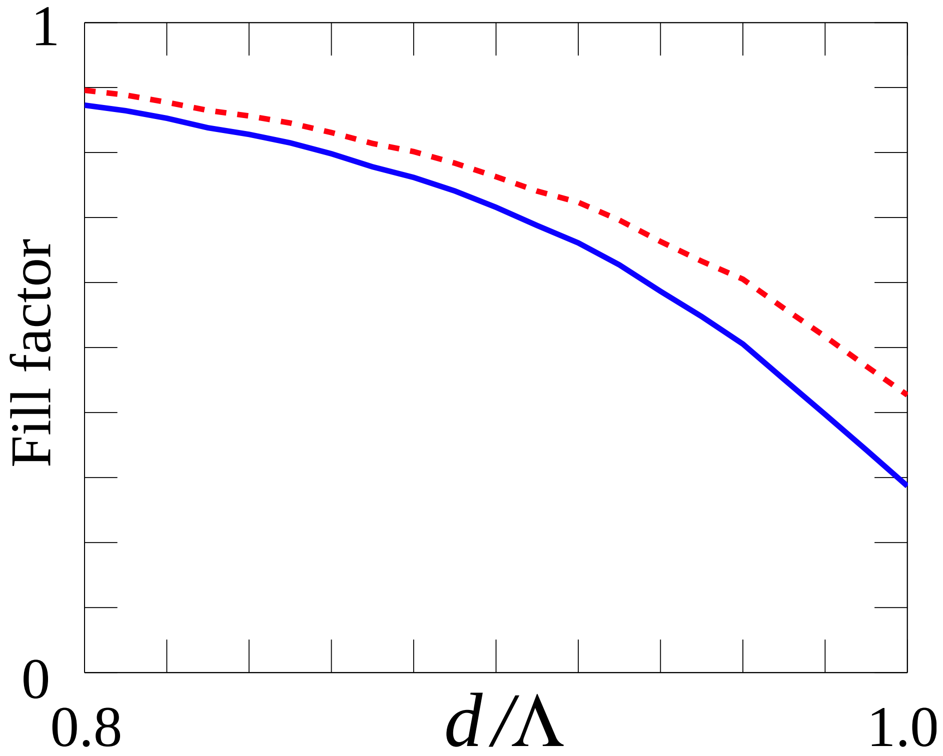

Figure 3.5: Fill factor as a function of the d/Λ. Red dashed and blue solid curves represent the fill factor for the 4th and 5th bands, respectively.

constant is chosen so that the extrema of the 8th and 9th bands cross the air line. Note that the red solid curve is nearly linear, while the red dashed curve is concave. The blue solid curve represents the relative bandgap in percentage, which is the ratio of the difference and the average of the two red curves. Note that blue curve has a maximum at d/Λ of 0.78. In Fig. 3.7(b), the red dashed curve is the same as in Fig. 3.7(a). Three solid blue curves represent the normalized frequency in the Γ, M, and M-K points as functions of the d/Λ. The extremum of the 8th band is located at the M-K point when the d/Λ is small. As the d/Λ increases, the frequency at the Γ point increases faster than it does at the M-K point, and the band extremum shifts to the Γ point when the d/Λ is between 0.77 and 0.78. As a consequence, the dashed curve is concave. A similar transition occurs when we fix the d/Λ at 0.8 and vary the

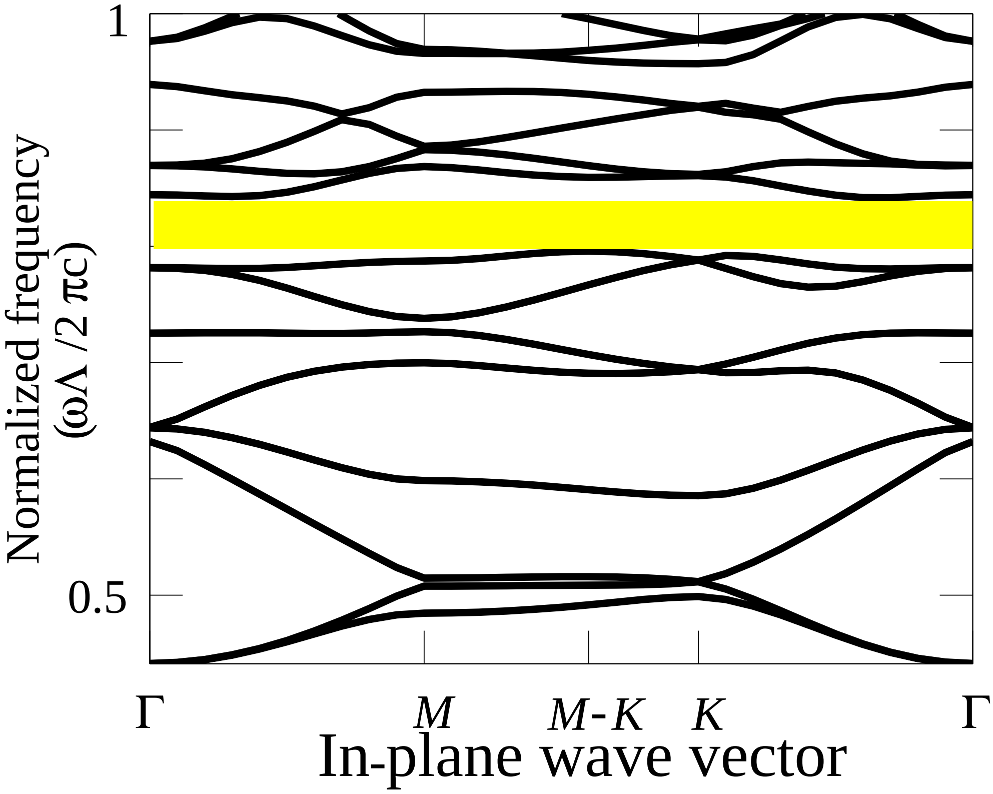

Figure 3.6: Band diagram when we use a refractive index of 2.4 and an d/Λ of 0.75. Yellow indicates the largest relative bandgap.

refractive index. Hence, the relative maximum bandgap has a peak, as shown in the center of the Fig. 3.2. This peak is less steep than the peak at the left upper corner of Fig. 3.2.

3.2 Mode leakage loss analysis

Next, we show the leakage loss for this fiber design near the center of the lowest bandgap using the multipole method [35], [36]. We used a maximum order $M_{\max} = 6$ in the multipole expansion for the cladding holes and $M_{\max} = 10$ in the multipole expansion for the center hole to obtain n_{eff}, the loss, and the mode intensity, and we verified that using $M_{\max} = 7$ for the cladding holes and 11 for the center hole

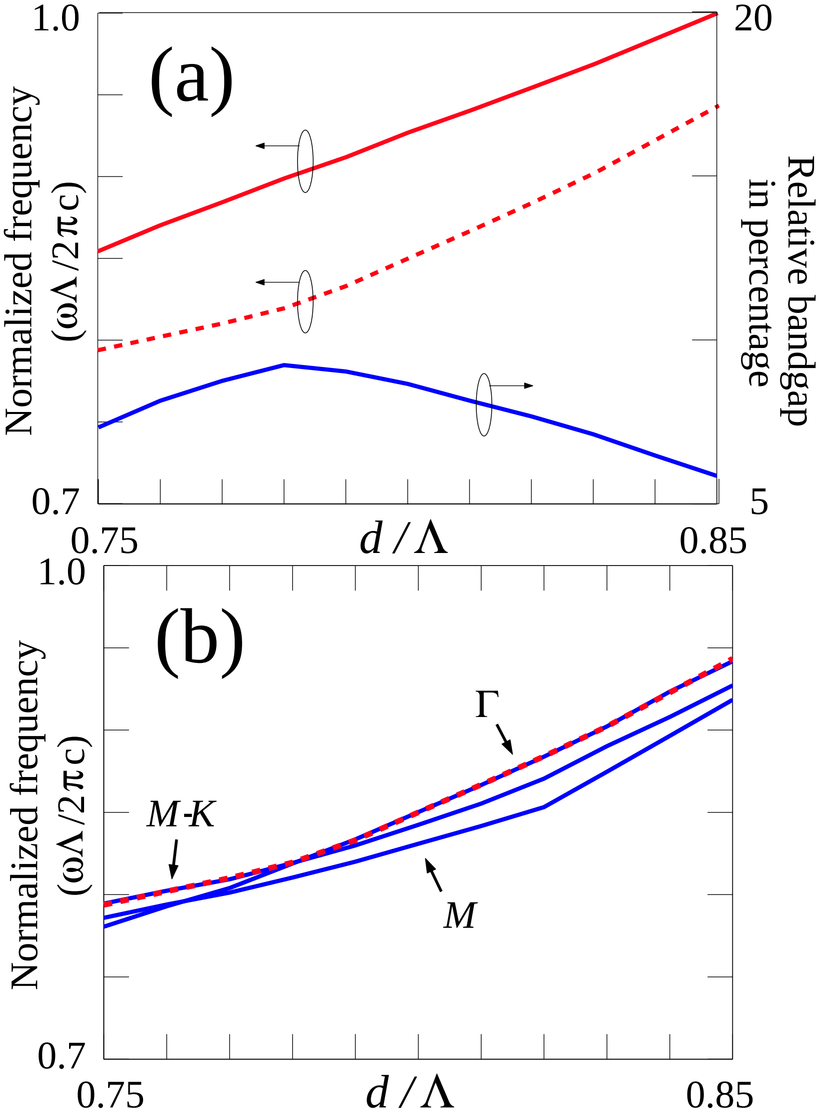

Figure 3.7: (a) Red solid and dashed curves represent the lowest frequency in the 9th band and highest frequency in the 8th band as functions of the d/Λ. (b) The red dashed curve is the same as in (a). Three solid blue curves represent the normalized frequency in the Γ, M, and M-K points as a function of d/Λ.

yields the same n_{eff} to within 0.1% in all the simulations we used in this chapter. The variation of the loss is larger, but it is not visible on a logarithmic scale. The glass width between the center air hole and the first layer of air holes is set as small as 0.08Λ in all of our simulations to suppress surface modes [96], [97]. Figure 3.8 shows the frequency dependence of the leakage loss for the air-core PBGFs with 5

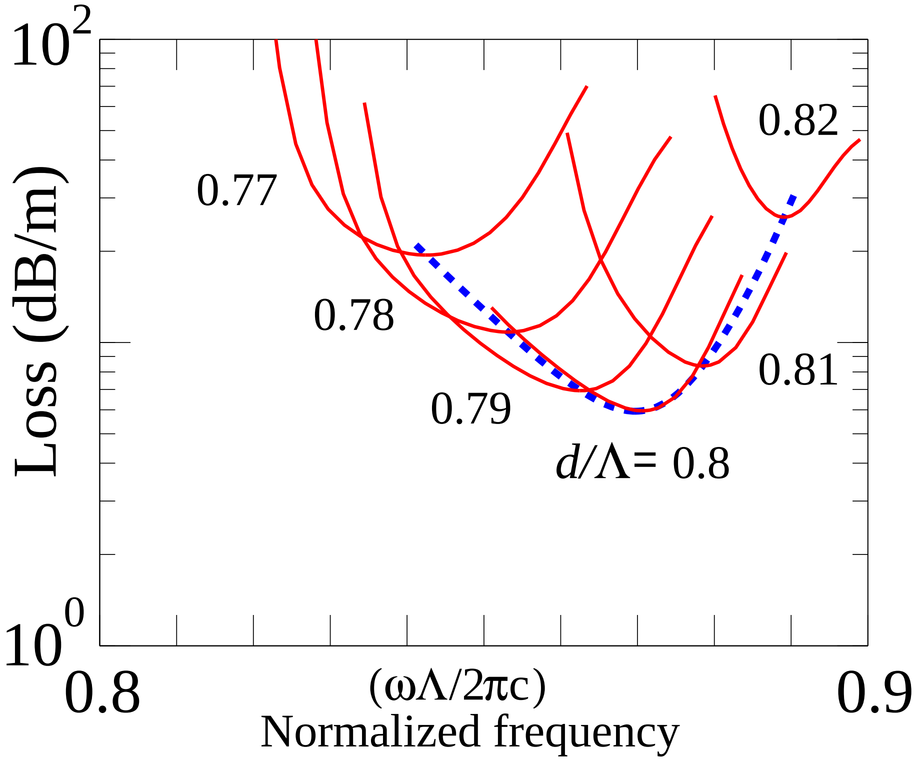

Figure 3.8: The frequency dependence of the leakage loss for air-core PBGFs with 5 rings of air holes, where the d/Λ is taken as a parameter. The dashed curve represents the loss for the optimized normalized frequency with different d/Λ. We recall that normalized frequency $\omega\Lambda/2\pi c$ equals the pitch-wavelength ratio Λ/λ. Loss is calculated by using a wavelength of 4 μm and a refractive index of 2.4.

rings of air holes, where d/Λ is taken as a parameter. The leakage loss is calculated as Loss $= 40\pi\Im(n_{\text{eff}})/[\ln(10)\lambda]$, where $\Im(n_{\text{eff}})$ and λ are the imaginary part of the effective index and the wavelength in meters, respectively [35]. We also plot the loss for optimized normalized frequency with different d/Λ in this figure as a dashed curve, which connects all the minima of the solid curves. The dashed curves in Fig. 3.8 show that there is a minimum loss with a d/Λ of 0.8 and a normalized frequency of 0.87. One must optimize both the d/Λ and the normalized frequency in order to obtain the minimum loss.

We calculated the minimum loss as a function of the refractive index after we

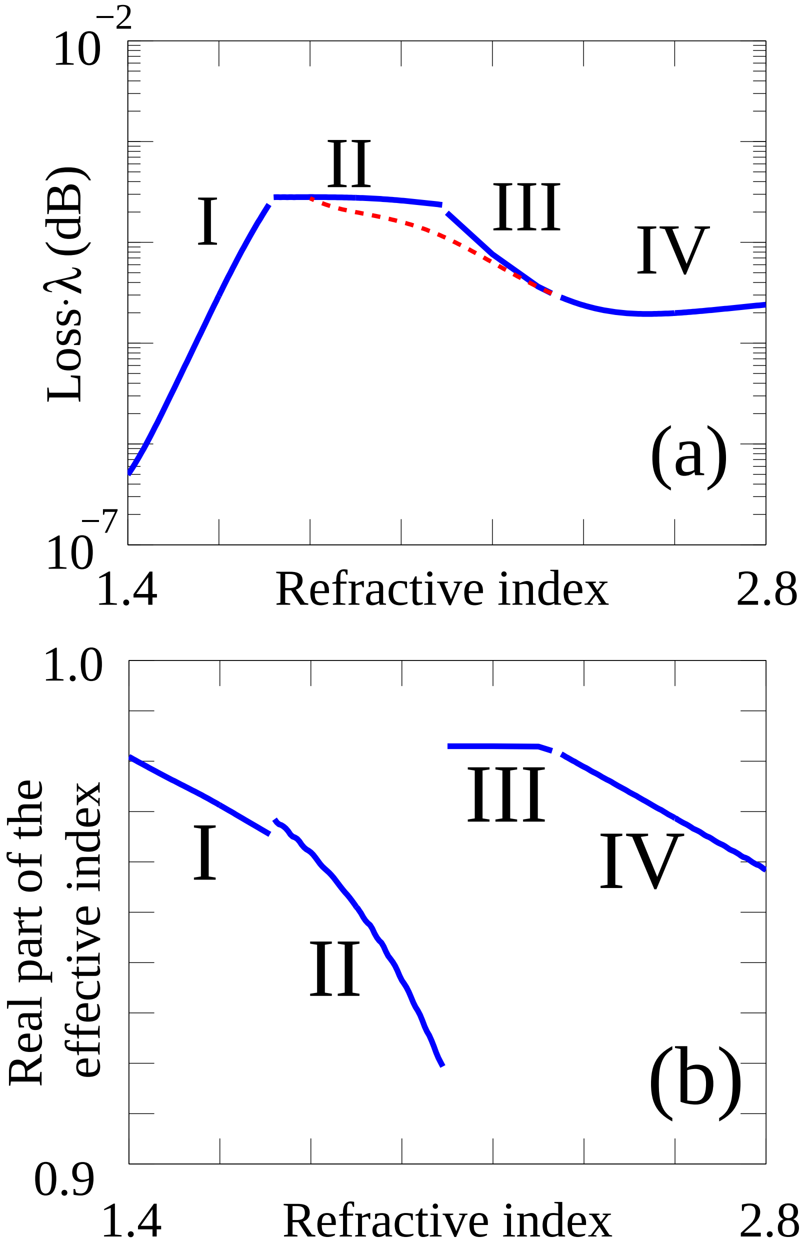

Figure 3.9: (a) The normalized leakage loss (loss × wavelength) as a function of refractive index. (b) The corresponding real part of the effective index.

optimized both the d/Λ and the normalized frequency for a refractive index between 1.4 and 2.8. Figure 3.9(a) shows the normalized minimum loss as a function of the refractive index. There are four curves in Fig. 3.9(a). The modes in curve I are

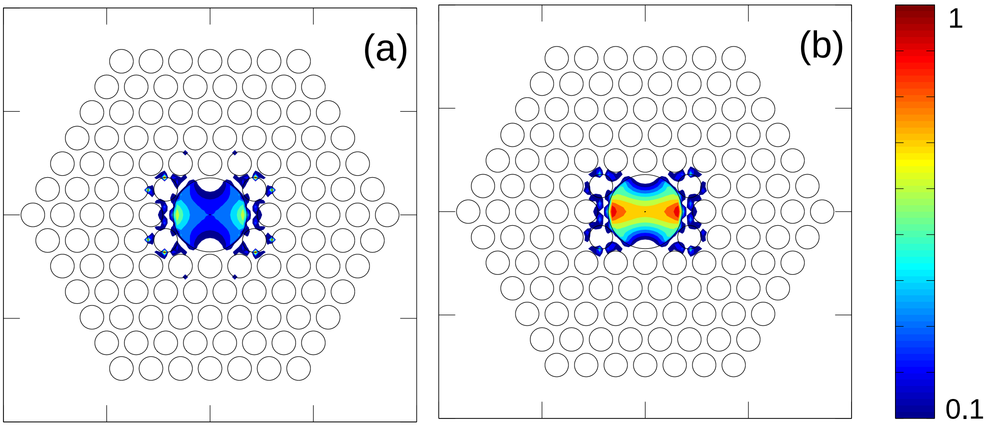

Figure 3.10: Geometry and corresponding normalized mode intensity for a 5-layer air-guided PBGF corresponding to (a) the mode found by our optimization procedure without any constraints and (b) the mode found by our optimization procedure with the constraint that more than 75% of the mode power is located in the central air core. A normalized mode intensity smaller than 0.1 is not shown.

located at the bandgap between the 4th and 5th bands. The modes in curves II, III, and IV are located at the bandgap between the 8th and 9th bands. The real part of the effective index is shown in Fig. 3.9(b). As the real part of the effective index approaches the left-hand side of curve IV, the modes become surface-like. In the range of refractive indices in curve III, the search procedure to find the minimum loss finds the mode at the avoided crossing in the middle of the core mode line. Because we only account for leakage loss, the surface-like mode here has a lower loss than the core mode in this case. However, in practice this mode will couple to extended modes and have a high loss [22], so that the calculated low loss is not realistic. In order to avoid finding the surface-like mode in the search procedure, we constrain the modes that come from the search procedure to have 75% or more of its mode power in the central air core. With this constraint, we obtain curve III in Fig. 3.9(a). The red dashed curve in Fig. 3.9(a) is the result from the optimization without any constraints. Figures 3.10(a) and (b) show the geometry and the corresponding mode intensity,

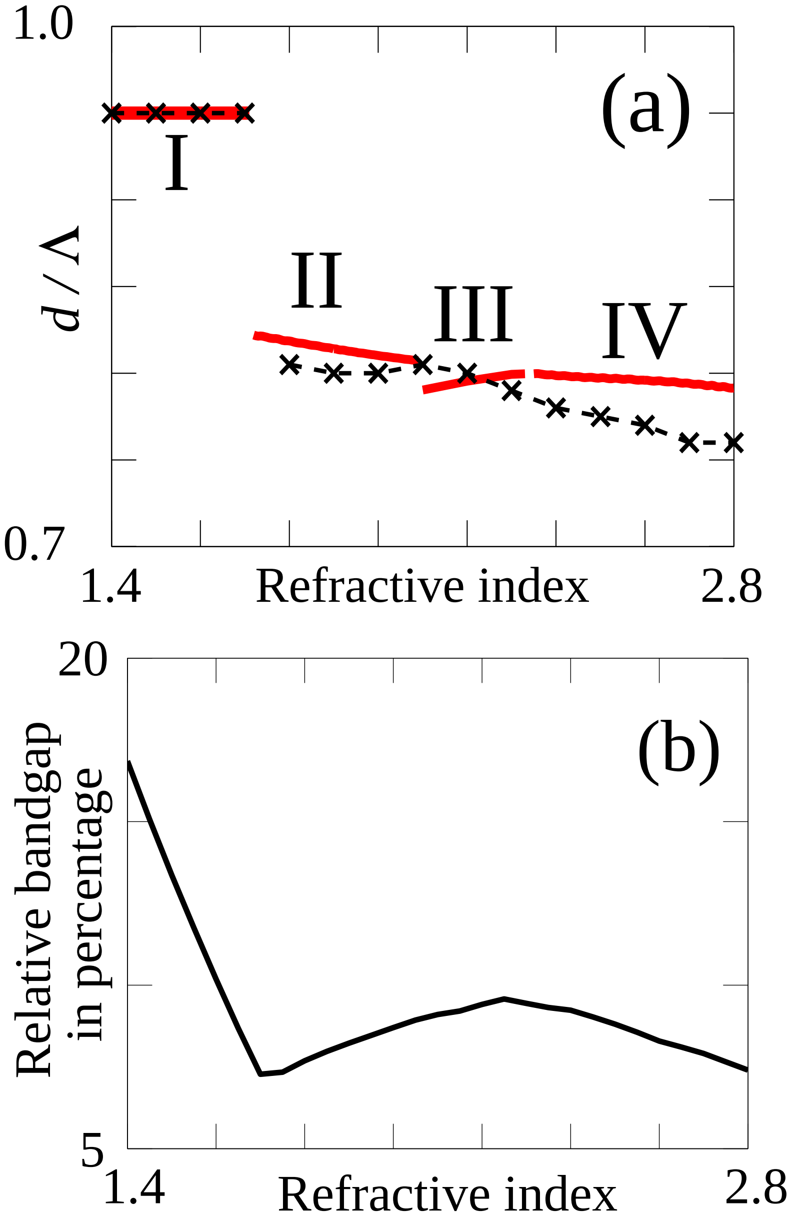

Figure 3.11: (a) The solid curves represent the d/Λ corresponding to minimum loss. The dashed curves with x-marks represent the d/Λ corresponding to the maximum relative bandgap. (b) Relative bandgap when the d/Λ corresponds to the dashed curve of (a).

normalized to its peak, with a refractive index of 2.2 found by the search procedure without any constraints and found by the search procedure with constraint that more than 75% of the mode power is located in the central air core. In Figs. 3.10(a) and (b), the black circles represent the hole boundaries and the color contour plots represent the Poynting flux. The leakage losses calculated by the multipole method corresponding to Figs. 3.10(a) and (b) are 16 and 19 dB/m with a wavelength of 4 μm, respectively. Hereafter, we will refer to curve III, in which this constraint is obeyed, as the minimum loss curve, since the loss figures for the surface-like modes are not realistic in practice [22]. We plot the d/Λ corresponding to the minimum loss as the red solid curve in Fig. 3.11(a). The black dashed curves represent the d/Λ corresponding to the largest relative bandgap for each refractive index, which is the same as the black dashed curves in Fig. 3.2. The maximum difference between the d/Λ corresponding to the maximum relative bandgap and the minimum loss is about 0.03. Figure 3.11(b) shows the relative bandgap when the d/Λ corresponds to the dashed curve of Fig. 3.11(a), which is the maximum possible relative bandgap at each refractive index. The trends in Fig. 3.11(b) are the opposite of those in Fig. 3.9(a). When the relative bandgap decreases, the loss increases, and vice versa. The refractive index of 2.6, corresponding to the minimum loss, is higher than the refractive index of 2.2, corresponding to the maximum relative bandgap. The reason for this difference is that the higher refractive index contrast between the air and the glass helps to confine the mode in the center air hole. Hence, the refractive index corresponding to the minimum loss is somewhat higher.

Figure 3.12 shows the optimized normalized frequency corresponding to the curves in Fig. 3.9 as a function of refractive index. Note that the optimized normalized frequency decreases as the refractive index increases. The reason is that the field in a material with a higher refractive index will have a lower frequency than the field with a lower refractive index, assuming that the geometry and the propagation constant

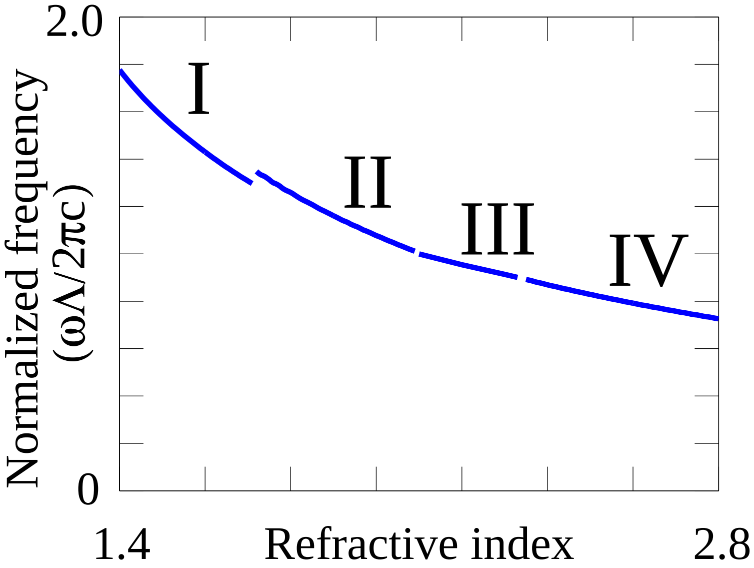

Figure 3.12: The optimized normalized frequency corresponding to curves in Fig. 3.9 as a function of refractive index.

are fixed. The normalized frequency that we showed in Fig. 3.1 will decrease as the refractive index increases at a fixed propagation constant. Hence, the optimized normalized frequency decreases as the refractive index increases. The slight offset between curves I and II comes from the different bandgaps we discussed in Chapter 3.1. The optimized normalized frequency shown in Fig. 3.12 will be useful in the practical design of the air-guided PBGF.

Figure 3.13 shows the geometry and the corresponding mode intensity, normalized to its peak, for a 5-layer air-core PBGF using an refractive index of 2.6, a d/Λ of 0.8 and a normalized frequency of 0.79 corresponding to the minimum shown in the curve IV in Fig. 3.9(a). The black circles represent the hole boundaries and the color contour plots represent the Poynting flux. Figure 3.14 shows the loss as a function of the number of air hole rings on a logarithmic scale with the same fiber parameter. Note that the loss is less than 1 dB/km with 9 air hole rings and a wavelength of

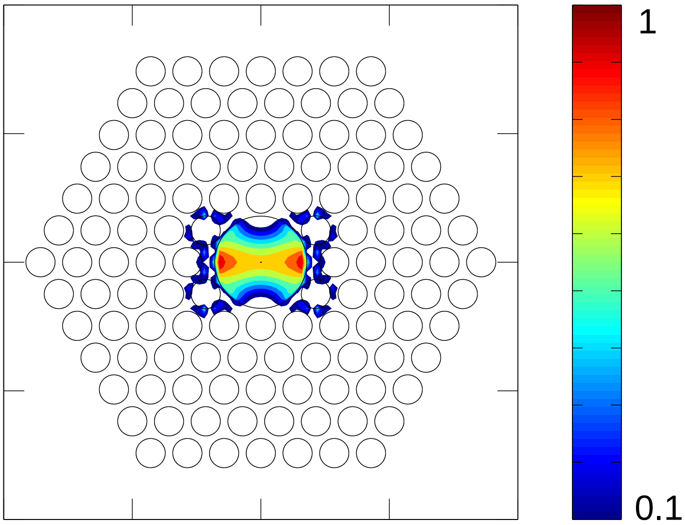

Figure 3.13: (a) Geometry and corresponding normalized mode intensity for a 5-layer air-guided PBGF corresponding to the minima shown in the dashed curves in Fig. 3.9. A normalized mode intensity smaller than 0.1 is not shown.

4 μm. This loss is lower than what can be obtained with 14 air hole rings with a d/Λ of 0.9 for silica material with a refractive index of 1.45, as shown in Fig. 6 of Ref. 20. We have also carried out the optimization procedure with 6 and 7 air hole rings, and we find that the optimized d/Λ and normalized frequency corresponding to minimum loss vary by 1% and 2%, respectively.

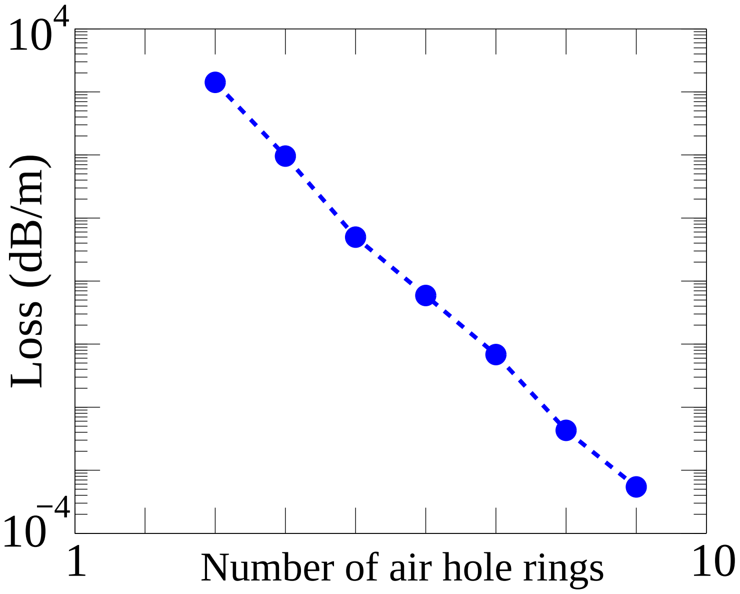

Figure 3.14: The loss as a function of the number of air hole rings on a logarithmic scale with the same fiber parameter.

Chapter 4

Optimization of the operational bandwidth in air-core photonic bandgap fibers

Air-core photonic bandgap fibers (PBGFs), in contrast to some other types of holey fiber, guide light through the photonic bandgap effect, instead of using total internal reflection [10]. These air-core PBGFs have the potential to provide very low-loss transmission, along with delivery of high-powers and low nonlinearity. Surface modes, which are located between the core and cladding, have been shown to have a significant impact on the loss of the fundamental mode [22], [98]. Amezcua-Correa, *et al.* [23], [24] demonstrated that by carefully selecting the thickness of the inner glass ring around the core, it is possible to push the surface modes away from the center of the bandgap in silica PBGFs. Laser-power delivery in infrared (IR) region through optical fibers has important military and medical applications [15], [17]. Pearce, *et al.* [97] showed that a PBGF with a 19-cell core and a glass refractive index of 2.4 has an operational bandwidth of 5% of the center frequency with an inner glass ring thickness of 0.05Λ, where the pitch, Λ, is defined as the distance between the centers of the nearby holes. However, this result does not indicate what parameter choice optimizes the bandwidth. In this chapter, we study the operational bandwidth as a function of inner glass ring thickness for PBGFs with different refractive indices for the glasses used for IR transmission. We analyze fibers with both a 19-cell and a 7-cell core. These geometries were previous studied experimentally [23], [97]. The optimum inner glass ring thickness that yields the widest operational bandwidth is 0.04Λ. The operational bandwidth increases when the refractive index decreases from 2.8 to 2.0, which is slightly larger than the range of possible values for chalcogenide glass used for IR transmission [15].

4.1 Fiber geometry

We calculate the fiber modes and their propagation constants using Comsol Multiphysics, a commercial full-vector mode solver based on the finite-element method. Anisotropic perfectly-matched layers (PMLs) [20] are positioned outside the outermost ring of holes in order to reduce the simulation window for a PBGF with five air-hole rings. To validate our simulations, we compared our results to the Fig. 3 of Ref. 23, and we obtained agreement. Figure 4.1 shows the fiber core geometries for two air-core PBGFs. The core is created by introducing a larger air hole at the center of the fiber. Only a quarter of the geometry is used in modeling PBGFs because of the symmetry of the fundamental core mode. Figures 4.1(a) and (b) correspond to a 19-cell and 7-cell core, meaning that 19 and 7 air holes have been removed respectively to form the core before the drawing process. In this study we use $D/\Lambda = 0.8$ for both 19-cell and 7-cell cores, which has been shown to yield a wide bandgap for high index glass [86]. In Fig. 4.1(a), the corner of the inner glass ring is rounded with radius d_p, where $d_p/\Lambda = 0.5$. In Fig. 4.1(b), we use $d_p/\Lambda = 0.2$. The corner of the core region is rounded with radius d_c, where $d_c/\Lambda = 0.94$.

4.2 Result and analysis

When there is no coupling loss due to surface modes, the overall attenuation is dominated by scattering loss due to surface roughness. This loss factor F can be estimated from the field intensity at the air-glass interfaces as [99]

$$F = \left(\frac{\epsilon_0}{\mu_0}\right)^{1/2} \frac{\oint_{\text{hole perimeters}} dl|\mathbf{E}|^2}{|\int_{\text{cross-section}} dA(\mathbf{E} \times \mathbf{H}^*) \cdot \hat{\mathbf{z}}|}, \tag{4.1}$$

where ϵ_0 and μ_0 are the vacuum permittivity and permeability, respectively, while **E** and **H** denote the electric and magnetic field. In the numerator, the **E**-field is evaluated along the path just inside each hole interface. Figure 4.2 shows the power in the core as a percentage of the total power and the normalized loss factor $F \cdot \Lambda$. As the normalized ring thickness t/Λ increases, the number of surface modes also increases. When t/Λ is larger than 0.08, the increase in the number of surface modes leads to a decrease in the operational bandwidth. In Fig. 4.2(a), we use red to indicate the parameter range where the fundamental core mode has more than 90% of power located in the core. Yellow indicates avoided crossings due to the surface modes [22]. Blue indicates the parameter range where the fundamental mode is no longer confined in the core. Note that Figs. 4.2(a) and (b) are highly correlated. In Fig. 4.3(a), we show the mode effective index as a function of normalized frequency at a normalized ring thickness of 0.05. The blue solid and dashed curves represent the fundamental air-guided mode and surface modes, respectively. The black dashed lines represent the edge of the bandgap, calculated by the full-vectorial plane-wave

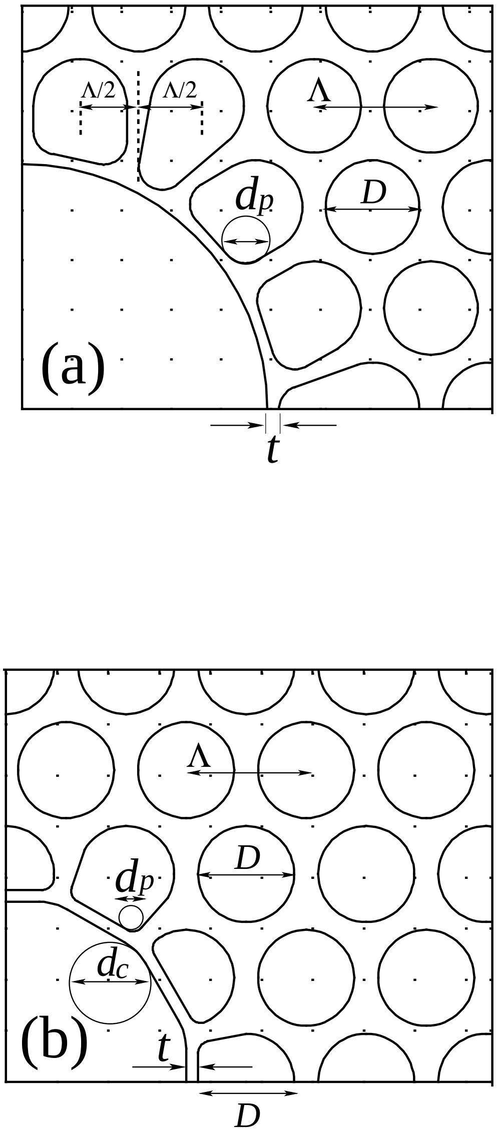
Λ/2
Λ/2
Λ
d_p
D
(a)
t
Λ
D
d_p
d_c
(b)
t
D

Figure 4.1: Fiber geometries for PBGFs with (a) a 19-cell core and (b) a 7-cell core.

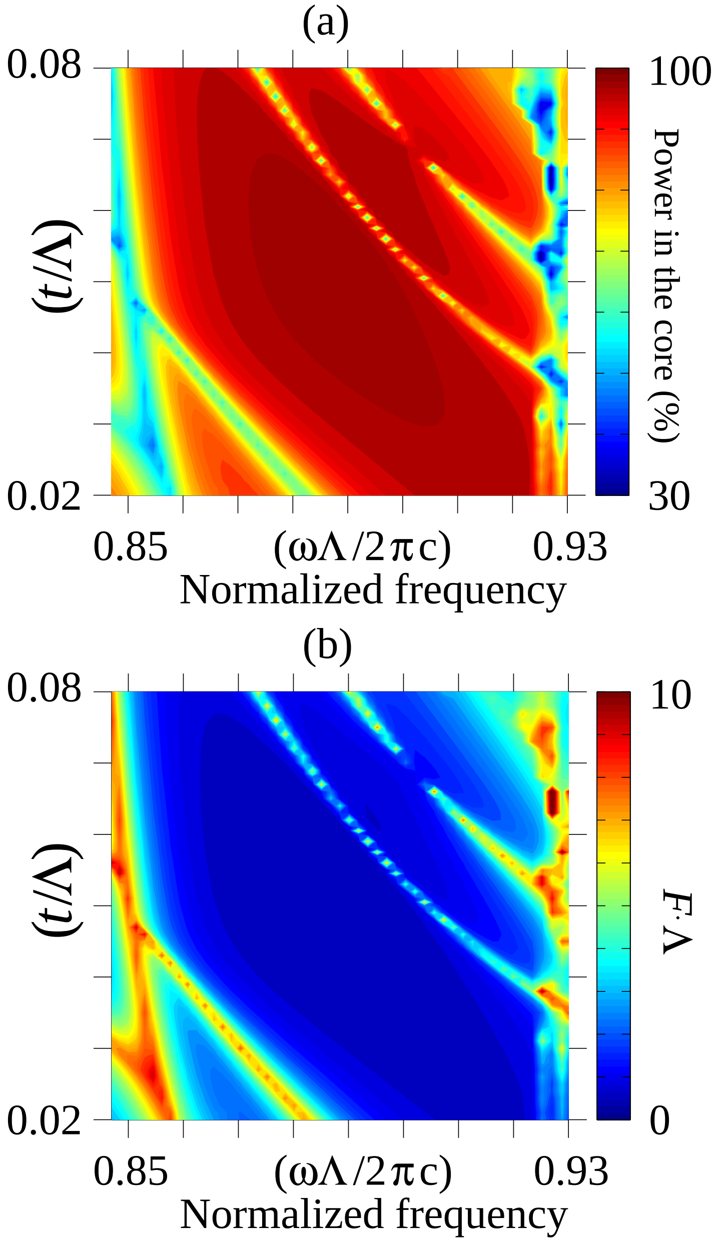

Figure 4.2: Contour plots of (a) power in the core and (b) $F \cdot \Lambda$ for a PBGF with a 19-cell core.

method [38]. This fiber has an avoided crossing between the fundamental mode and a surface mode within the bandgap at a normalized frequency of 0.9. Away from the avoided crossing point, most of the optical power of the fundamental mode is localized in the core region, as shown in mode (I). The surface mode (III) has most of its power confined in the glass region between core and cladding. At a frequency near the avoided crossing, the mode shown in (II) cannot be unambiguously identified as either a core mode or a surface mode, since the power is distributed in both the core and surface regions. In Fig. 4.3(b), we show both power in the core and the normalized loss factor $F \cdot \Lambda$. These two quantities are inversely related. We obtain the optimal normalized ring thickness that yields the widest possible operational bandwidth when $F \cdot \Lambda = 1.6$. The optimal bandwidth is insensitive to the threshold value of 1.6 for $F \cdot \Lambda$, as is apparent in Fig. 4.3. The power in the core is more than 90% of the total power in this case. We define the relative operational bandwidth as the ratio of the widest operational bandwidth to the center frequency. Figure 4.4 shows the relative operational bandwidth as a function of normalized ring thickness with glass refractive indices of 2.2, 2.3, 2.4, and 2.5. Note that the optimal normalized ring thickness is 0.04, which yields a relative operational bandwidth of nearly 6% for a refractive index of 2.4. Figure 4.5 shows that the relative operational bandwidth as a function of refractive index at a ring thickness of 0.04. The relative operational bandwidth increases as the refractive index decreases from 2.8 to 2.0.

In Fig. 4.6, we present the power in the core and the normalized loss factor $F \cdot \Lambda$ for a PBGF with a 7-cell core and a glass refractive index of 2.4. In this case, when the normalized ring thickness is less than 0.05, the relative operational bandwidth increases as the normalized ring thickness decreases. The relative operational band-

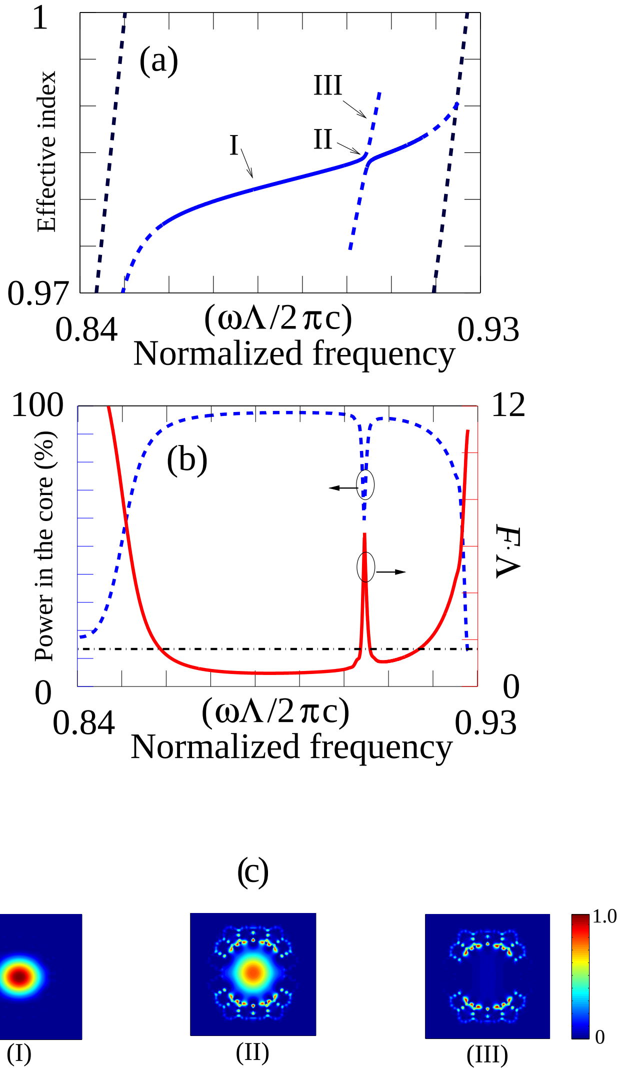

Figure 4.3: (a) The mode effective index as a function of normalized frequency at a normalized ring thickness of 0.05. The blue solid and dashed curves represent the fundamental air-guided mode and surface modes, respectively. The black dashed lines represent the edge of the bandgap. (b) The comparison between power in the core and normalized factor $F \cdot \Lambda$ for a PBGF with a 19-cell core. Black dash-dotted line indicates $F \cdot \Lambda = 1.6$. (c) The relative mode intensity profiles correspond to points I, II, and III in (a).

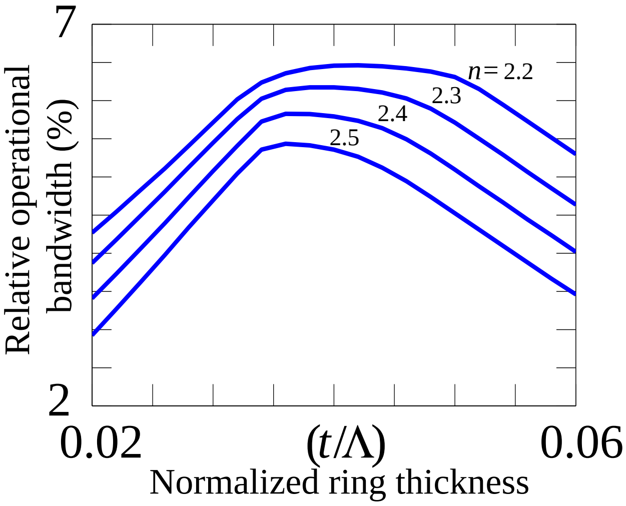

Figure 4.4: Relative operational bandwidth as a function of normalized ring thickness.

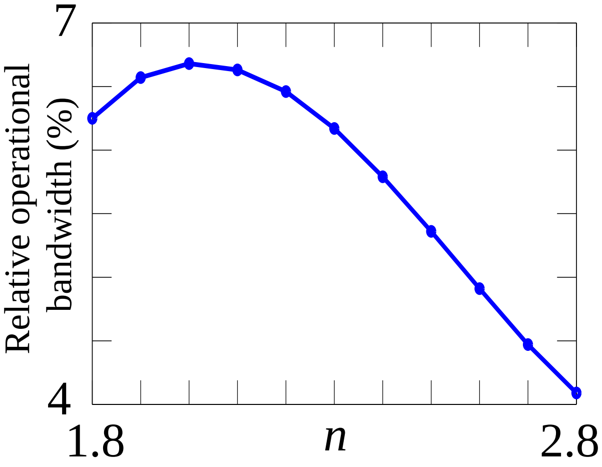

Figure 4.5: The relative operational bandwidth for different glass refractive indices with a normalized ring thickness of 0.04.

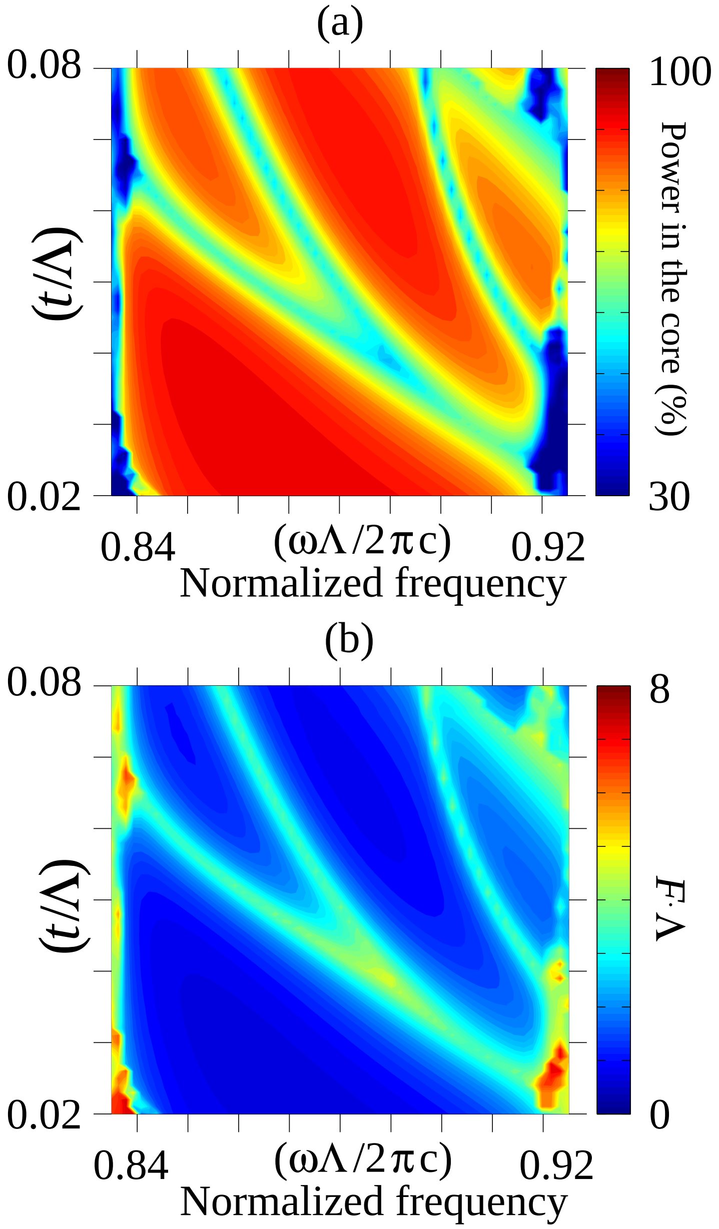

Figure 4.6: Contour plots of (a) power in the core and (b) $F \cdot \Lambda$ for a PBGF with a 7-cell core.

width is higher than 6% when the normalized ring thickness is less than 0.03. Such a small ring thickness may be difficult to draw in practice.

Chapter 5

Raman response function and supercontinuum generation in chalcogenide fiber

Supercontinuum generation uses the Kerr effect and the Raman effect in optical fibers to broaden the bandwidth of an optical signal, and it has numerous applications to spectroscopy, pulse compression, and the design of tunable ultrafast femto second laser sources [100]. Most investigations to date have used silica fibers. The longest wavelength that can be generated in silica fibers is below 2 μm, because the wavelength is limited by the material loss of the fiber. Supercontinuum generation beyond this wavelength requires fibers with longer infrared (IR) transmission windows. Price, *et al.* [101] have shown theoretically that it is possible to generate an IR supercontinuum from 2 to 5 μm using a bismuth-glass PCF with the same structure. Domachuk, *et al.* [102] have experimentally generated a mid-IR supercontinuum with a spectral range of 0.8 to 4.9 μm using a tellurite PCF with the same structure. However, the light generated above 2 μm is very limited. Shaw, *et al.* have reported experimental work that demonstrates supercontinuum generation from 2.1 to 3.2 μm in an As_2Se_3-based chalcogenide PCF with one ring of air holes in a hexagonal structure [26]. In this paper, we report a detailed investigation of supercontinuum generation using an As-Se based chalcogenide PCF in a hexagonal structure. We present the experimentally measured Raman spectrum, which is proportional to the imaginary part of third-order nonlinear susceptibility. We then calculated the real part of the third-order nonlinear susceptibility using the Kramers-Kronig relations [103] and from the total susceptibility, we calculate the time-domain Raman response function. Using the total nonlinear time-domain response function of the chalcogenide fiber, which includes both the instantaneous (Kerr) response and the delayed (Raman) response, we are able to theoretically reproduce the experimentally-measured bandwidth [26] of the supercontinuum generation. This result shows that the measured nonlinear response of the chalcogenide fiber can completely account for the supercontinuum generation. We then theoretically find a relatively flat bandwidth of more than 4 μm, in which roughly the same maximum power is obtained over the entire bandwidth, can be generated using an endlessly single-mode As_2Se_3-based chalcogenide PCF with an air hole diameter to pitch value of 0.4 and a pitch value of 3 μm. Compared to tellurite glass, chalcogenide glass has a larger refractive index and a higher nonlinear index, leading to a greater modal confinement and a higher nonlinearity.

5.1 Raman response function for chalcogenide fiber

We solve the generalized nonlinear Schrödinger equation (GNLS) [100]:

$$\begin{aligned} \frac{\partial A(z,t)}{\partial z} + \frac{a}{2}A - i\mathrm{IFT}\{[\beta(\omega_0+\Omega) - \beta(\omega_0) - \Omega\beta(\omega_0)]\tilde{A}(z,\Omega)\} \\ = i\gamma\left(1+\frac{i}{\omega_0}\frac{\partial}{\partial t}\right)\left[A(z,t)\int_{-\infty}^{t} R(t')|A(z,t-t')|^2 dt'\right], \end{aligned} \tag{5.1}$$

where $A(z,t)$ is the electric field envelope. IFT$\{\}$ denotes the inverse Fourier transform. $\gamma = n_2\omega_0/(cA_{\mathrm{eff}})$ is the nonlinear coefficient, n_2 is the nonlinear refractive index, a is fiber loss, and A_{eff} is the fiber's effective area. We use the full dispersion curve. It is equivalent to expanding the dispersion relation in a Taylor series when the series converges. While one often writes the GNLS with a Taylor series, this calculation is usually done in practice using the inverse Fourier transform unless the Taylor series only has a small number of terms, like 2 or 3. The nonlinear response function $R(t) = (1 - f_R)\delta(t) + f_R h_R(t)$ includes both the Kerr $\delta(t)$ and Raman $h_R(t)$ contributions [103]. Figure 5.1(a) shows the normalized imaginary part of the third-order susceptibility N'', which is proportional to the Raman gain. The blue solid curve and the red dashed curve represent the measured Raman gain in a chalcogenide fiber [18] and the Raman gain in a silica fiber [103], respectively. Figure 5.1(b) shows the real part of the third-order susceptibility N' in the same arbitrary units, which is obtained from a Kramers-Kronig (Hilbert) transformation of N'' [103]. The Raman response function, shown in Fig. 5.2, may be obtained from either the real part or the imaginary part of the third-order susceptibility since they have even and odd symmetry, respectively [103]. Note that $\int_0^\infty h_R(t)dt = 1$ [103]. The Raman gain for silica fiber has a peak at around 440 cm^{-1}, and the Raman gain for chalcogenide fiber has a peak at around 230 cm^{-1}. Hence, the response function for chalcogenide fiber has a longer response time than silica fiber, as shown in Fig. 5.2, and the Raman response must be taken into account for pulses as long as a picosecond, in contrast to silica fibers, where the finite time delay may be ignored for pulses that are longer than about 300 fs. The quantity f_R represents the Raman contribution to the nonlinearity. The Raman power gain coefficient g is related to f_R by $g(\Omega) = (2\omega_p/c)n_2 f_R \text{Im}[H_R(\Omega)]$ [103], where ω_p and $\text{Im}[H_R(\Omega)]$ represent the pump frequency and the imaginary part of the Fourier transform of $h_R(t)$, respectively. We then obtain $f_R = 0.1$ for chalcogenide fiber using parameters reported in Ref. 18. The convolution integral in Eq. 5.1 is calculated as a product in the frequency domain.

5.2 Comparison between theory and experiment

Figure 5.3 shows the material dispersion calculated from refractive indices measured at the Naval Research Laboratory for chalcogenide glass and the total dispersion calculated from a chalcogenide PCF with one air-hole ring, respectively. We model a chalcogenide PCF with a core diameter of 10 μm and a hole diameter to pitch ratio of 0.8. The full dispersion curve is used to solve Eq. 5.1. In Fig. 5.4, the blue solid curve and the red dashed curve show the simulation and corresponding experimental spectra [26] with a resolution bandwidth of 1 nm after one meter of chalcogenide PCF. In accordance with the parameters from Ref. 26, the loss is set to 4.8 dB/m, and the input signal has a full width at half maximum of 100 fs, a pulse energy of 100 pJ, and a wavelength of 2.5 μm. For the nonlinear index n_2, we used $n_2 = 1.5 \times 10^{-17}$ m/W at a wavelength of 2.5 μm, which we obtained from Fig. 5 of Ref. 18. The simulation result is in good agreement with experiment. While there are quantitative differences that we attribute to a combination of longitudinal variation of the fiber cross-section, uneven spectral response of the optical spectrum analyzer (OSA), and the wavelength dependent coupling losses into the OSA [104], the simulations accurately reproduce the bandwidth of the supercontinuum in the range of 2.1 to 3.2 μm to within 5%. Accurate reproduction of the bandwidth has been the main goal in simulations of supercontinuum generation [105], [106]. This result shows that the measured nonlinear response of the chalcogenide fiber can completely account for the supercontinuum generation.

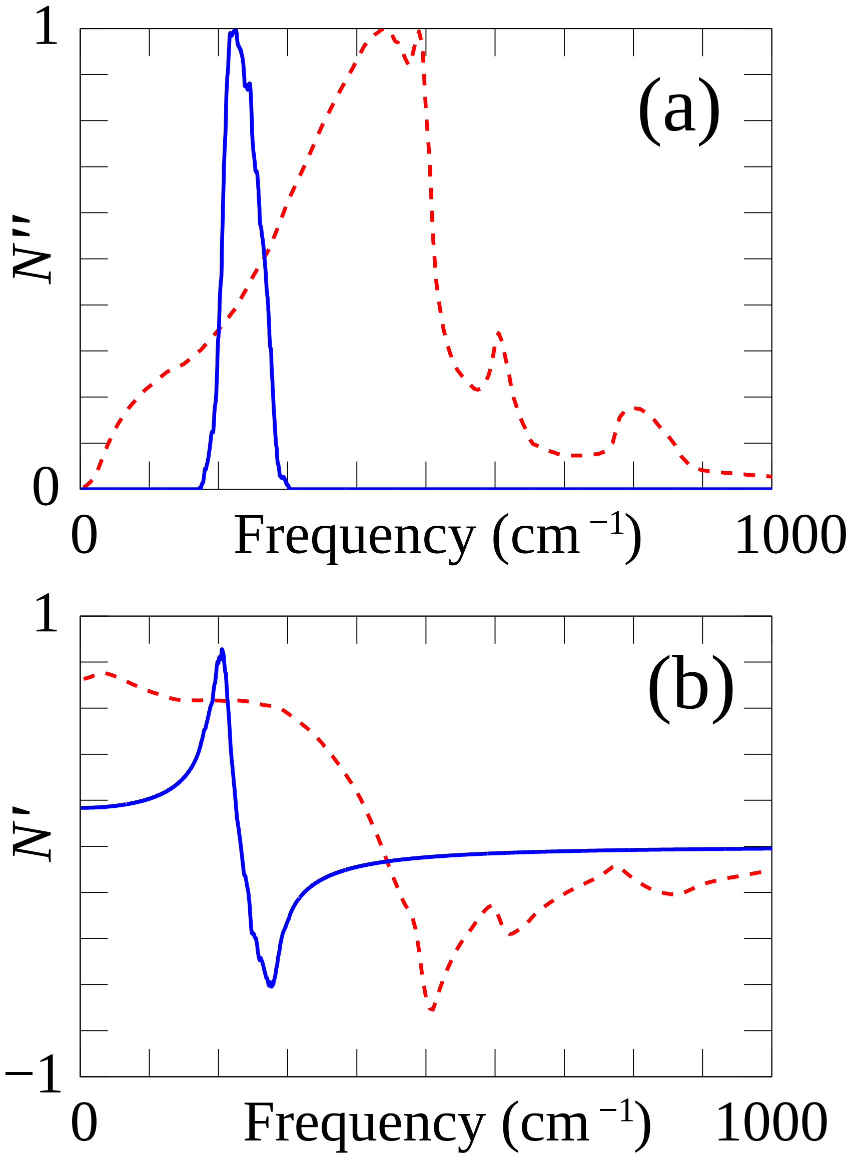

Figure 5.1: (a) The imaginary part of third-order susceptibility, which is proportional to the Raman gain. It has been normalized to unity at the peak gain. (b) The real part of the third-order susceptibility is shown in the same arbitrary units.

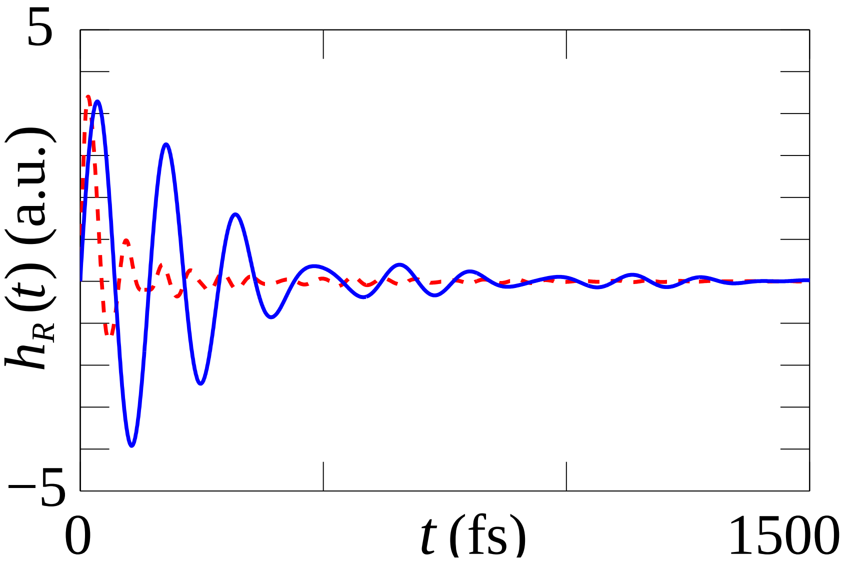

Figure 5.2: Raman response function. In these figures, the blue solid curve and the red dashed curve represent chalcogenide fiber and silica fiber, respectively.

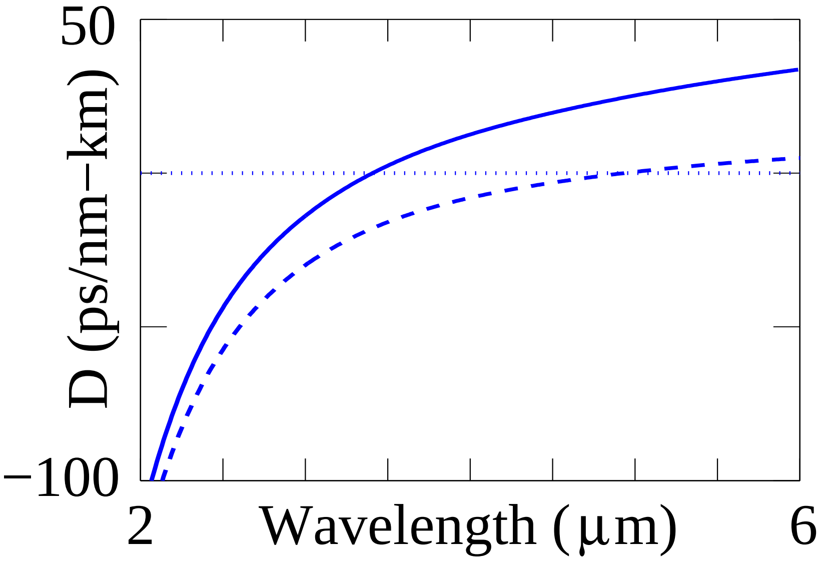

Figure 5.3: (a) The dashed curve and solid curve represent material dispersion for chalcogenide glass and total dispersion for a chalcogenide PCF with one air-hole ring, respectively.

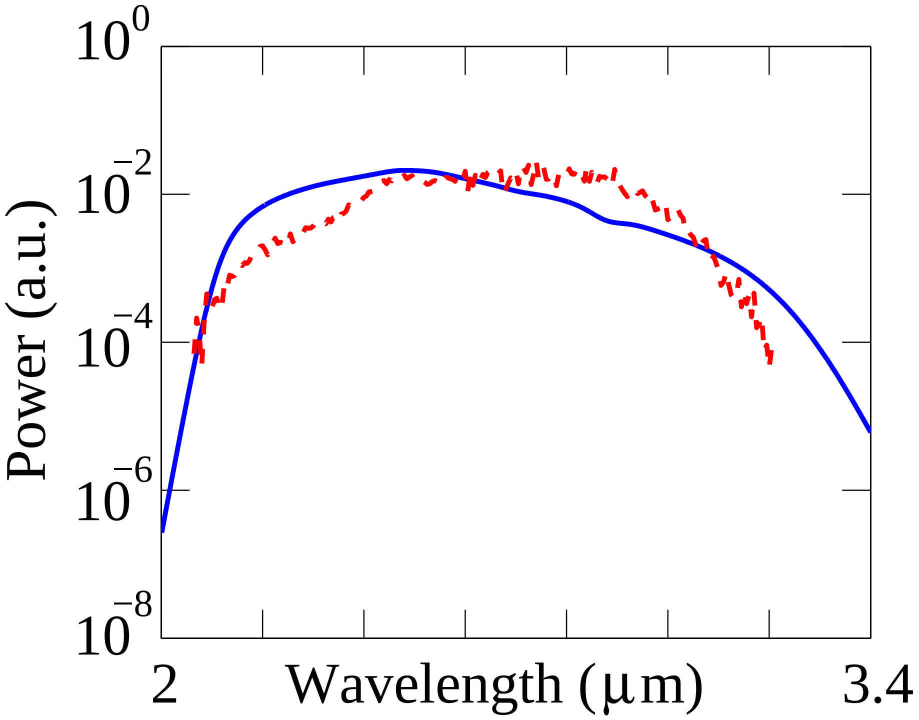

Figure 5.4: The blue solid curve and the red dashed curve show the simulation result and corresponding experimental result [26].

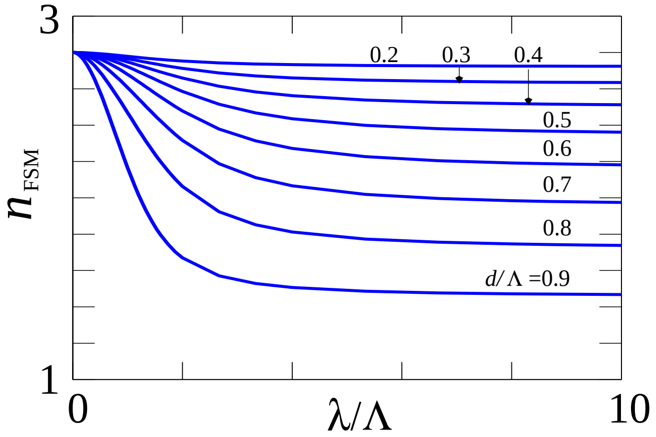

Figure 5.5: The effective index of the fundamental space-filling mode n_{FSM} as a function of the ratio of wavelength to pitch, λ/Λ, with different ratios of hole diameter to pitch, d/Λ.

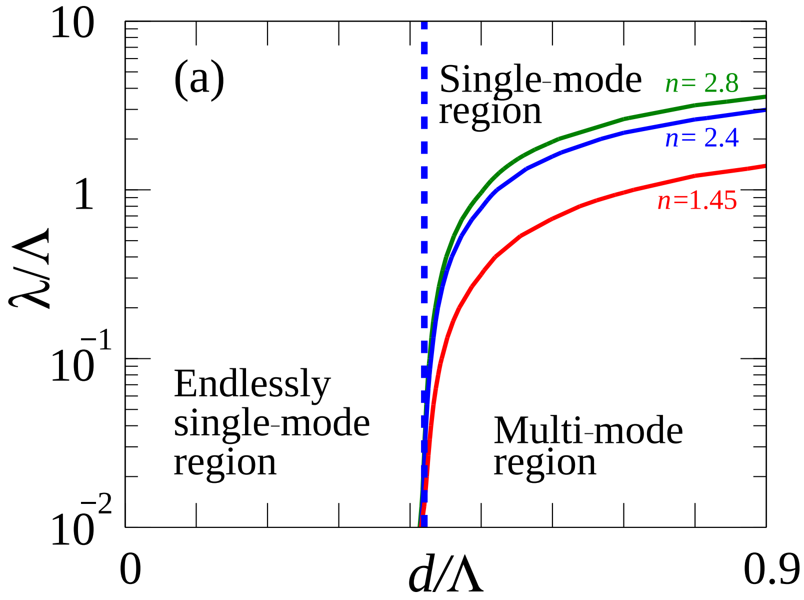

Figure 5.6: The curves corresponding to $V_{\text{eff}} = 2.405$ for different refractive indices of glass. The red, blue, and green solid solid curves represent refractive indices of 1.45, 2.4, and 2.8, respectively.

5.3 Single mode analysis

It has been shown that silica PCFs with some geometries can be single-mode for any wavelength [107]. Here, we want to find the single-mode condition for chalcogenide fiber. The cutoff wavelength of a higher-order mode is determined by using the effective cladding index n_{FSM}. The value n_{FSM} is the effective index of the fundamental space-filling mode (FSM), which is defined as the fundamental mode of the infinite photonic crystal cladding if the core is absent [107]. Figure 5.5 shows n_{FSM} as a function of the ratio of wavelength to pitch, λ/Λ, with different ratios of hole diameter to pitch, d/Λ, calculated by using the full-vectorial plane-wave method [94]. The refractive index of the background glass is set to 2.8, corresponding to the refractive index of As_2Se_3 at a wavelength of 4 μm, and material dispersion is ignored here for simplicity. Note that n_{FSM} strongly depends on both the ratio of wavelength to pitch and the ratio of hole diameter to pitch. In a standard step-index fiber (SIF), the number of guided modes is determined by the V-value [108],

$$V = \frac{2\pi}{\lambda} a (n_{\mathrm{co}}^2 - n_{\mathrm{cl}}^2)^{1/2}, \tag{5.2}$$

where, a, λ, n_{co}, and n_{cl} represent the core radius, wavelength, core index, and cladding index, respectively. The value V must be less than 2.405 for a fiber to have a single mode. The effective V for PCF can be defined by [109]

$$V_{\mathrm{eff}} = \frac{2\pi}{\lambda} a_{\mathrm{eff}} (n_{\mathrm{co}}^2 - n_{\mathrm{FSM}}^2)^{1/2}, \tag{5.3}$$

where a_{eff} is the effective core radius. We use $a_{\mathrm{eff}} = \Lambda/\sqrt{3}$ with the cutoff condition of $V_{\mathrm{eff}} = 2.405$ [109]–[111]. Figure 5.6 shows the curves corresponding to $V_{\mathrm{eff}} = 2.405$ for different refractive indices of glass. The red solid curve represents silica with a refractive index of 1.45, which reproduces the result in Ref. 109. The blue and green solid curves represent refractive indices of 2.4 and 2.8, which correspond to refractive indices of As_2S_3 and As_2Se_3 at a wavelength of 4 μm, respectively. At each index, the parameter values in the area above the curve corresponding to $V_{\mathrm{eff}} = 2.405$ and to the left of the dashed line yield single-mode operation. While the single-mode region and multi-mode region in Fig. 5.6 vary as the refractive index changes, the endlessly single-mode region is almost unchanged at every index. The physical reason is as follows: When λ/Λ is small, we may approximate Eq. 5.3 as

$$V_{\mathrm{eff}} \simeq \frac{2\sqrt{2 n_{\mathrm{co}}}\pi}{\sqrt{3}\lambda/\Lambda} (n_{\mathrm{co}} - n_{\mathrm{FSM}})^{1/2}. \tag{5.4}$$

Using data shown in Fig. 5.5 with small λ/Λ, we find that $n_{\mathrm{co}} - n_{\mathrm{FSM}}$ is proportional to $(\lambda/\Lambda)^2$ and depends on d/Λ exponentially. Hence, V_{eff} in Eq. 5.4 is independent of

λ/Λ at small λ/Λ, which is why the curve corresponding to $V_{\text{eff}} = 2.405$ falls steeply as d/Λ is reduced in Fig. 5.6. Considering that glass typically has a refractive index range of 1.45 and 2.8 [14], the variation of $\sqrt{n_{\text{co}}}$ is small compared to the variation in d/Λ. Hence, PCF becomes endlessly single-mode at nearly the same d/Λ with different refractive indices.

5.4 Supercontinuum generation using four-wave mixing

Next, we consider the effect of supercontinuum generation using four-wave mixing in As_3Se_2-based PCF. In this process, two pump photons at the same frequency generate a Stoke and an anti-Stokes photon. The phase-matching condition is [112], [113]

$$(n_s\omega_s + n_a\omega_a - 2n_p\omega_p)/c + 2(1 - f_R)\gamma(\omega_p)P_p = 0, \tag{5.5}$$

where n_s, n_a, and n_p are effective refractive indices at angular frequency ω_s, ω_a, and ω_p for the Stokes, anti-Stokes, and pump wave, respectively, and P_p is the peak power of the pump. Again, we use the full dispersion curve to calculate phase-matching condition. Figure 5.7 shows the phase-matching diagram calculated for the As_2Se_3-based chalcogenide PCF. The blue solid, dashed, and dotted curves present the phase-matching conditions for peak powers of 1, 0.1, and 0 kW, respectively, with $d/\Lambda = 0.4$ and $\Lambda = 3$ μm. The red dash-dotted curve presents the phase-matching condition for a peak power of 0.1 kW for PCF with $d/\Lambda = 0.4$ and $\Lambda = 2.5$ μm. Note that between the wavelength of 2.5 μm and 3 μm, the wavelength generated by PCF with $\Lambda = 3$ μm is longer than the wavelength generated by PCF with $\Lambda = 2.5$ μm. We consider PCF with $d/\Lambda = 0.4$ in this chapter so that it operates in an endlessly single-mode parameter regime.

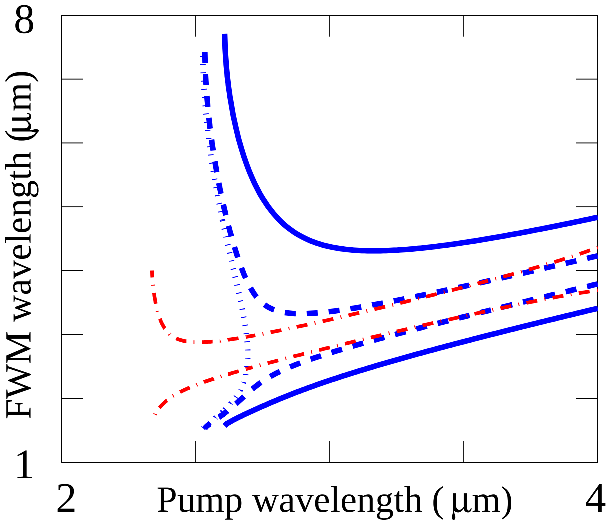

Figure 5.7: The phase-matching diagram is calculated for an As_2Se_3-based chalcogenide PCF. The blue solid, dashed, and dotted curves present the phase-matching conditions for peak powers of 1, 0.1, and 0 kW, respectively, with $d/\Lambda = 0.4$ and $\Lambda = 3$ μm. The red dash-dotted curve presents the phase-matching condition for a peak power of 0.1 kW for PCF with $d/\Lambda = 0.4$ and $\Lambda = 2.5$ μm.

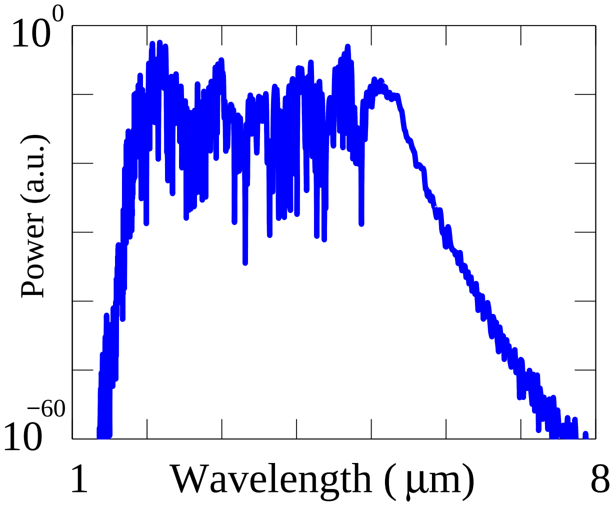

Figure 5.8: The output spectrum using a As_2Se_3-based PCF with $d/\Lambda = 0.4$ and $\Lambda = 3$ μm. The input pulse has a FWHM of 500 fs. The input peak power is set at 1 kW.

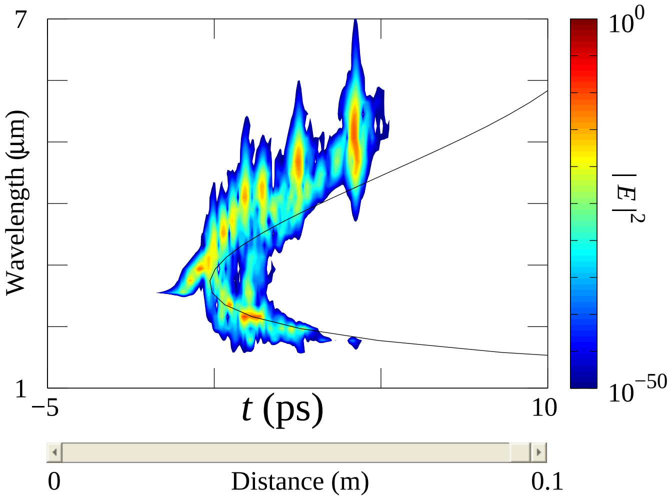

Figure 5.9: Movie of a simulation of the spectrogram as the wave propagates along the PCF. The black solid curve shows the group delay with respect to the wave at 2.5 μm.

We next solve Eq. 5.1 computationally to find an optimized pitch value of PCF that maximizes the supercontinuum generation. Most of the spectral broadening occurs in the first few centimeters. So, when we set the length of the fiber equal to 0.1 meter, we find that a longer fiber length does not increase the supercontinuum bandwidth. The effective area is calculated with different values of the pitch [114]. The loss includes leakage loss and material loss for chalcogenide fiber with low hydrogen impurities [115], which has a low-loss region from 2 μm to about 10 μm. We set the total loss so that the minimum loss is 4.8 dB/m, which is consistent with Ref. 26. Figure 5.8 shows the output spectrum using a As_2Se_3-based PCF with $\Lambda = 3$ μm. The input pulse has a full-width half maximum (FWHM) of 500 fs and peak power of 1 kW. We define a total generated bandwidth as the bandwidth inside frequency limits that are 20 dB down from the peak of the spectrum. The total generated bandwidth is more than 4 μm in Fig. 5.8.

Figure 5.9 shows a movie of a simulation of the spectrogram as the wave propagates

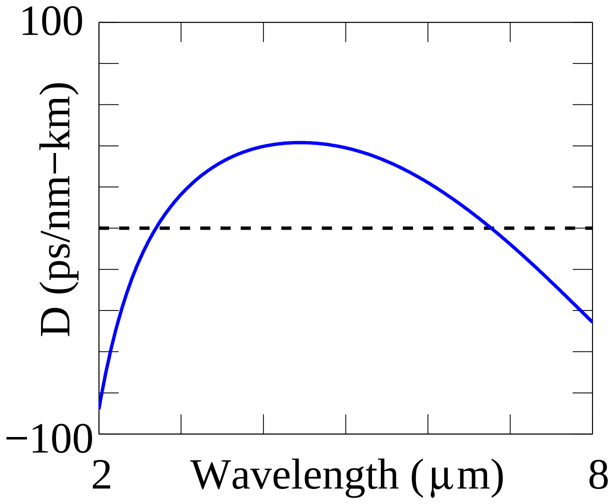

Figure 5.10: The dispersion curve for PCF with $d/\Lambda = 0.4$ and $\Lambda = 3$ μm.

along the PCF. The black solid curve shows the group delay with respect to the wave at 2.5 μm. In the beginning, the effect of self-phase modulation first broadens the spectrum into the region around 2.6 μm and 2.7 μm. At a distance of about 0.03 m, the power is generated at wavelength around $4 - 5$ μm due to four-wave mixing, which is consistent with the phase-matching diagram in Fig. 5.7. In the final stage, the solitons generated using four-wave mixing around $4 - 5$ μm are shifted to longer wavelengths due to the soliton self-frequency shift [116]. The center frequency of the largest soliton is shifted to around 5.5 μm. There is little additional shifting because of lower dispersion above 5 μm, as shown in Fig. 5.10, and decreased power due to the fiber attenuation. The amount of the soliton self-frequency shift in wavelength has been shown to be proportional to the dispersion [116].

Figure 5.11 shows the total generated bandwidth as a function of Λ. Note that there is a peak around $\Lambda \simeq 2.8$ μm. When the pitch is small, the bandwidth that can be generated using the four-wave mixing process, as shown in the red curve of Fig. 5.7, is narrower than the wavelength generated using a longer pitch, as shown in the blue

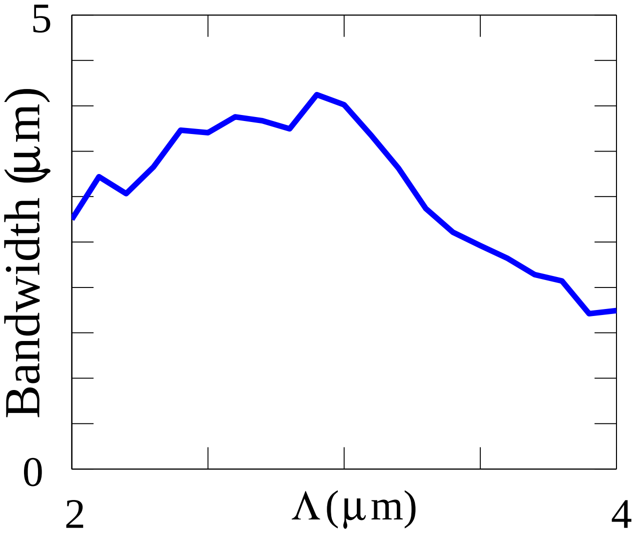

Figure 5.11: The total generated bandwidth as a function of Λ.

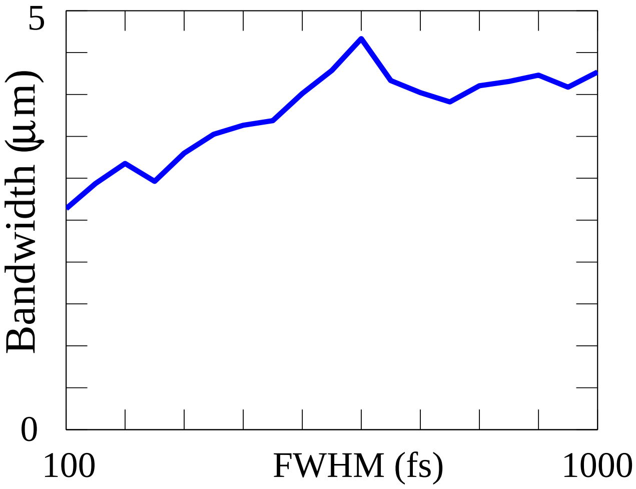

Figure 5.12: The total generated bandwidth as a function of the FWHM of the input pulse.

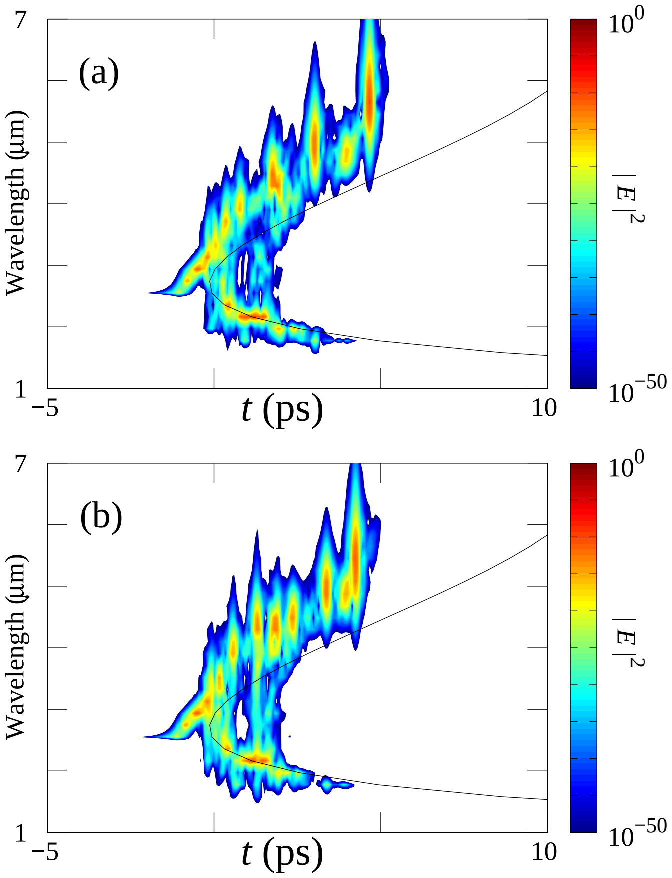

Figure 5.13: Spectrograms with (a) an input FWHM of 600 ps and (b) an input FWHM of 650 ps.

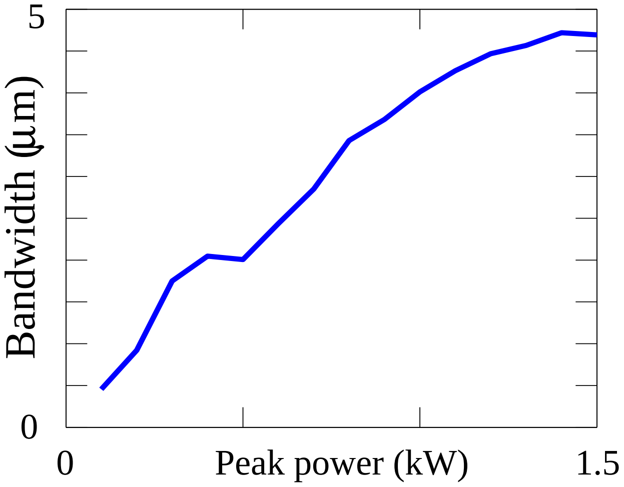

Figure 5.14: The total generated bandwidth as a function of input peak power.

curves of Fig. 5.7. When the pitch is large, the effective area becomes large and hence the nonlinearity is low. Figure 5.12 shows the total generated bandwidth as a function of the FWHM of the input pulse. The input peak power is fixed at 1 kW. Note that when the FWHM increases from 100 fs to 500 fs, the total generated bandwidth increases almost linearly, which implies that it is easier to generate a supercontinuum for a wider pulse. When the FWHM is larger than 600 fs, the curve for the total generated bandwidth fluctuates. The fluctuations occur because input pulses with different durations generate different numbers of solitons with different amplitudes, and the number and the amplitudes change abruptly. Figs. 5.13(a) and (b) show the spectrumgrams with an input FWHM of 600 ps and 650 ps, respectively. When the pulse duration is 600 fs, there are about ten solitons, one of which has a relatively large amplitude, resulting in a large self-frequency shift, as shown in Fig. 5.13(a). When the pulse duration is 650 fs, there are still about ten solitons. However, all have a relatively low amplitude, and none of them undergoes a large self-frequency shift, as shown in Fig. 5.13(b). Hence, the bandwidth goes down when the FWHM duration changes from 600 fs to 650 fs. Figure 5.14 shows the total generated bandwidth as a function of input peak power. The FWHM of the input pulse is fixed at 500 fs. The total generated bandwidth increases as the peak power increases until the peak power reaches 1.4 kW.

Chapter 6

Conclusion

Photonic crystal fibers (PCFs) can be divided into two main categories, solid core PCFs and air-guided PBGFs. In solid core PCFs, light is guided by total internal reflection. In air-guided PCFs, also called hollow core photonic band gap fibers (PBGFs), there is a big air core in the center, and the periodic cladding forms a photonic bandgap to confine the mode. PBGFs have the potential to provide very low-loss transmission, along with delivery of high power and low nonlinearity, while solid core PCF provides high nonlinearity that may be used to generate a supercontinuum. In this dissertation, we present calculations of the leakage loss, the bandgap effect, and the surface mode effect in PBGFs, and we also present calculations of supercontinuum generation using the Kerr and Raman effects in solid-core chalcogenide PCFs.

We first calculate the wave propagation in a uniform medium, three-layer slab waveguide, W-type slab waveguide, and bandgap slab waveguide. We decompose an input pulse into a set of basis functions. In leaky structures, like a W-type slab waveguide and a bandgap slab waveguide, we must integrate over a Lorentzian-shaped function to calculate the field at a distance z. The leakage loss coefficients that are calculated by integrating over the radiation mode contributions, direct determination of the leaky mode attenuation, and a perturbation method agree well. Steepest descent asymptotic analysis is applied to correctly predict the power at a large distance for all waveguide structures we consider here. The leaky mode and steepest descent asymptotic analysis yield exponential decay and algebraic decay, respectively. Hence, at a large distance, the power decay rate changes from exponential to algebraic. The wave propagation shows that the power lost in a leaky structure is actually redistributed from the core into the outside region.

We show the bandgap and mode analysis for two peaks in the relative bandgap when we vary the air-filling factor and the refractive index. The difference between the air-filling factors for the maximum relative bandgap and the lowest loss is around 0.03 with a refractive index between 1.4 and 2.8. Thus, this work supports the assumption of Pottage, *et al.* [21] that the analysis of the unit-cell bandgap is a good indication of the optimal air-filling factor for air-core PBGF design. We also found that when the relative bandgap increases, the loss decreases, and vice versa. There exists a minimum loss in the high index region. The refractive index corresponding to this minimum loss is higher than the refractive index corresponding to the maximum relative bandgap, since a high index contrast helps to confine the mode. The optimal normalized frequency corresponding to minimum loss decreases as the refractive index increases.

In terms of the surface mode effect, we found that for PBGFs with a 19-cell core, a normalized ring thickness of 0.04 yields the widest operational bandwidth, which is nearly 6%. The operational bandwidth increases as the refractive index decreases from 2.8 to 2.0. For PBGFs with a 7-cell core, one must draw fiber with a ring thickness of less than 0.03Λ to achieve a comparable operational bandwidth.

We show the third-order susceptibility and the Raman response function for As_2Se_3-based chalcogenide fiber. Using the calculated Raman response function and the total dispersion, we showed that it is possible to accurately reproduce the experimentally-observed bandwidth of the IR supercontinuum generation using chalcogenide PCF that was reported in Ref. 26. We then use the validated code to optimize the fiber geometry to maximize the supercontinuum generation in IR region. We found that the PCF becomes endlessly single-mode at $d/\Lambda < 0.42$ for all the refractive indices of glass. Using the effect of FWM in combination of SPM and SSFS, we theoretically found that a bandwidth of more than 4 μm can be generated using an endlessly single mode As_2Se_3-based chalcogenide PCF with $d/\Lambda = 0.4$ and $\Lambda = 3$ μm.

Bibliography

[1] P. Kaiser and H. W. Astle, "TestLow-loss single-material fibres made from pure fused silica," Bell Syst. Tech. J. **53**, 1021–39 (1974).

[2] B. J. Eggleton, P. S. Westbrook, C. A. White, C. Kerbage, R. S. Windeler, and G. L. Burdge, "Cladding-mode-resonances in air-silica microstructure optical fibers," J. Lightwave Technol. **18**, 1084–1100, (2000).

[3] P. Falkenstein, C. D. Merritt, and B. L. Justus, "Fused preforms for the fabrication of photonic crystal fibers," Opt. Lett. **29**, 1858–1860 (2004).

[4] J. B. Jensen, L. H. Pedersen, P. E. Hoiby, L. B. Nielsen, T. P. Hansen J. R. Folkenberg, J. Riishede, D. Noordegraaf, K. Nielsen, A. Carlsen, and A. Bjarklev, "Photonic crystal fiber based evenescent-wave sensor for detection of biomolecules in aqueous solutions," Opt. Lett. **29**, 1974–1976 (2004).

[5] C. M. Smith, N. Venkataraman, M. T. Gallagher, D. Müller, J. A. West, N. F. Borrelli, D. C. Allan, and K. W. Koch, "Low-loss hollow-core silica/air photonic bandgap fibre," Nature **424**, 657–659 (2003).

[6] T. P. Hansen, J. Broeng, S. E. B. Libori, E. Knudsen, A. Bjarklev, J. R. Jensen, and H. Simonsen, "Highly birefringent index guiding photonic crystal fibers," IEEE Photon. Technol. Lett. **13,** 588–590 (2001).

[7] K. Saitoh, N. Florous, and M. Koshiba, “Ultra-flattened chromatic dispersion controllability using a defected-core photonic crystal fiber with low confinement losses,” Opt. Express **13**, 8365–8371 (2005).

[8] T.-L. Wu and C.-H. Chao, “A novel ultraflattened dispersion photonic crystal fiber,” IEEE Photon. Technol. Lett. **17,** 67–69, (2005).

[9] B. Temelkuran, S. D. Hart, G. Benoit, J. D. Joannopoulos, and Y. Fink, “Wavelength-scalable hollow optical fibres with large photonic bandgaps for CO_2 laser transmission,” Nature **420**, 650–653, (2002).

[10] J. Broeng, S. E. Barkou, T. Søndergaard, and A. Bjarklev, “Analysis of air-guiding photonic bandgap fibers,” Opt. Lett. **25**, 96–98 (2000).

[11] J. C. Knight, J. Broeng, T. A. Birks, and P. St. J. Russell, “Photonic band gap guidance in optical fibers,” Science **282**, 1476–1478 (1998).

[12] P. St. J. Russell, “Photonic-crystal fibers,” Science **299**, 358–362 (2003).

[13] L. E. Busse, J. A. Moon, J. S. Sanghera, and I. D. Aggarwal, “Chalcogenide fibers deliver high IR power,” Laser Focus World **32**, 143–166, (1996).

[14] X. Feng, A. K. Mairaj, D. W. Hewak, and T. M. Monro, “Nonsilica glasses for holey fibers,” J. Lightwave Technol. **23**, 2046–2054 (2005).

[15] J. S. Sanghera, I. D. Aggarwal, L. E. Busse, P. C. Pureza, V. Q. Nguyen, F. H. Kung, L. B. Shaw, and F. Chenard, “Chalcogenide optical fibers target mid-IR applications,” Laser Focus World **41** 83–87 (2005).

[16] J. S. Sanghera and I. D. Aggarwal, “Active and passive applications of chalcogenide glass fibers a review,” J. Non-Cryst. Solids **256& 257**, 6–16 (1999).

[17] C. Anastassiou, G. Dellemann, O. Weisberg, and U. Kolodny, “Fibers Deliver CO_2 Laser Beams for Medical Applications,” Photonics Spectra **38** 108–112 (2004).

[18] R. E. Slusher, G. Lenz, J. Hodelin, J. Sanghera, L. B. Shaw, and I. D. Aggarwal, “Large Raman gain and nonlinear phase shifts in high-purity As_2Se_3 chalcogenide fibers,” J. Opt. Soc. Am. B **21**, 1146–1155 (2004)

[19] P. A. Thielen, L. B. Shaw, P. C. Pureza, V. Q. Nguyen, J. S. Sanghera, and I. D. Aggarwal, “Small-core As-Se fiber for Raman amplification ,” Opt. Lett. **28**, 1406–1408 (2003)

[20] K. Saitoh and M. Koshiba, “Leakage loss and group velocity dispersion in air-core photonic bandgap fibers,” Opt. Express **11**, 3100–3109 (2003).

[21] J. M. Pottage, D. M. Bird, T. D. Hedley, T. A. Birks, J. C. Knight, P. St.J. Russell and P. J. Roberts, “Robust photonic band gaps for hollow core guidance in PCF made from high index glass,” Opt. Express **11**, 2854–2861 (2003).

[22] J. West, C. Smith, N. Borrelli, D. Allan, and K. Koch, “Surface modes in air-core photonic band-gap fibers,” Opt. Express **12**, 1485–1496 (2004).

[23] R. Amezcua-Correa, N. G. Broderick, M. N. Petrovich, F. Poletti, and D. J. Richardson, “Optimizing the usable bandwidth and loss through core design in realistic hollow-core photonic bandgap fibers,” Opt. Express **14**, 7974–7985 (2006).

[24] R. Amezcua-Correa, N. G. Broderick, M. N. Petrovich, F. Poletti, and D. J. Richardson, “Design of 7 and 19 cells core air-guiding photonic crystal fibers for low-loss, wide bandwidth and dispersion controlled operation,” Opt. Express **15**, 17577–17586 (2007).

[25] A. Kudlinski, A. K. George, J. C. Knight, J. C. Travers, A. B. Rulkov, S. V. Popov, and J. R. Taylor, “Zero-dispersion wavelength decreasing photonic crystal fibers for ultraviolet-extended supercontinuum generation,” Opt. Express **14**, 5715–5722 (2006)

[26] L. B. Shaw, V. Q. Nguyen, J. S. Sanghera, I. D. Aggarwal, P. A. Thielen, and F. H. Kung, “IR supercontinuum generation in As-Se photonic crystal fiber,” in Proc. Advanced Solid State Photonics, Vienna, Austria, paper TuC5 (2005).

[27] S. E. Miller, “Integrated optics: an introduction,” Bell Syst. Tech. J. **48**, 2059–2069 (1969).

[28] E. A. Marcatili, “Dielectric rectangular waveguide and directional coupler for integrated optics,” Bell Syst. Tech. J. **48** 2071–2102 (1969).

[29] E. Snitzer, “Cylindrical dielectric waveguide modes,” J. Opt. Soc. Am. **51**, 491–198 (1961).

[30] D. Gloge, “Weakly guiding fibers,” Appl. Opt. **10** 2252–2258 (1971).

[31] J. Jin, *The Finite Element Method in Electromagnetics*, (John Wiley & Sons, Inc., 2nd Ed. 2002).

[32] K. Kawano and T. Kitoh, *Introduction to Optical Waveguide Analysis Solving Maxwell's Equations and the Schrödinger Equation*, (John Wiley & Sons, Inc., 2001).

[33] M. Koshiba and Y. Tsuji, "Curvilinear hybrid edge/nodal elements with triangular shape for guided-wave problems," J. Lightwave Technol. **18**, 737–743 (2000).

[34] M. N. O. Sadiku, *Numerical Techniques in Electromagnetics*, (CRC Press LLC, 2nd Ed., 2001).

[35] T. P. White, B. T. Kuhlmey, R. C. McPhedran, D. Maystre, G. Renversez, C. M. de Sterke, and L. C. Botten, "Multipole method for microstructured optical fibers. I. Formulation," J. Opt. Soc. Am. B **19**, 2322–2330 (2002).

[36] B. T. Kuhlmey, T. P. White, G. Renversez, D. Maystre, L. C. Botten, C. M. de Sterke, and R. C. McPhedran, "Multipole method for microstructured optical fibers. II. Implementation and results," J. Opt. Soc. Am. B **19**, 2331–2340 (2002).

[37] D. Marcuse, "Solution of the vector wave equation for general dielectric waveguides by the Galerkin method," IEEE J. Quantum Electron. **28**, 459-465 (1992).

[38] S. Johnson and J. Joannopoulos, "Block-iterative frequency-domain methods for Maxwell's equations in a planewave basis," Opt. Express **8**, 173–190 (2001),

[39] J. M. Lourtioz, H. Benisty, V. Berger, J.-M. Gérard, D. Maystre, and A. Tchelnokov, *Photonic Crystals Towards Nonoscale Photonic Devices*, (Springer, 2005).

[40] D. Marcuse, *Theory of Dielectric Optical Waveguides* (Academic Press, Inc., 1991)

[41] A. W. Snyder and J. D. Love, *Optical Waveguide Theory* (Kluwer Academic Publishers, 1983)

[42] R. E. Collin, *Field Theory of Guided Waves* (IEEE Press, 2nd Ed. 1991)

[43] S. Barone, "Leaky wave contributions to the field of a line source above a dielectric slab," Microwave Res. Inst., Polytechnic Inst. of Brooklyn, Brooklyn, NY, Rept. R-532-546, PIB-462, November (1956).

[44] S. Barone and A. Hessel, "PART II - Leaky wave contributions to the field of a line source above a dielectric slab," Microwave Res. Inst., Polytechnic Inst. of Brooklyn, Brooklyn, NY, Rept. R-698-58, PIB-626, December, (1958).

[45] N. Marcuvitz, "On field representations in terms of leaky modes or eigenmodes," IEEE Transactions on Antennas and Propagation, **4**, 192–194 (1956).

[46] T. Tamir and A. A. Oliner, "Guided complex waves. Part 1: fields at an interface," Proc. IEE **110**, 310–324 (1963).

[47] T. Tamir and A. A. Oliner, "Guided complex waves. Part 2: relation to radiation pattern," Proc. IEE **110**, 325–334 (1963).

[48] C. W. Hsue and T. Tamir, "Evolution of transverse-electric surface and leaky waves guided by an asymmetric layer configuration," J. Opt. Soc. Am. A **1**, 923–931 (1984).

[49] T. Tamir and F. Y. Kou, "Varieties of leaky waves and their excitation along multilayered structures," IEEE J. Quantum Electron. **22**, 544–551 (1986).

[50] S. T. Peng and A. A. Oliner, “Guidance and leakage properties of a class of open dielectric waveguides. I. Mathematical formulations,” IEEE Trans. Microwave Theory Tech. **MTT-29**, 843-855 (1981).

[51] A. A. Oliner, S. T. Peng, T. I. Hsu, and A. Sanchez, “Guidance and leakage properties of a class of open dielectric waveguides. II. New physical effects,” IEEE Trans. Microwave Theory Tech. **MTT-29**, 855-869 (1981).

[52] E. S. Cassedy and M. Cohn, “On the existence of leaky waves due to a line source above a grounded dielectric slab,” IRE/IEEE Trans. Microw. Theory Tech. **9**, 243–247 May (1961).

[53] D. B. Hall and C. Yeh, “Leaky waves in a heteroepitaxial film,” J. Appl. Phys. **44**, 2271–2274 (1973).

[54] H. Haus and D. Miller, “Attenuation of cutoff modes and leaky modes of dielectric slab structures,” IEEE J. of Quantum Electron. **22**, 310–318 (1986).

[55] Y. Suematsu and K. Furuya, “Quasi-Guided Modes and Related Radiation Losses in Optical Dielectric Waveguides with External Higher Index Surroundings,” IEEE Trans. Microw. Theory Tech. **23**, 170–175 (1975).

[56] S. Kawakami and S. Nishida, “Characteristics of a doubly clad optical fiber with a low-index inner cladding,” IEEE J. of Quantum Electron. **10**, 879–887 (1974).

[57] S. Kawakami and S. Nishida, “Perturbation theory of a doubly clad optical fiber with a low-index inner cladding,” IEEE J. of Quantum Electron. **11**, 130–138 (1975).

[58] J. Arnbak, “Leaky waves on a dielectric rod,” Electron. Lett. **5**, 41–42 (1969).

[59] J. R. James, “Leaky waves on a dielectric rod,” Electron. Lett. **5**, 252–254 (1969).

[60] J. Burke, “Propagation constants of resonant waves on homogeneous, isotropic slab waveguides,” Appl. Opt. **9**, 2444–2452 (1970).

[61] V. V. Shevchenko, “On the behavior of wave numbers beyond the critical value for waves in dielectric waveguides (media with losses),” Radiophys. Quantum Electron. **15**, 194–200 (1972).

[62] A. W. Snyder and D. J. Mitchell, “Ray attenuation in lossless dielectric structures,” J. Opt. Soc. Am. **64**, 956–963 (1974).

[63] A. W. Snyder and D. J. Mitchell, “Leaky mode analysis of circular optical waveguides,” Opto-electronics **6**, 287–296 (1974).

[64] M. Maeda and S. Yamada, “Leaky modes on W-fibers: mode structure and attenuation,” Appl. Opt. **16**, 2198–2203 (1977).

[65] A. W. Snyder, “Leaky-ray theory of optical waveguides of circular cross section,” Appl. Phys. **4**, 273–298 (1974).

[66] A. W. Snyder and D. J. Mitchell, “Leaky rays on circular optical fibers,” J. Opt. Soc. Am. **64**, 599–607 (1974).

[67] A. W. Snyder, D. J. Mitchell, and C. Pask, “Failure of geometric optics for analysis of circular optical fibers,” J. Opt. Soc. Am. **64**, 608–614 (1974)

[68] J. D. Love and C. Winkler, “Attenuation and tunneling coefficients for leaky rays in multilayered optical waveguides,” J. Opt. Soc. Am. **67**, 1627–1633 (1977)

[69] J. T. Chilwell and I. J. Hodgkinson, “Thin-films field-transfer matrix theory of planar multilayer waveguides and reflection from prism-loaded waveguides,” J. Opt. Soc. Am. A **1**, 742–753 (1984).

[70] L. Torner, F. Canal, and J. Hernandez-Marco, “Leaky modes in multilayer uniaxial optical waveguides,” Appl. Opt. **29**, 2805–2814 (1990).

[71] J. Petr*áč*ek and K. Singh, “Determination of leaky modes in planar multilayer waveguides,” IEEE Photon. Technol. Lett. **14**, 810–812 (2002).

[72] F. Zolla, G. Renversez, A. Nicolet, B. Kuhlmey, S. Guenneau, and D. Felbacq, *Foundations Of Photonic Crystal Fibres* (Imperial College Press, 2005).

[73] K. Okamoto, *Fundamentals of Optical Waveguides* (Academic Press, 2000), chap. 2.

[74] E. A. Coddington and N. Levinson, *Theory of Ordinary Differential Equations* (McGraw-Hill Book Company, Inc., 1984).

[75] W. Klaus and W. R. Leeb, “Transient fields in the input coupling region of optical single-mode waveguides,” Opt. Express **15**, 11808–11826 (2007).

[76] S.-L. Lee, Y. Chung, L. A. Coldren, and N. Dagli, “On leaky mode approximations for modal expansion in multilayer open waveguides,” IEEE J. Quantum Electron. **31**, 1790–1802 (1995).

[77] G. B. Arfken and H. J. Weber, *Mathematical Methods for Physicists* (Academic Press, San Diego, CA 5th Ed. 2001)

[78] J. D. Joannopoulos, S. G. Johnson, J. N. Winn, R. D. Meade, *Photonic Crystals: Molding the Flow of Light*, (Princeton University Press; 2nd Ed, 2008).

[79] K. Hoffman and R. Kunze, *Linear Algebra* (Prentice Hall, 2nd Ed. 1971), chap. 8.5.

[80] P. M. Morse and H. Feshbach, *Methods of Theoretical Physics* (McGraw-Hill Book Company, Inc., 1953), chap. 4.6.

[81] M. J. Adams, *An Introduction to Optical Waveguides* (John Wiley & Sons, 1981), chap. 2.6.

[82] R. V. Churchill and J. W. Brown, *Complex Variables and Applications* (McGraw-Hill, Inc, 5th Ed. 1990), chap. 2.

[83] D. Marcuse, *Light Transmission Optics* (Van Nostrand Reinhold Company, 1972), chap. 8.4.

[84] R. N. Bracewell, *The Fourier Transform and Its Applications*, (McGraw-Hill, 3rd edition, 1999).

[85] P. Yeh, A. Yariv, and C.-S. Hong, "Electromagnetic propagation in periodic stratified media. I. General theory," J. Opt. Soc. Am. **67**, 423–438 (1977).

[86] J. Hu and C. R. Menyuk, "Leakage loss and bandgap analysis in air-core photonic bandgap fiber for nonsilica glasses," Opt. Express **15**, 339–349 (2007).

[87] A. Yariv and P. Yeh, *Optical Waves in Crystals* (John Wiley & Sons, Inc., 1984), chap. 11.10.

[88] S. Guo, F. Wu, S. Albin, H. Tai, and R. Rogowski, "Loss and dispersion analysis of microstructured fibers by finite-difference method," Opt. Express **12**, 3341–3352 (2004),

[89] J. P. Berenger, "A perfectly matched layer for the absorption of electromagnetic waves," J. Comput. Phys. **114**, 110–117 (1994).

[90] A. Taflove and S C. Hagness, *Computational Electrodynamics*, (Artech House, Inc, 2nd Ed, 2000).

[91] G. H. Golub and C. F. Van Loan, *Matrix Computations*, (The Johns Hopkins University Press, 3rd Ed, 1996).

[92] T. M. Monro, Y. D. West, D. W. Hewak, N. G. R. Broderick, and D. J. Richardson, "Chalcogenide holey fibres," Electron. Lett. **36**, 1998–2000 (2000).

[93] L. B. Shaw, J. S. Sanghera, and I. D. Aggarwal, "As-S and As-Se based photonic band gap fiber for IR laser transmission," Opt. Express **11**, 3455–3460 (2003).

[94] S. G. Johnson, and J. D. Joannopoulos, "Block-iterative frequency-domain methods for Maxwell's equations in planewave basis," Opt. Express **8**, 173–190 (2001).

[95] J. D. Joannopoulos, R. D. Meade, and J. N. Winn, *Photonic Crystals*, (Princeton University Press, 1995).

[96] H. K. Kim, M. J. F. Digonnet, G. S. Kino, J. Shin, and S. Fan, "Simulations of the effect of the core ring on surface and air-core modes in photonic bandgap fibers," Opt. Express **12**, 3436–3442 (2004).

[97] G. J. Pearce, J. M. Pottage, D. M. Bird, P. J. Roberts, J. C. Knight, and P. St. J. Russell, “Hollow-core PCF for guidance in the mid to far infra-red,” Opt. Express **13**, 6937–6946 (2005).

[98] K. Saitoh, N. Mortensen, and M. Koshiba, “Air-core photonic band-gap fibers: the impact of surface modes,” Opt. Express **12**, 394–400 (2004).

[99] P. Roberts, F. Couny, H. Sabert, B. Mangan, D. Williams, L. Farr, M. Mason, A. Tomlinson, T. Birks, J. Knight, and P. St. J. Russell, “Ultimate low loss of hollow-core photonic crystal fibres,” Opt. Express **13**, 236–244 (2005).

[100] J. M. Dudley, G. Genty, and S. Coen, “Supercontinuum generation in photonic crystal fiber,” Rev. Mod. Phys. **78**, 1135–1184 (2006).

[101] J. H. V. Price, T. M. Monro, H. Ebendorff-Heidepriem, F. Poletti, P. Horak, V. Finazzi, J. Y. Y. Leong, P. Petropoulos, J. C. Flanagan, G. Brambilla, X. Feng, and D. J. Richardson, “Mid-IR Supercontinuum Generation From Non-silica Microstructured Optical Fibers,” IEEE J. Sel. Topics Quantum Electron. **13**, 738–749, (2007).

[102] P. Domachuk, N. A. Wolchover, M. Cronin-Golomb, A. Wang, A. K. George, C. M. B. Cordeiro, J. C. Knight, and F. G. Omenetto, “Over 4000 nm bandwidth of mid-IR supercontinuum generation in sub-centimeter segments of highly nonlinear tellurite PCFs,” Opt. Express **16**, 7161–7168 (2008).

[103] R. H. Stolen, J. P. Gordon, W. J. Tomlinson, and H. A. Haus, “Raman response function of silica-core fibers,” J. Opt. Soc. Am. B **6**, 1159–1166 (1989).

[104] W. H. Reeves, D. V. Skryabin, F. Biancalana, J. C. Knight, P. St. J. Russell, F. G. Omenetto, A. Efimov, and A. J. Taylor, “Transformation and control of ultra-short pulses in dispersion-engineered photonic crystal fibers,” Nature **424**, 511–515 (2003).

[105] M. A. Foster, J. M. Dudley, B. Kibler, Q. Cao, D. Lee, R. Trebino, and A. L. Gaeta, “Nonlinear pulse propagation and supercontinuum generation in photonic nanowires: experiment and simulation,” Appl. Phys. B **81**, 363–367 (2005).

[106] M. L. V. Tse, P. Horak, F. Poletti, N. G. Broderick, J. H. Price, J. R. Hayes, and D. J. Richardson, “Supercontinuum generation at 1.06 μm in holey fibers with dispersion flattened profiles,” Opt. Express **14**, 4445–4451 (2006).

[107] T. A. Birks, J. C. Knight, and P. St. J. Russell, “Endlessly single-mode photonic crystal fiber,” Opt. Lett. **22**, 961–963 (1997).

[108] A. W. Snyder and J. D. Love, *Optical Waveguide Theory* (Chapman & Hall, London, 1983).

[109] K. Saitoh and M. Koshiba, “Numerical modeling of photonic crystal fibers,” J. Lightwave Technol. **23**, 3580–3590, (2005).

[110] M. Koshiba, “Full-vector analysis of photonic crystal fibers using the finite element method,” IEICE Trans. Electron., **85**-C, 881–888 2002.

[111] M. Koshiba and K. Saitoh, “Applicability of classical optical fiber theories to holey fibers,” Opt. Lett., **29** 1739–1741, (2004).

[112] G. P. Agrawal, *Nonlinear Fiber Optics* (Academic Press, New York, 2001).

[113] G. Genty, M. Lehtonen, H. Ludvigsen, J. Broeng, and M. Kaivola, “Spectral broadening of femtosecond pulses into continuum radiation in microstructured fibers,” Opt. Express **10**, 1083–1098 (2002),

[114] J. Hu, B. S. Marks, C. R. Menyuk, J. Kim, T. F. Carruthers, B. M. Wright, T. F. Taunay, and E. J. Friebele, “Pulse compression using a tapered microstructure optical fiber,” Opt. Express 14, 4026–4036 (2006).

[115] V. Q. Nguyen, J. S. Sanghera, P. Pureza, F. H. Kung, I. D. Aggarwal, “Fabrication of Arsenic Selenide Optical Fiber with Low Hydrogen Impurities,” J. Am. Ceram. Soc. **85**, 2849-2851 (2002).

[116] J. P. Gordon, “Theory of the soliton self-frequency shift,” Opt. Lett. **11**, 662–664 (1986).